**TECHNISCHE
UNIVERSITÄT
WIEN**
Vienna University of Technology

Dissertation

Lanthanum Strontium Cobaltite as Model System to Study Relationships of Surface Chemistry, Structure, and the Oxygen Exchange Kinetics

ausgeführt zum Zwecke der Erlangung des akademischen Grades
eines Doktors der Naturwissenschaften
unter der Leitung von

Univ. Prof. Dipl. Phys. Dr. Jürgen Fleig

Institut für Chemische Technologien und Analytik,
Fachbereich Elektrochemie

eingereicht an der Technischen Universität Wien
von

Dipl.-Ing. Markus Kubicek

Matrikelnummer: 9925793
Hederichgasse 5 1100 Wien

Wien, im Mai 2013

Abstract

The oxygen reduction reaction (ORR) on the mixed ionic and electronic conducting (MIEC) oxide Lanthanum-Strontium-Cobaltite ($La_{1-x}Sr_xCoO_{3-\delta}$, LSC) was investigated. The oxygen reduction reaction on MIEC oxides such as LSC is of scientific interest for several applications: cathodes for solid oxide fuel cells (SOFCs), sensors or oxygen separation membranes. In this work it was aimed to find correlations between structural and chemical properties of the material and the catalytic activity towards the ORR. Besides oxide and thin film preparation, the emphasis was clearly put on several analytical methods which were used to detect changes in catalytic activity or chemical composition at surfaces and interfaces. In addition to the studies on LSC, these analytical challenges inspired the adaption of existing and development of novel measurement set-ups and modes for inductively coupled plasma-optical emission spectrometry (ICP-OES) and for time-of-flight secondary ion mass spectrometry (ToF-SIMS).

LSC thin film electrodes ($\sim$200 nm thickness) were prepared on single crystalline yttria stabilized zirconia ($Zr_{1-x}Y_xO_{2-\delta}$, YSZ), an SOFC electrolyte material. These model-type samples enabled to perform electrochemical SOFC half-cell measurements and to apply many other analytical methods on the same samples. By using impedance spectroscopy it was shown that the catalytic activity of the LSC surface is decreasing after annealing at high temperatures. Chemical etching of a few nm of material off the LSC surface led again to a recovery of the catalytic activity for ORR. By using ToF-SIMS and ICP-OES in improved etching experiments, an enrichment of Sr at the LSC surface could be verified which is accompanying the degradation of catalytic activity. Further experiments to study the kinetics of the formation of this enrichment and the mobility of the cations in LSC at SOFC operation temperatures were encouraged by these results. The diffusion coefficients for all cations in LSC thin films were measured down to temperatures as low as 625°C. Interestingly, similar diffusion parameters for all cations were found in these experiments and their values would even allow much faster segregation of cations than observed. It was shown that trying to avoid

segregation of cations by reducing the operation temperature to "freeze" the cation lattice would not reasonably work for SOFCs.

In further experiments using ~20 nm epitaxial LSC films on different (100) single crystalline substrates, the influence of lattice strain on the oxygen exchange kinetics and diffusion was investigated. $^{16}O/^{18}O$ oxygen isotope exchange and ToF-SIMS depth profiling were used to determine the parameters of oxygen exchange and diffusion of tensile and compressively strained LSC. A strong influence of lattice strain on the kinetics of the ORR on LSC was found and reproduced for different compositions. Tensile lattice strain was shown to significantly increase both, the surface exchange and the diffusion of oxygen in LSC thin films.

For achieving these results and also for other analytical tasks such as the determination of active and resistive zones of electrodes, a novel operation mode for ToF-SIMS was developed. Adapting the guidance of the Bi-primary ion beam led to improvements of lateral resolution and for determining the accurate oxygen isotope fractions. An overview of several different examples for applications of the novel mode is given including measurements on functional oxides and investigations of the ORR on Pt electrodes.

This SIMS mode was also used for isotope exchange depth profiling on 200 nm LSC thin films on YSZ. The same samples were then investigated at the same temperature (400°C) by impedance spectroscopy thus enabling a complementary analysis of the electrode resistances with two different methods. By this comparative approach a much more detailed interpretation was possible than with one method alone.

Kurzfassung

Die Sauerstoffreduktions-Reaktion am gemischtleitenden Oxid Lanthan-Strontium-Cobaltat ($La_{1-x}Sr_xCoO_{3-\delta}$, LSC) wurde an Dünnschichten untersucht. Diese LSC Dünnschichten, welche mittels gepulster Laserdeposition auf einkristallinen Substraten abgeschieden wurden, dienten in zahlreichen Untersuchungsmethoden als Modellsystem. Die Sauerstoffreduktions-Reaktion und das gemischtleitende Oxid LSC sind für Kathoden in Festoxid-Brennstoffzellen (SOFCs), für Sensoren oder für Sauerstoff-Trennmembranen von Bedeutung. Das Ziel der Arbeit war es, Korrelationen zwischen der Struktur, den chemischen Eigenschaften und der katalytischen Aktivität für die Sauerstoffreduktion zu finden. Neben der Herstellung der LSC Dünnschichten lag das Hauptaugenmerk auf verschiedenen analytischen Methoden, die ermöglichten auch kleinste Änderungen an Ober- und Grenzflächen nachzuweisen. Die analytischen Herausforderungen bei den Untersuchungen von LSC inspirierten auch die Entwicklung von neuen analytischen Ansätzen und Messmodi für Optische Emissionsspektroskopie mit induktiv gekoppeltem Plasma (ICP-OES) und Flugzeit-Sekundärionen-Massenspektrometrie (ToF-SIMS).

LSC Dünnfilmelektroden (~200 nm Dicke) auf einkristallinem Yttrium-dotierten Zirkoniumoxid ($Zr_{1-x}Y_xO_{2-\delta}$, YSZ), einem Festoxidelektrolyten, wurden verwendet, da an diesen sowohl elektrochemische Halbzellenmessungen durchführbar als auch viele andere analytische Methoden anwendbar sind. Mittels Impedanzspektroskopie konnte gezeigt werden, dass die katalytische Aktivität von LSC-Oberflächen bei hohen Temperaturen, wie sie in SOFCs verwendet werden, abnimmt. Durch Entfernen von wenigen Nanometern Materials von der LSC Oberfläche konnte jedoch wieder die ursprünglich hohe katalytische Aktivität erlangt werden. Mittels Untersuchungen mit ToF-SIMS und ICP-OES in neuartigen in-situ-Ätz-Experimenten konnte eine Änderung in der Kationen-Zusammensetzung von LSC, insbesondere eine Anreicherung von Sr an der Oberfläche nachgewiesen werden. In weiteren Experimenten stand daher die Mobilität der Kationen im Vordergrund. Verglichen mit bereits existierenden Studien konnten die Diffusionskoeffizienten von allen Kationen in LSC bei besonders niedrigen

Temperaturen bestimmt werden. Interessanterweise zeigten alle Kationen ähnliche Diffusionsparameter und außerdem zeigte es sich, dass die Beweglichkeit der Kationen sogar deutlich schnellere Segregation ermöglichen könnte als beobachtet. Es konnte in Folge geschlossen werden, dass ein „Einfrieren" von Kationen um mögliche Segregationen zu verhindern durch Reduktion der Arbeitstemperatur einer Festoxid-Brennstoffzelle nicht praktikabel ist.

Der Einfluss von Gitterspannungen auf den Oberflächenaustausch und die Diffusion von Sauerstoff in LSC wurde in weiteren Experimenten mit ~20 nm dicken epitaktischen Filmen untersucht. Sauerstoffisotopenaustausch von ^{16}O und ^{18}O und ToF-SIMS Tiefenprofile bildeten die Grundlage um die kinetischen Parameter des Sauerstoffaustauschs an LSC zu bestimmen. Es wurde gefunden, dass Gitterspannungen einen starken Einfluss haben, wobei planare Zugspannung sowohl zu schnellerem Oberflächenaustausch von Sauerstoff, als auch zu dessen schnellerer Diffusion in LSC führte.

Für die eben genannten aber auch für andere Untersuchungen an Elektroden mittels ToF-SIMS wurde ein neuartiger Messmodus entwickelt und angewandt. Durch Änderungen in der Strahlführung des Primärionenstrahls konnten die Genauigkeit von Sauerstoff-Isotopenmessung und die laterale Auflösung gesteigert werden. Neben der Beschreibung des Messmodus werden auch mehrere Anwendungsbeispiele beschrieben, wie Untersuchungen an Oxiden und Platinelektroden, zur Oxidation von Stahl sowie zur Korrosion von Kupfer.

Der oben beschriebene Messmodus wurde auch für ToF-SIMS Tiefenprofilmessungen nach Sauerstoffaustauschexperimenten an 200 nm LSC Dünnfilmen auf YSZ verwendet. Die selben Proben wurden anschließend bei der gleichen Temperatur (400°C) mittels Impedanzspektroskopie untersucht. Die vergleichende Verwendung dieser unterschiedlichen Methoden ermöglichte eine weitaus detailliertere Analyse der verschiedenen Beiträge zum Elektrodenwiderstand als mit nur einer Methode allein möglich gewesen wäre.

Table of Contents

1 Introduction

1.1 Scope

In this thesis, investigations of the mixed conducting perovskite oxide $La_{1-x}Sr_xCoO_{3-\delta}$, LSC with respect to its use as cathode in solid oxide fuel cells (SOFCs) are summarized. LSC is of scientific interest because of its high ionic and electronic conductivity and its high catalytic activity for oxygen reduction even at low SOFC operation temperatures. The scope of this thesis reaches from electrochemical measurements of half cells and tracer diffusion experiments of oxygen and cations to the investigation and quantification of chemical changes in the first monolayers at the surface of LSC. The aim was to investigate the relationship between the structure, the composition, and the surface chemistry of LSC on one side, and its electrical, catalytic and diffusion-related properties in the other side. A core analytical method for the scientific work was time of flight-secondary ion mass spectrometry (ToF-SIMS), for which a novel measurement mode was developed, which is also described in detail.

1.2 Motivation and State of Research

One of the biggest challenges of today is to generate enough electrical energy for maintaining and improving the life standards of people, while reducing the harmful emission of greenhouse gases. Because a rigorous reduction of today's energy consumption seems to be impossible for social and economic reasons, technologies for cleaner energy production are necessary. Many of these - often called "new" - energy technologies already exist, and among them are ceramic fuel cells.[1-7] They offer the possibility to convert chemical energy into electrical energy with very high efficiency. Among the different types of fuel cells, in this work only solid oxide fuel cells (SOFCs) will be discussed. In comparison to other fuel cell types, SOFCs work at higher temperatures (typically 700-1000°C)[1, 5] and they have the highest fuel flexibility enabling them to operate directly on hydrocarbons.[1, 2, 4, 5, 7] The main advantage of SOCFs over conventional caloric power plants is their higher efficiency. SOFCs are not limited in theoretical efficiency by Carnot's cycle; rather the whole Gibbs free energy (ΔG) of a chemical reaction can be converted into electrical energy.

In Fig. 1, a sketch of a SOFC operated with oxygen and hydrogen shows the working principle. Oxygen is reduced at the cathode (Eq. 1), transported through the electrolyte and reacts at the anode with hydrogen (or hydrocarbon fuel gases) to form water (and CO_2) according to Eq. 2. The overall reactions are chemically driven, but as only charged oxide ions can migrate through the electrolyte, charges are separated and an electrical voltage is generated between cathode and anode. This voltage can be used for electrical power generation. Of the three main components of a SOFC (anode, cathode, and electrolyte) the cathode and the chemical reactions related to it are a central topic of this work.
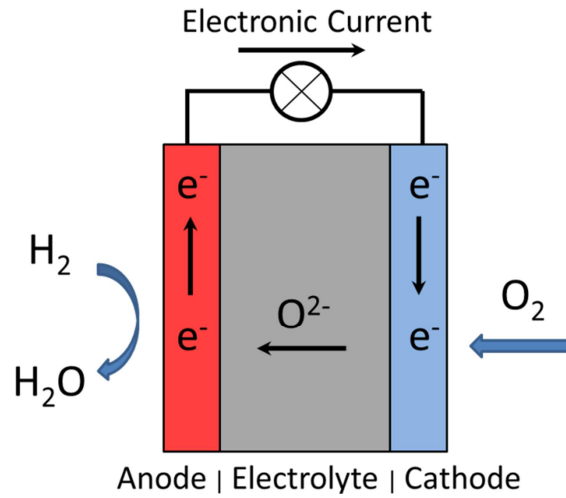
Figure 1: Sketch of a solid oxide fuel cell operated with oxygen and hydrogen.

$$\frac{1}{2}O_2 + 2e^- \rightleftharpoons O^{2-} \qquad\qquad\qquad \textit{SOFC cathode reaction} \text{ (1)}$$

$$O^{2-} + H_2 \rightleftharpoons H_2O + 2e^- \qquad\qquad\qquad \textit{SOFC anode reaction} \text{ (2)}$$

One of the main goals of SOFC research is to lower the operation temperatures to 500-700°C.[2, 6] This would be advantageous for the durability of the casing materials, reduce thermal expansion stress during heat-up and even slightly increase the efficiency. At these temperatures, the slow kinetics of the oxygen reduction reaction (Eq. 1) at the cathode is usually responsible for the biggest part of resistive losses of SOFCs, what makes improving the cathode crucial.[8-10] Pt electrodes were used in the past,[4, 11] but special oxide materials are commonly used today as cathode material to catalyze the oxygen reduction reaction (ORR). These oxides with mixed ionic and electronic conduction help to enhance the reaction rates by increasing the electrochemically active area[9]. This is the case, because for metal electrodes only the so called "surface path" can be used in the oxygen reduction reaction. Here oxygen incorporation into the electrolyte is only possible via a small active area very close to the three phase boundary of gas|electrode|electrolyte as shown in Fig. 2a. For mixed

ionic and electronic conducting (MIEC) oxides, also the "bulk path" for oxygen reduction becomes possible and typically dominating. Via this path, oxygen is reduced and incorporated on the whole cathode surface and oxide ions are then transferred into the electrolyte (cf. Fig. 2b).
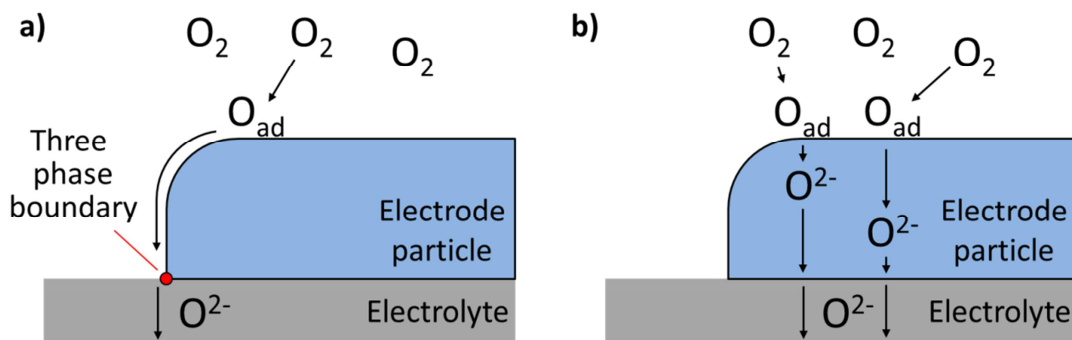

Figure 2: Reaction paths of the oxygen reduction reaction for solely electronic conducting cathodes (a), and mixed ionic electronic cathodes (b).

The MIEC oxides used as cathode materials are often perovskite-type oxides with the general chemical composition $ABO_{3\pm\delta}$. Here A is a large cation (e.g. Sr^{2+}, La^{3+}) and B is a small transition metal cation (e.g. $Fe^{3+/4+}$, $Mn^{3+/4+}$). $O_{3\pm\delta}$ means that in a typical perovskite stoichiometry there are three oxide ions per unit cell. However, in MIEC oxides often a slight deviation from the stoichiometry is present, which is crucial for the ionic conductivity. The oxide which was most commonly used for commercial SOFCs in the last years is $La_{1-x}Sr_xMnO_{3\pm\delta}$ (LSM), which has only a very low ionic conductivity. It is therefore regularly used as composite together with fast ion conductors. In research, especially MIEC oxides with significantly higher ionic conductivity than LSM are of interest. These materials, for example $La_{1-x}Sr_xCo_{1-y}Fe_yO_{3-\delta}$ (LSCF) or $Ba_{1-x}Sr_xCo_{1-y}Fe_yO_{3-\delta}$ (BSCF), can enable SOFC operation at lower temperatures which is desired. In this work, thin films of $La_{1-x}Sr_xCoO_{3-\delta}$ (LSC) with $0.2 \leq x \leq 0.4$ are used as model system for several investigations. Fig. 3 shows a model of the perovskite crystal structure of LSC. The cubic structure is shown, although slight rhombohedral

distortions (by several tenth of a degree) can occur in the crystal lattice of LSC depending on the exact stoichiometry and the temperature.[12]
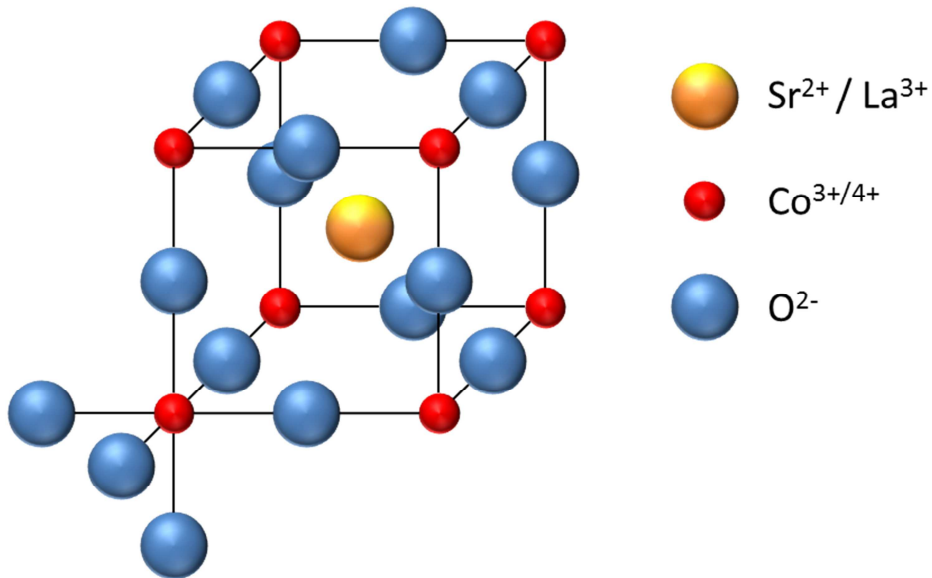

Figure 3: Model of the crystal structure of La$_{1-x}$Sr$_x$CoO$_{3-\delta}$. The cubic perovskite structure is shown, slight lattice distortions can occur depending on stoichiometry and temperature.

LSC is characterized by a high ionic and electronic conductivity.[13] The ionic conductivity becomes possible by the presence of oxygen vacancies ($V_O^{\cdot\cdot}$) in the crystal lattice. Their number is represented by δ in the chemical formula and depends strongly on the oxygen partial pressure and the temperature.[14] A typical value of δ for La$_{0.6}$Sr$_{0.4}$CoO$_{3-\delta}$ at 600°C in air is ~0.05.[12] The high electronic conductivity of ~1000 S/cm[10] is achieved by hole conduction similar to an acceptor doped semiconductor (p-type), which can also be described by the mixed valence of the transition metal cation Co$^{3+/4+}$. The high ionic and electronic conductivity as well as the high catalytic activity towards the ORR would make LSC an ideal SOFC cathode material, but its downside is its low chemical stability:[7] Reactions with yttria stabilized zirconia, an important SOFC electrolyte material, at high temperatures,[15, 16]

instability at low oxygen partial pressures,[17] or degradation related to the so called "Cr poisoning" [18] are reported.

Even if some of these problems might be improvable by new materials, recent research efforts have focused not only on finding new cathode materials, but also on analyzing and improving existing ones. The kinetics of the ORR can be influenced in numerous ways such as by microstructural optimization,[19, 20] surface decoration layers,[21] DC-polarization pulses,[22] chemical surface treatment,[23] or by lattice strain[24] thus achieving strong enhancements of exchange current densities up to several orders of magnitudes. On the other side, degradation of the catalytic properties of the cathode material can often be observed at SOFC operation temperatures. Chemical side reactions of the cathode or the segregation of cations either at the surface or at the cathode|electrolyte interface are often responsible for the degradation of catalytic activity.[25-27] As many effects and processes are consistently observable for several of the chemically similar MIEC oxides, a better understanding of one system can provide valuable information to improve SOFC cathodes in general. Further details on the status of research and open questions regarding the interplay of structural or chemical properties and electrochemical electrode performance are also given in the following sections.

In this thesis LSC thin film electrodes prepared by pulsed laser deposition (PLD) were used as model system to investigate the chemical and structural properties and processes which strongly influence the catalytic activity of SOFC cathodes. In chapter 2, the relationship between cation segregation and the oxygen reduction kinetics is discussed. Here a novel measurement set-up for inductively coupled plasma-optical emission spectroscopy (ICP-OES) was used together with impedance spectroscopy and surface analysis by ToF-SIMS. In chapter 3, cation mobility and diffusion are investigated in order to study their influence on segregation effects in LSC. Chapter 4 contains investigations on the influence of lattice strain on the oxygen reduction kinetics of LSC. Here isotope exchange experiments were performed on 20 nm thin epitaxial LSC films. In chapter 5, a novel ToF-SIMS operation mode is presented which was developed as analytical tool for optimizing oxygen isotope analysis. Chapter 6 shows that complementary measurements of the electrode kinetics by impedance

spectroscopy and oxygen isotope exchange depth profiling are very helpful for a correct mechanistic interpretation of electrode resistances.

2 Relationship between Cation Segregation and the Electrochemical Oxygen Reduction Kinetics of La$_{0.6}$Sr$_{0.4}$CoO$_{3-\delta}$ Thin Film Electrodes

This chapter contains in large part material published as scientific paper in the "Journal of the Electrochemical Society".[28]

LSC thin films are frequently used as model electrodes in studies of the oxygen reduction kinetics.[29-32] Several techniques such as PLD,[16, 33, 34] magnetron sputtering [15, 35] or sol-gel-deposition [36, 37] can be employed to deposit LSC thin films on yttria stabilized zirconia (YSZ) at sufficiently low temperatures to avoid reactions at the interface. The preparation method and parameters are vitally important in order to obtain and sustain high oxygen exchange activity and they strongly affect morphology, microstructure and interfacial chemistry of LSC electrodes.[38-41] PLD-prepared thin films may also improve the performance of SOFC electrodes[19] and recently it was shown that LSC thin film electrodes deposited by PLD at comparatively low temperatures may exhibit polarization resistances as low as 0.1 Ωcm^2 at 600°C.[42] However, drastic effects of PLD deposition conditions, annealing time and annealing temperature on the polarization resistance and also significant variance in values of polarization resistance which are reported for almost the same LSC composition[34, 42-45] raise the question of chemical reasons behind such strong variations.

PLD was used to deposit La$_{0.6}$Sr$_{0.4}$CoO$_{3-\delta}$ thin film electrodes on YSZ (100) single crystals. The goal is to find correlations between the chemical surface composition of these LSC thin films and their electrochemical properties. ToF-SIMS was employed to investigate the near surface region of differently prepared or annealed electrodes with respect to possible differences in cation composition. Additionally, a special test assembly was set up for in-situ analysis of the eluate from etched thin film electrodes using inductively coupled plasma - optical emission spectrometry (ICP-OES). This

technique revealed further information on the quantity of cation segregations and on the relationship between surface composition and electrode polarization.

2.1 Experimental

2.1.1 Sample preparation

$La_{0.6}Sr_{0.4}CoO_{3-\delta}$ was synthesized by the nitrate/citrate (Pechini) route.[42, 46] The LSC powder was calcinated at 1000°C for 20 h, and then a pellet was pressed, sintered for 12 h at 1200°C in air and used as target for the PLD process. LSC was deposited on polished YSZ (100) single crystals (CrysTec GmbH, Germany) using a KrF excimer laser ($\lambda = 248$ nm, COMPex Pro 101 F, Lambda Physics, Germany). The laser beam energy was set to 400 mJ per pulse at 5 Hz pulse frequency. The deposition was performed in 0.4 mbar O_2 atmosphere. The surface temperature of the heated substrate was monitored by a pyrometer (Heitronics KT-19.99, Germany) and deposition temperatures of 450°C and 650°C were used in this study. The film thickness (100-200 nm) was controlled via deposition time and measured by SEM and digital holographic microscopy (DHM Lyncée Tec, Switzerland) of SIMS-craters. The cation compositions of the resulting films were determined by chemical analysis (ICP-OES) of dissolved films and a cation composition of $La_{0.60(1)}Sr_{0.42(2)}Co_{0.98(2)}$ was found, which is very close to the nominal one. For impedance measurements circular microelectrodes with diameters of 200 μm, 100 μm, 80 μm and 50 μm were prepared from the thin films by photolithography and subsequent ion beam etching with 2 keV Ar^+ ions.

2.1.2 Characterization

The focus was set on the correlation between the electrochemical behavior and the surface composition of LSC thin films deposited at two different temperatures, 450°C

and 650°C. The influence of annealing at 600°C in air and the effect of chemical etching with diluted hydrochloric acid were studied. Electrochemical impedance spectroscopy (EIS) measurements were performed with an Alpha-A high performance frequency analyzer (Novocontrol Technologies, Germany). Impedance spectra were recorded on microelectrodes with 10 mV AC amplitude at 600°C in air without DC bias. The setup for microelectrode measurements is described in Ref. [47].

SIMS investigations were carried out on a ToF.SIMS 5 instrument (ION-TOF GmbH, Münster, Germany). Bi_3^+ clusters in high current bunched mode were used as primary ions, positive secondary ions were analyzed. O_2^+ ions were utilized in the sputter gun for depth profiling. Typical beam currents, voltages and areas used were 25 keV, 36 pA, 100×100 μm² for Bi_3^+ and 500 V, 100 nA, 300×300 μm² for O_2^+.
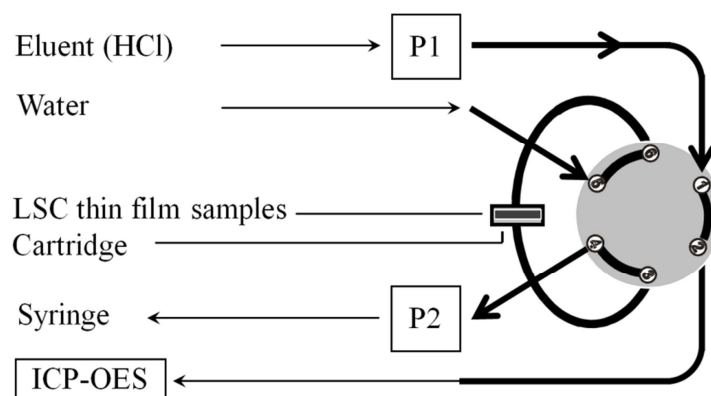
Figure 4: Sketch of the set-up used for etching analysis/profiling by ICP-OES. Purified water was drawn into the cartridge with a syringe at the beginning of a measurement (P2) and to stop the etching process. The etching process was started by turning the 6-way-valve. A constant flow of diluted HCl (1.0 ml/min) was then applied through the etching cartridge by a peristaltic pump (P1). The eluate was analyzed on-line by ICP-OES.

For chemical etching analysis, a flow injection system coupled to ICP-OES (iCAP 6500 Thermo Scientific, USA) was employed (Fig. 4). 5×5 mm² samples – YSZ with 100 nm LSC thin films - were placed inside a small teflon cell. First the cell was filled with

purified water. After starting the ICP-OES measurement, a constant flow of 1.0 ml/min diluted hydrochloric acid (0.06 mol/l and 0.12 mol/l allowing different etching speed) was applied through the cell. The eluate was directly introduced into the nebulizer of the detection system. Strong emission lines of the elements La (333.7 nm, 379.4 nm, 419.6 nm), Sr (216.5 nm, 346.4 nm, 421.5 nm), and Co (228.6 nm, 238.8 nm) were analyzed. Cation signals from the film were measurable after a dead time required for the purified water to be rinsed from the etching cell. Etching speed then increased and dropped again when most of the film was dissolved. After dissolving the entire LSC film the cation content in the eluate dropped to almost zero as YSZ is insoluble in diluted HCl and thus neither Y nor Zr were detected in the eluate. The surface and cross-sectional microstructures of the LSC-films were investigated on FEI Quanta 200 field-emission gun scanning electron microscope.

2.2 Results and Discussion

2.2.1 AC impedance

A typical impedance spectrum obtained for 200 μm LSC microelectrodes on YSZ can be found in Fig. 5. In an earlier study [48] it was shown that the equivalent circuit in Fig. 5, theoretically derived in Ref. [49], is often appropriate to quantify impedance spectra on mixed conducting electrodes with high ionic conductivity. This equivalent circuit, which includes resistors R and capacitors or more general constant phase elements Q, was also used for fitting the data of this study. In accordance with Ref.[48] the low frequency arc can be assigned to the oxygen exchange at the electrode surface, while the higher frequency semicircle is associated with the LSC-YSZ interface. The high frequency axis intercept is attributed to the ionic transport in the YSZ single crystal.
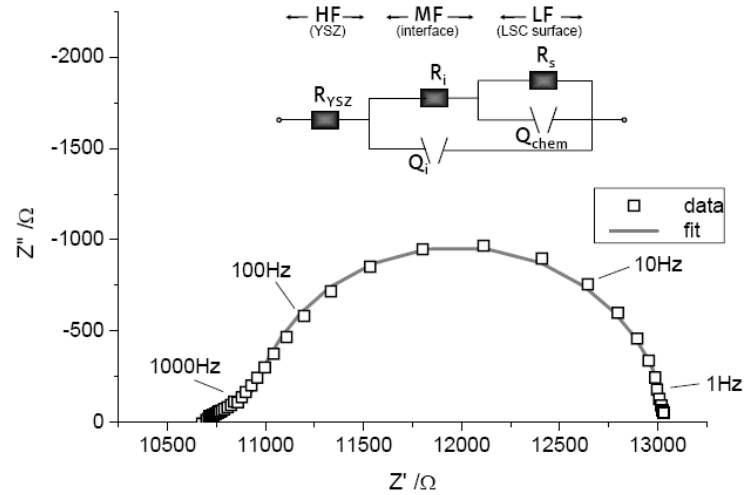
Figure 5: Impedance spectrum measured at 600°C and corresponding fit for a circular 200 μm LSC microelectrode on YSZ and equivalent circuit used for the fit. The symbol Q denotes a constant phase element.
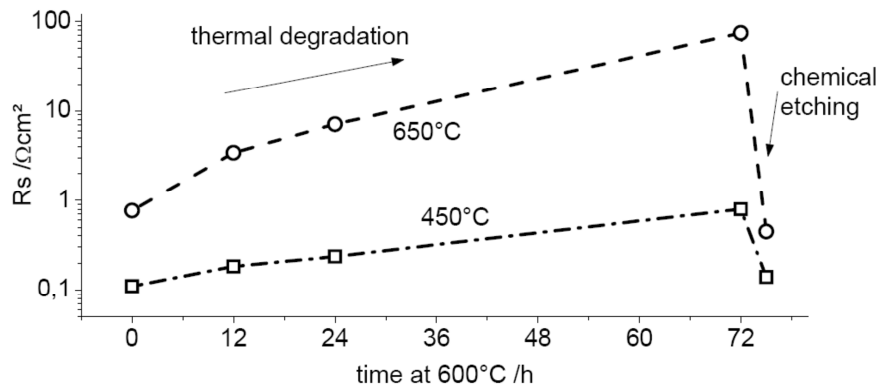
Figure 6: Surface polarization resistance R_S of LSC thin film electrodes deposited at 450 and 650°C measured at 600°C in air. Changes of R_S with annealing time at 600°C and after chemical etching are displayed.

Thermal degradation was studied at 600°C in air for samples that were prepared at different substrate temperatures in the PLD process, 450°C and 650°C respectively. It was already shown in an earlier study [42] that surfaces of thin LSC electrodes of 40-

200 nm thickness can be catalytically highly active right after preparation but may also show rapid degradation with very thin films deposited at higher temperatures degrading to substantially higher polarization resistances. This is confirmed in our study: The low frequency semicircle (electrode surface resistance R_S) is strongly affected by thermal annealing at 600°C, whereas the high frequency semicircle (LSC|YSZ interface resistance R_i) remains almost unchanged. Typical values of R_S are shown in Fig. 6: Deposition at 450°C leads to cathodes exhibiting polarization resistances R_S of ca. 0.1 Ωcm^2 immediately after heating to 600°C and ca. 0.8 Ωcm^2 after 72 hours. Films deposited at 650°C also start with rather low R_S values of about 0.7 Ωcm^2 but degrade by a factor of 100 within 72 hours.

2.2.2 Effect of chemical etching on the AC impedance

Chemical etching with diluted hydrochloric acid (1 mol/l HCl for 15 min) was found to have a huge effect on the polarization resistance of $La_{0.72}Sr_{0.18}MnO_3$ (LSM) electrodes [23]. Much softer conditions (0.12 mol/l HCl, etching for 5 s) were used in this study as LSC dissolves quicker in HCl than LSM. The amount of material removed from the electrode surface under given etching conditions was quantified by ICP-OES and corresponds to about 5-10 nm. Etching resulted in a drastic decrease of the electrode polarization resistance in case of degraded LSC electrodes. However, only the low frequency semicircle in Nyquist plot was affected by the etching procedure, which is strong further evidence that this semicircle in fact corresponds to a surface process. This is exemplified in Fig. 7: After annealing for 1 to 3 days large resistances are found (main arcs), which drastically decrease after etching (magnification in Fig. 7). After etching, surface resistances reached similar and very low values even if there was a degradation induced difference in R_S of orders of magnitude before etching. This suggests that only the very near surface area, which was removed by etching, was affected by degradation. Thus by etching a new LSC surface can be obtained which exhibits very high electrochemical activity. This is regarded as an indication that LSC perovskite surfaces inherently have fast oxygen exchange kinetics but chemical changes may strongly lower their catalytic activity. Below results are presented that

support this hypothesis and correlate these property changes with chemical changes at the surfaces. It should be mentioned that after etching and thus recovering a degraded LSC electrode high activity could only be found immediately after heating to 600°C. The subsequent degradation was observed to be faster than for as prepared films (Fig. 6).
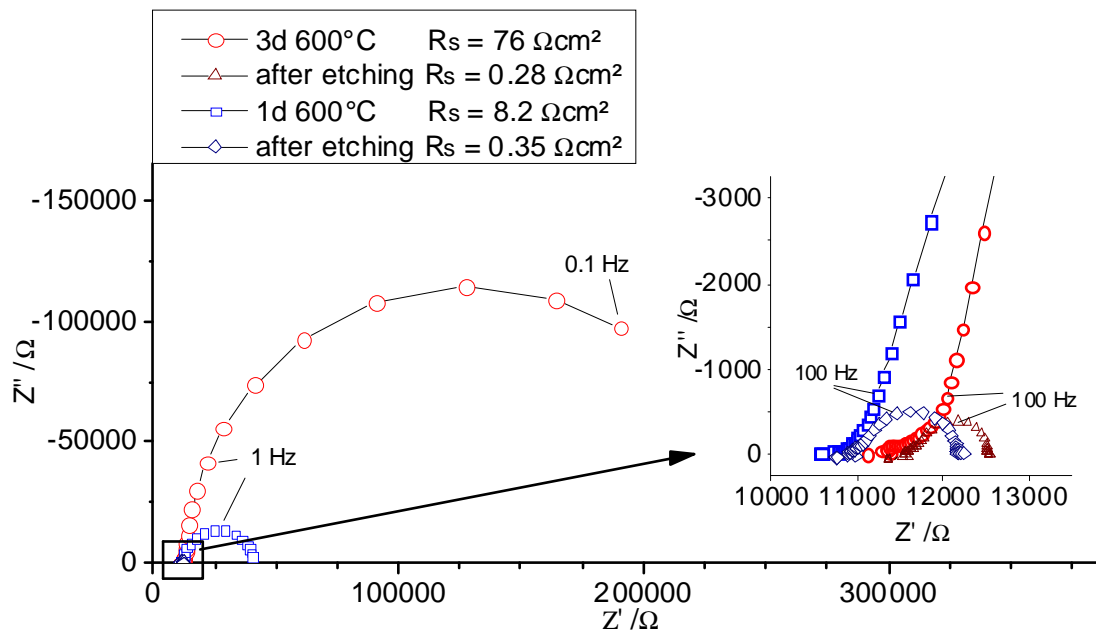

Figure 7: EIS spectra measured at 600°C on 200 μm microelectrodes prepared at 650°C after 1 or 3 days of annealing respectively before and after subsequent chemical etching: The surface resistance R_S returns to very low values (under 1 Ωcm²) after etching almost independent of previous thermal degradation of R_S.

2.2.3 ToF-SIMS analysis of the LSC films

The challenge with SIMS analysis of the cation composition of LSC was to distinguish measuring artefacts that can occur due to matrix effect, ionic mixing and preferential sputtering [50] from real changes in composition. Especially the surface region is

problematic as the chemical environment of the surface changes with ion bombardment until a steady state is reached [51, 52]. While the absolute values of the secondary ion signals are therefore extremely difficult to interpret correctly, differences found between different LSC samples can be expected to reflect true effects and can thus give useful data about surface composition. From this viewpoint, only differences between the secondary ion signals of different LSC films are considered and can be interpreted unambiguously.

In Fig. 8 ToF-SIMS depth profiles of the secondary ions O^+, Co^+, Sr^+, and La^+ of LSC thin films prepared at 450°C and 650°C after deposition, after annealing, and after annealing plus chemical etching are displayed. Samples were measured using very low sputter ion doses in order to obtain a reasonable depth resolution. The focus was laid on the near surface region, i.e. the top 30 nm of the films. Significant differences between the cation intensities in different LSC thin films were found. As discussed above, time (and thus depth) dependent secondary ion intensities in a given film do not necessarily reflect a true depth dependence of the corresponding ion in LSC. Some features as the very high signals of cobalt and lanthanum or the lower signals for strontium (and also oxygen) in the very first measuring points are observed in all measured LSC depth profiles. It is highly probable that those general features are SIMS related artifacts. However, several distinctive qualities such as an increase of the Sr signal in the first 50 sputter seconds or the shape of the intensity curve of the La signal are reproducibly different for LSC thin films of different prehistory. This is a very strong indication that these differences in the secondary ion signals correspond to real compositional changes close to the LSC surface.

By relating the cation signal intensities to the value in the bulk LSC (Fig. 9), changes at the surface are easier distinguishable. The relative Sr^+ signal is very close to 1 throughout the entire layer for the 450°C deposited LSC film and both etched films (cf. Figs. 9a, c, f). The other thin films show a clearly higher Sr^+ signal close to the surface (cf. Figs. 9b, d, e). Also differences in the La^+ and Co^+ signal are visible though a systematic relation to sample prehistory is not obvious.
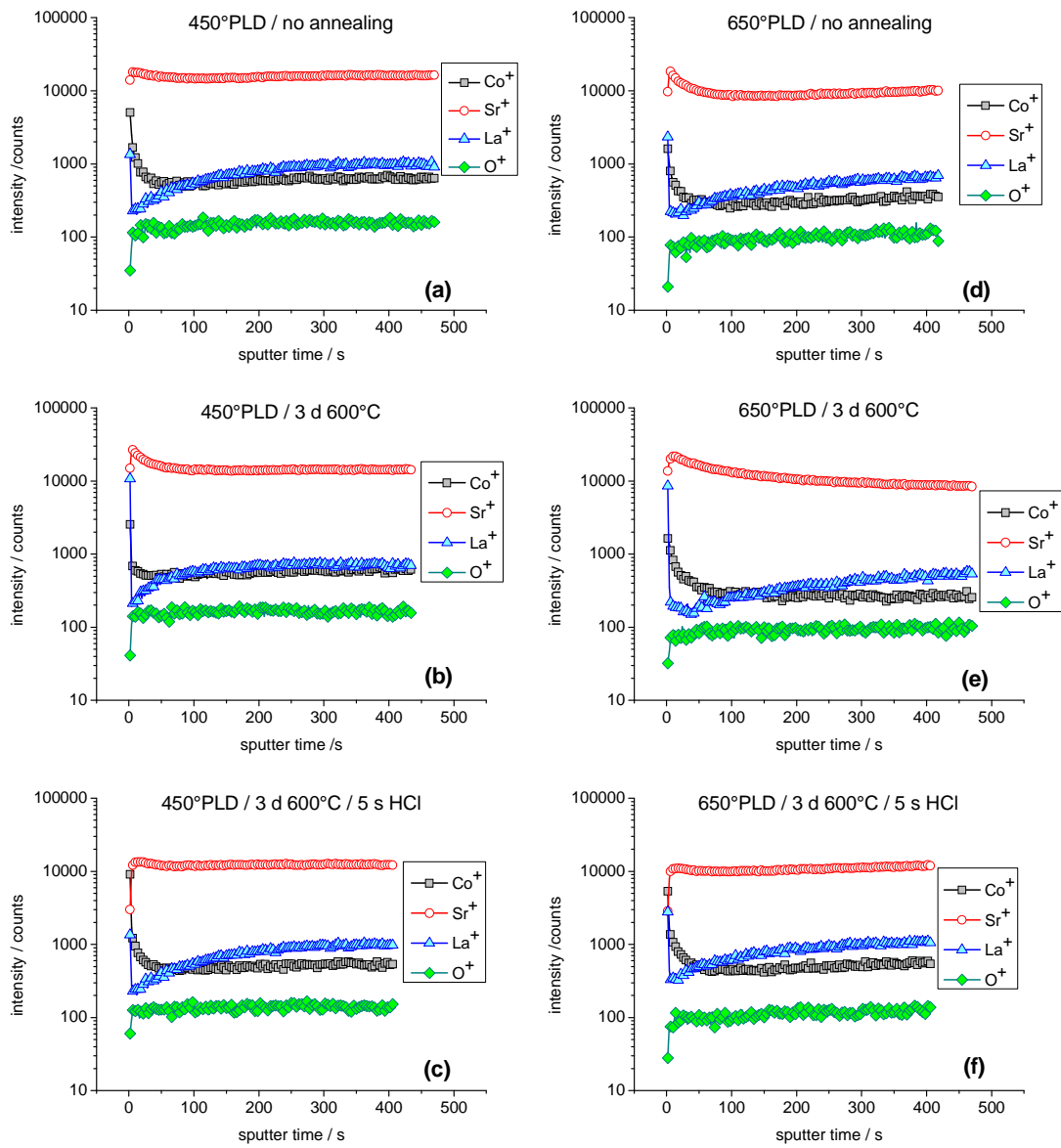
Figure 8: Positive secondary ion signals of different LSC films prepared at 450°C (left side) and 650°C (right side), respectively, before annealing (a, d), after 3 days at 600°C (b, e) and after such an annealing and subsequent chemical etching (c, f): positive secondary ion signals are displayed. 100 s sputter time correspond to about 8 nm in depth. Biggest differences between samples were found within the first 100 s.
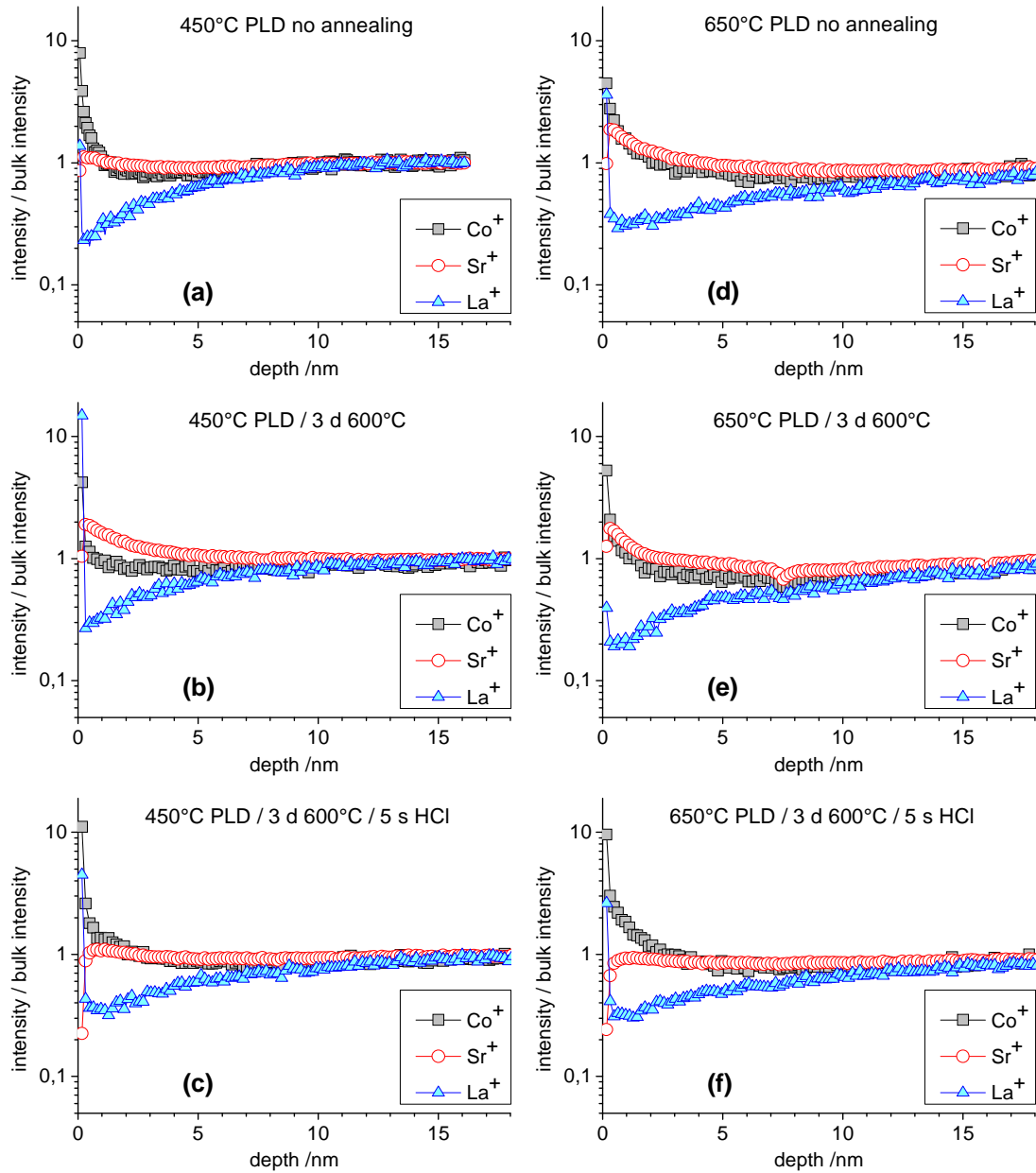
Figure 9: Relative ion signals (bulk intensity = 1) in the first 200 sputter seconds of different LSC films prepared at 450°C (left side). LSC films before annealing (a, d), after 3 days at 600°C (b, e) and after such an annealing and subsequent chemical etching (c, f): positive secondary ion signals are displayed.
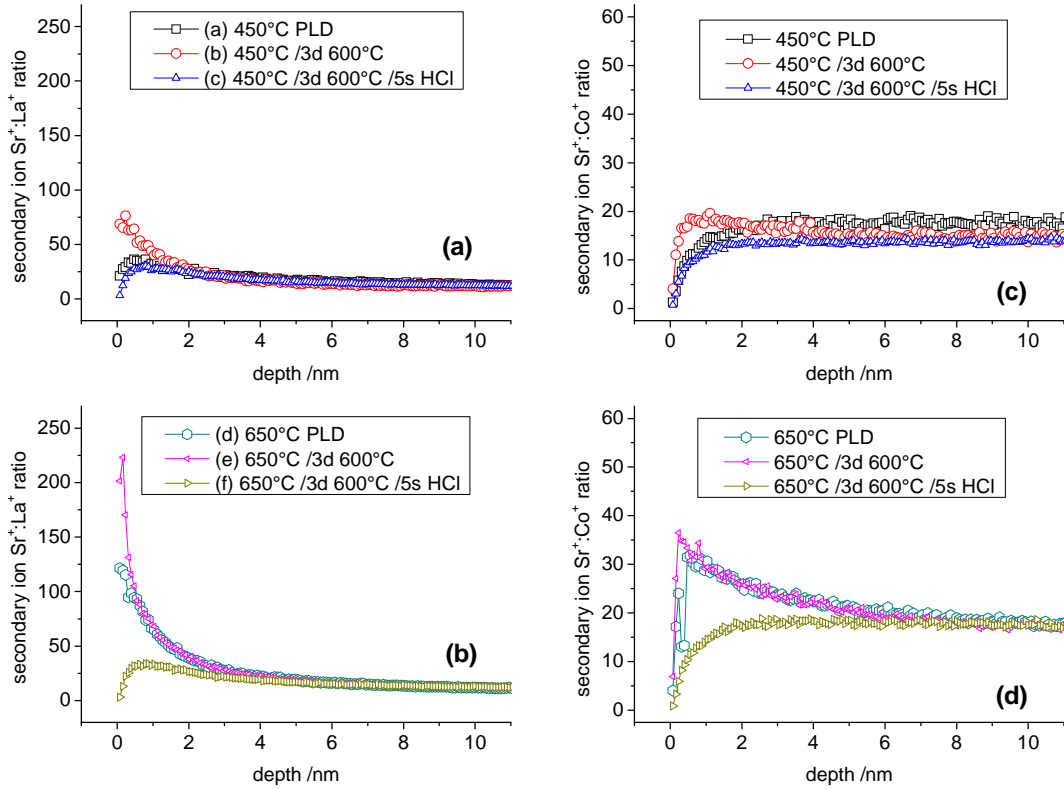
Figure 10: Secondary ion ratios from SIMS raw data for the films in Figs. 8 and 9. $Sr^+:La^+$ ratio for films prepared at 450°C (a) and 650°C (b) and $Sr^+:Co^+$ ratio for the same films (c, d). An increase in both ratios as observable in the 450°C deposited and annealed film and even stronger in both the 650°C deposited as prepared and 650°C deposited and annealed LSC films indicates a Sr enrichment at the surface.

Systematic variations become even more obvious in Fig. 10 when plotting the secondary ion ratios of $Sr^+ : La^+$ (a) and $Sr^+ : Co^+$ (b). Significant differences are found only in the topmost 2-5 nm of LSC thin films. An increase of both ratios at the surface of the 650°C deposited sample and at the surfaces of both annealed films give a strong indication for Sr enrichment on those LSC surfaces. The as-prepared 450°C deposited thin film and both etched samples show very similar and low $Sr^+:La^+$ and $Sr^+:Co^+$ signal ratios close to the surface. This indicates that the surface composition after preparation at low temperatures is similar to the surface composition after etching, which is expected to be close to bulk composition (see also ICP-OES results).

Interestingly, compositional similarities found by ToF-SIMS are reflected in the electrochemical properties: The three films exhibiting similar secondary cation ratio profiles all showed very fast oxygen reduction kinetics in impedance measurements. Films with a pronounced increase of the Sr^+:La^+ intensity ratio toward the surface all have higher polarization resistances with the highest R_S belonging to the sample with the highest Sr^+:La^+ signal ratio. However, a 1:1 correlation between Sr^+:La^+ signal increase and extend of the R_S increase is not possible.

It is detailed below (ICP-OES measurements) that the three highly active films exhibiting similar Sr^+:La^+ signals are thought to be close to an undisturbed, stoichiometric LSC surface. Hence, these correlations further suggest an intrinsically very low polarization resistance for oxygen reduction on LSC perovskite, but also a strong tendency for modification of those surfaces even at the moderate temperature of 600°C. These changes, which come along with Sr enrichment at the surface, also seem to be either responsible or an indication for degradation of the oxygen reduction activity. Cation ratios from SIMS depth profiling suggest that at most the top 5 nm of the films were affected by degradation.

Two mechanisms are conceivable leading to Sr enrichment at the surface: Sr segregation within the perovskite structure resulting in Sr enrichment on the A-site in the near surface region, or formation of a new Sr-rich phase at the LSC surface. The formation of SrO-rich phases has already been suggested and observed on the surface of other Sr-containing perovskites such as $(La,Sr)MnO_3$ [23, 53-56] or $SrTiO_3$ [57-59] and in several cases a decrease of the catalytic activity of an electrode was attributed to Sr segregation. Thus the latter mechanism seems more probable.

In Fig. 10 it is shown that differences in the Sr^+:La^+ intensities are most pronounced in the first 2 nm while Sr^+:Co^+ differs in about 5 nm. This might indicate additional changes in Co content due to segregation but a more detailed correlation is not possible based on these data. Therefore we also refrain from speculating how exactly cation redistribution lowers the oxygen reduction rate.

2.2.4 ICP-OES

Differences in the chemical composition of the near surface region of LSC films were further investigated by ICP-OES. The usual approach would be to analyze the solved cations in the eluate remaining after a chemical etching procedure. However, this gives only information about the averaged stoichiometric composition of the eluate after a given etching procedure. A new approach was therefore performed in this study by in-situ etching with a constant flow of eluate and simultaneous on-line ICP-OES measurement. Compositional profiles of very high depth resolution could thus be obtained.
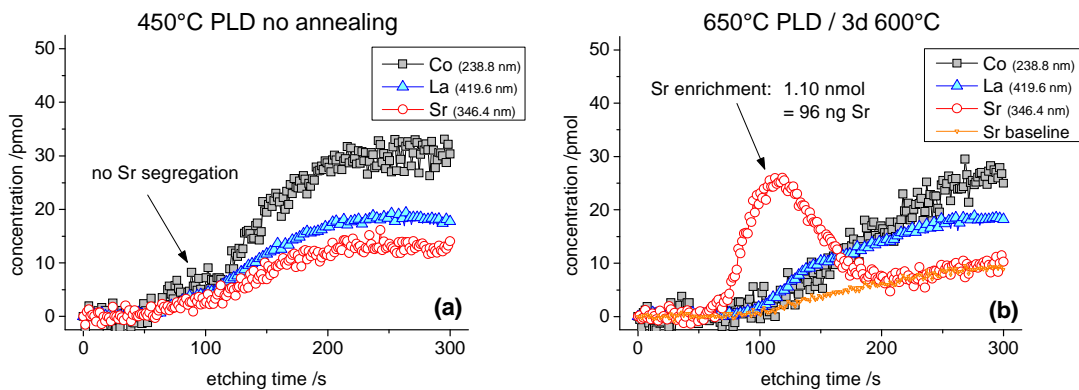
Figure 11: Chemical etching profiles (0.06 mol/l HCl) from the surface area of LSC thin films measured by ICP-OES: Sr enrichment is visible in the 650°C deposited and degraded thin film annealed at 600°C for 3 days (b). No such enrichment is found in 450°C deposited films before annealing (a). A Sr-baseline regarding the changes in etching speed during the measurement is used for quantification.

Fig. 11 shows the etching ICP-OES profiles (0.06 mol/l HCl) of the two thin films with the biggest difference in polarization resistance and therefore the biggest expected difference in surface composition (450°C PLD no annealing, 650°C PLD 3 d 600°C). Owing to starting the detector before starting the etching of the sample and the dead

time of the set-up (Fig. 11) the first cations of the films were detected after ca. 60 seconds. Calibration of the measured intensity was performed by standard solutions of different concentrations of La, Sr and Co applied into the same set-up via a tube containing exactly 200 μl.
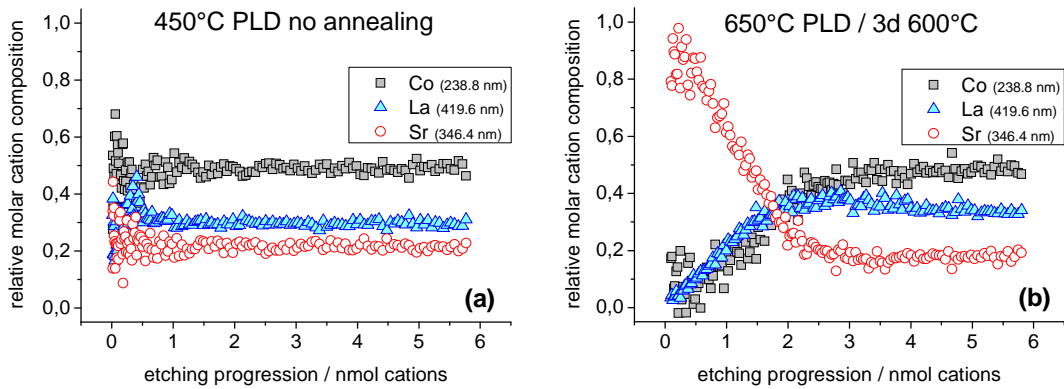
Figure 12: Relative molar cation composition of the surface area of LSC thin films from chemical etching (Fig. 11) is displayed vs. etching progression in nmol cations. For given sample size and ideal perovskite La$_{0.6}$Sr$_{0.4}$CoO$_{3-\delta}$ 1 nmol cations is equivalent to about 0.9 nm film thickness. A very uniform cation composition close to 0.5 Co, 0.3 La, 0.2 Sr as expected from stoichiometry was found in case of the thin film deposited at 450°C (a). Inhomogeneous molar composition (b) was measured in thin films deposited at 650°C and annealing for 3 days. After a strong Sr enrichment at the surface, a weak La enrichment is found deeper below the surface. Co is depleted in the whole surface area.

In Fig. 12 the relative molar compositions of the cations calculated from the measurements in Fig. 11 are displayed vs. etching progression. The low temperature deposited film without annealing showed a constant cation composition very close to the nominal values (La 0.3, Sr 0.2, Co 0.5) throughout the entire near surface region (Fig. 12a). 6 nmol etched cations correspond to an etched thickness of about 5.5 nm LSC. This constant signal is another strong indication that such a LSC film indeed shows the nominal bulk composition up to the surface. Moreover this also strongly suggests that preferential etching of a cation in the perovskite-type LSC does not play

an important role: A constant signal as seen in Fig. 12b would require an exact counter balancing of preferential etching and compositional variation which is highly unlikely.

In case of thermally degraded samples a high amount of Sr at the beginning of the etching process (Figs. 11b, 12b) was found together with depletion of Co in the whole surface region. La is also depleted in most of the Sr enriched zone but exhibits a slight hump before a level close to bulk composition is reached. It is also worth mentioning that after the Sr peak a Sr level slightly lower than in Fig. 12a is found and even after etching ca. 6 nmol of cations (ca. 5.5 nm) stoichiometric bulk composition is not exactly found. This might indicate that two different phases are present, a Sr rich surface phase and a slightly Sr depleted bulk phase. Occurrence of the Sr peak corresponds well with the Sr enrichment at the surface concluded from SIMS measurements (compare Figs. 10, 11). The huge difference seen in Fig. 12 was reproduced on several samples. Additional experiments with higher etching rates (0.12 mol/l HCl) confirmed these results and further showed that the Sr peak can be found not only in 650°C deposited and annealed LSC films but also in 450°C deposited and annealed samples and in 650°C deposited . For films after etching (0.12 mol/l HCl for 5 s in a beaker) no such Sr-peak was observed, consistent with the homogeneous composition found in all films after a certain etching time. From Fig. 11b the Sr enrichment for a 650°C deposited and annealed film was quantified to be 96 ng for a 5×5 mm^2 sample relative to the Sr baseline extrapolated. Assuming SrO as the Sr enriched species this would be equivalent to 0.95 nm of a dense SrO layer at the surface (more than two elementary cells). However, this layer does not have to be dense (i.e. may also be thicker without covering the entire surface). Accordingly, some selective etching of this phase compared to exposed perovskite LSC might take place. The SrO composition of the top layer is only one possibility; $SrCO_3$ can also explain the Sr enrichment.

2.2.5 Scanning Electron Microscopy

SEM images (Figs. 13a-d, 14a-d) were used to compare the microstructure of the LSC surfaces obtained at deposition temperatures of 450°C (Fig. 13) and 650°C (Fig. 14). The images were taken directly after deposition (Figs. 13a, 14a), after annealing for 3 days at 600°C (Figs. 13b, 14b), after chemical etching of annealed films with 0.06 mol/l HCl for 5 s (Figs. 13c ,14c) and for 20 s (Figs. 13d, 14d). HCl with lower concentration was used for practical reasons here. ICP-OES measurements showed that by etching with 0.06 mol/l HCl for 20 s an equal amount of material is dissolved from the surface than by the standard etching procedure (0.12 mol/l HCl for 5 s).
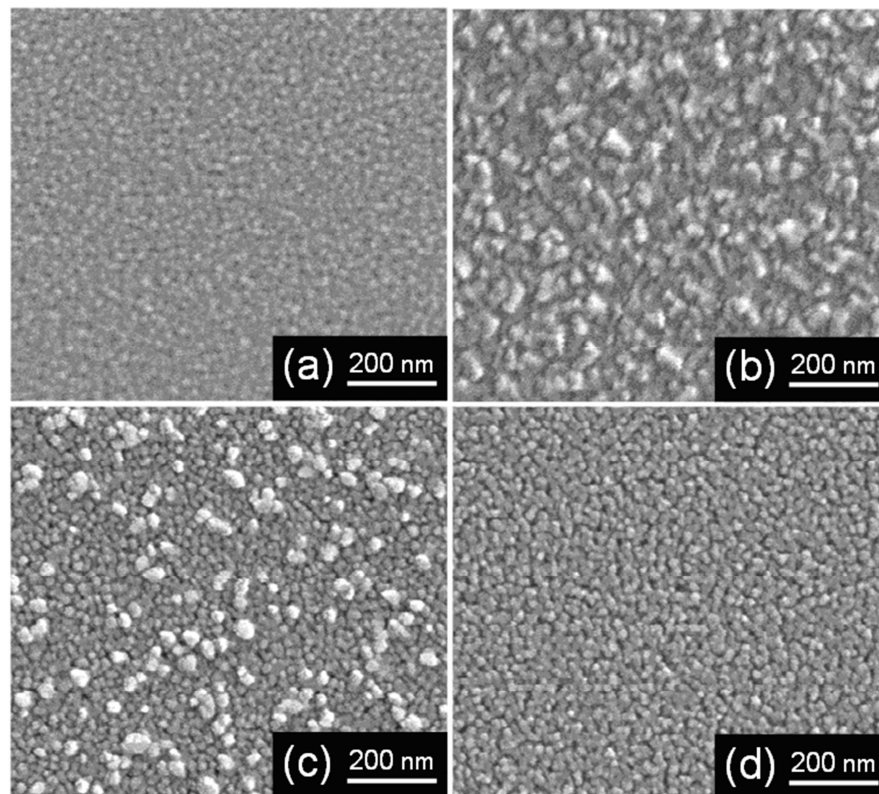
Figure 13: SEM images of LSC thin films deposited at 450°C: after deposition (a), after annealing for 3 d at 600°C (b), after annealing and extremely soft etching 5 s 0.06 mol/l HCl (c), after annealing and etching 20 s 0.06 mol/l HCl (d).
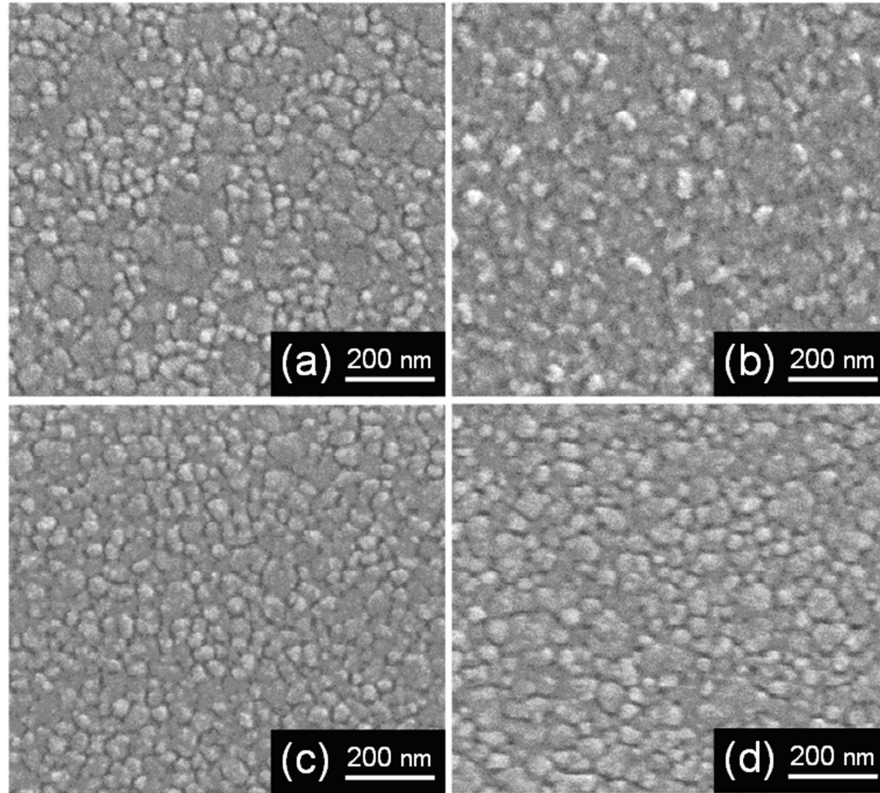
Figure 14: SEM images of LSC thin films deposited at 650°C: after deposition (a), after annealing for 3 d at 600°C (b), after annealing and extremely soft etching 5 s 0.06 mol/l HCl (c), after annealing and etching 20 s 0.06 mol/l HCl (d).

Before annealing, a nanocrystalline microstructure is visible for both films with grain sizes of ca. 20–30 nm and 40–70 nm for 450°C and 650°C deposition temperature respectively. For 450°C deposition temperature a significant difference is found between the electrochemically very active as-prepared thin film (Fig. 13a) and the thermally degraded thin film (Fig. 13b). Newly formed grains of about 50 nm diameter are visible after annealing. These grains are reduced in amount and size after extremely slow etching for 5 s (Fig. 13c) and completely removed after etching for 20 s (Fig 13d). The microstructure in Fig. 13d is very close to the original microstructure (Fig. 13a) as is the polarization resistance in impedance spectra. A very similar result was achieved for thin films prepared at 650°C. The original surface structure (Fig. 14a) changes after annealing and newly formed grains become visible (Fig. 14b). These

grains are removed by chemical etching (Figs. 14c, d) and a microstructure very similar to the structure directly after deposition is obtained. In case of 650°C deposition temperature the film looks very dense while in the case of 450°C pores might be present. It is plausible to assume that segregation of the cations during annealing is closely related to the observed precipitates even though absence of visible precipitates does not necessarily indicate absence of any Sr enrichment at the surface.

Combining all results gives evidence that a LSC perovskite surface is intrinsically highly active with respect to oxygen exchange or oxygen reduction while degradation of the performance is related to segregation of a Sr rich secondary phase. Especially when preparing electrodes above 600°C this segregation might have happened already before first electrochemical measurements and the full catalytic potential of LSC is never observed. Accordingly, many LSC electrodes used in the literature might have failed in exploiting the full catalytic potential of LSC surfaces.

This hypothesis raises the question how the segregation could be strongly reduced. Lower deposition temperature of PLD films leads to films with slower degradation (cf. Fig. 6 and Ref.[42]). Also in SEM images the segregated second phase seems to not yet fully cover the surface after 3 days of annealing. Reasons for this are not known yet but may be correlated with the low crystallinity of such films: In Ref.[60] these films did not exhibit significant XRD signal intensities. It has to be tested in the future in how far low deposition temperatures, low operation temperatures or also deposition of a very thin Sr lean layer onto the surface may suppress degradation for sufficiently long periods and thus helps keeping LSC at its high catalytic activity.

2.3 Conclusions

The surface related polarization resistance of $La_{0.6}Sr_{0.4}CoO_{3-\delta}$ thin film electrodes not only depends on the preparation temperature and shows in some cases pronounced degradation during annealing at 600°C. Chemical etching with diluted hydrochloric acid is able to undo the thermally induced increase of polarization resistance by renewing the electrode surface. ToF-SIMS depth profiles showed differences in the near

surface cation composition of films which went through different pre-treatments. A correlation of compositional changes and polarization resistance is found: Both secondary ion signal ratios, $Sr^+:La^+$ and $Sr^+:Co^+$ were found to be increased in electrochemically inactive LSC thin films indicating an impedimental Sr segregation to the surface in those films.

By in-situ chemical etching analysis with ICP-OES the change in surface composition could also be observed and further quantified. While electrochemically active thin films showed a very uniform cation composition up to the surface, Sr segregation to the surface and cobalt depletion in the surface region were found in degraded LSC films. Changes in cation distribution were quantified to be in the range of 0.5 $\mu g/cm^2$ and Sr enrichment corresponds to about 1 nm in thickness assuming a dense SrO film. In high resolution FEG-SEM images the formation of grains at the surface was observed in case of thermally degraded LSC films. The activating effect of chemical etching was found to be associated with removing this newly formed phase at the surface. These results thus suggest that LSC inherently exhibits very high catalytic activity towards oxygen reduction but becomes less active due to Sr-rich segregations or a phenomenon accompanying this segregation. Stoichiometric perovskite type LSC surfaces seem to form at low PLD deposition temperatures or by chemical etching, but it has to be further clarified whether or not it is possible to stabilize those surfaces by suppressing segregation of Sr-rich phases. In order to further investigate the reasons and kinetics of these segregation effects, the mobility of cations in LSC which is necessary for Sr segregation is the topic of the following chapter.

3 Cation Diffusion in La$_{0.6}$Sr$_{0.4}$CoO$_{3-\delta}$ Thin Films at Temperatures below 800°C

This chapter contains in large part material submitted as scientific paper to the journal Physical Chemistry Chemical Physics.

As mentioned above, MIEC perovskite-type oxides such as LSC are attractive cathode materials for intermediate SOFC operation at temperatures below 700°C. Under these operation conditions, perovskite oxides are usually considered to consist of stiff cation lattices with mobile oxide ions. However, although oxygen mobility is indeed many orders of magnitude higher, cation mobility cannot be neglected even at these moderate SOFC operation temperatures. This can be concluded from the segregation phenomena presented in the last chapter, and also from similar phenomena reported in literature[16, 25, 26, 61] or from changes of the surface termination of (La,Sr)(Cr,Mn)O$_{3-\delta}$[62] well below 700°C. On the other hand, experiments directly probing the cation mobility and measuring diffusion coefficients of cations are mostly restricted to temperatures of 900-1500°C.[63-75] Typically, in these studies on bulk samples, Arrhenius-type temperature dependencies of the cation diffusion coefficients are observed with activation energies in the range 2–4 eV.

Several types of experiments can be employed to determine the diffusion coefficients of cations in perovskite-type oxides. One technique uses two polished bulk samples (often called diffusion couples), which are brought into contact and are then heated to high temperatures. There, the kinetics of a solid state reaction[63-65] forming a third phase at the interface, or diffusion profiles of one or more species crossing the phase boundary[66, 67, 76] can be investigated. Other experiments use only one polished bulk sample and fabricate a thin tracer source on top, either by applying a solution that is later dried,[68-74] by pulsed laser deposition,[77] or by ion implantation.[75] Cation diffusion profiles are subsequently generated by annealing for a certain time at constant temperature. In all cases the resulting cation distribution is analyzed either by

SIMS, by electron microscopy and energy dispersive X-ray spectroscopy (EDX), or *via* the radiation emitted from radioactive tracer isotopes.

The diffusion lengths in all these experiments have to be considerably longer than the roughness of the sample surfaces and interfaces and the depth sensitivity of the detection method. Often, diffusion lengths in the range of several 100 nm to 50 μm are aspired, which is the reason for usually choosing high temperatures in such diffusion experiments. In order to determine diffusion coefficients at lower temperatures it is necessary to measure very short diffusion profiles with high accuracy. This is possible by depth profiling with ToF-SIMS and requires a very good quality of surfaces and interfaces. Thin films grown by PLD on epitaxial-polished single crystalline substrates can help obtaining such smooth surfaces and interfaces.[78] Depositing two or more of these layers on top of one another yields high quality "thin film diffusion couples". Owing to the small diffusion lengths which can be investigated in such samples, cation diffusion may be studied at lower temperatures than with conventional samples.

Here this type of diffusion experiment is applied to analyze the cation diffusion in $La_{0.6}Sr_{0.4}CoO_{3-\delta}$ thin films at 625-800°C by using different isotopic ($^{86}Sr/^{88}Sr$) and elemental tracers (Co/Fe, La/Sm). Thus, experiments were performed at the typical temperatures employed in SOFCs during operation. This gives us the possibility to also investigate the relationships between cation mobility, reaction kinetics of the oxygen exchange, and segregation effects found in such LSC thin films when used as model SOFC cathodes.

3.1 Experimental

3.1.1 Sample preparation

Powders of the desired cation compositions were prepared via the nitrate/citrate (Pecchini) route. The following high purity base materials were applied to ensure a low level of impurities: Co 99.995%, Fe 99.999%, $SrCO_3$ 99.995%, La_2O_3 99.999%, Sm_2O_3

99.9%, HNO_3 70% in H_2O, 99.999% purity, Citric acid monohydrate 99.9998% (all Sigma-Aldrich), $SrCO_3$ 99.99%, 96.4% [86]Sr isotope-enriched (Trace Sciences, Canada). PLD targets were produced by isostatic pressing (5.2 kbar, 2 min) and sintering (1150°C, 12 h). As very slight deviations in composition (~1-2%) were observed between an LSC target and a PLD thin film deposited from the target,[79] powder compositions were optimized such that the thin films had the desired stoichiometry. Three different powder compositions were prepared, one to obtain thin films of the natural isotope composition $La_{0.6}Sr_{0.4}CoO_{3-\delta}$ (LSC), one [86]Sr-tracer enriched $La_{0.6}{}^{86}Sr_{0.4}CoO_{3-\delta}$ (L[86]SC), and one containing 90% of the same composition as the LSC target and 10% tracer of all cations (Sm, [86]Sr, Fe) to yield the stoichiometry $La_{0.54}Sm_{0.06}Sr_{0.36}{}^{86}Sr_{0.04}Co_{0.9}Fe_{0.1}O_{3-\delta}$ (LSC-T10).

All thin films were prepared on $10 \times 10 \times 0.5$ mm³ (100) YSZ single crystals (9.5 mol% Y_2O_3, Crystec, Germany) by PLD. A KrF laser (COMPex Pro 101F, Lambda Physics, Germany) set to 400 mJ per pulse and 10 Hz was used. The deposition was performed in 0.04 mbar O_2, the heated substrate was positioned 6.7 cm from the target. Two different substrate temperatures, 450°C and 600°C, were employed during deposition - measured with a pyrometer (KT-19.99, Heitronics, Germany). This lead to dense thin films with different microstructures subsequently denoted as LSC-LT (450°C) and LSC-HT (600°C). Growth rates of 6-7 nm min⁻¹ were realized with these parameters. By variation of the deposition time, films of different thickness (50-200 nm) were deposited. A rotatable 3-target-holder allowed changing targets during deposition. In this way several bi- and multi-layers of LSC and LSC + tracer were deposited for the subsequent diffusion experiments. In Fig. 15, a sketch of the sample geometries is given. Symmetric 3- and 4-layered structures as shown in Fig. 15a with different layer sequence and thickness were used to investigate existence of any depth dependence of the diffusion coefficients in a 200 nm LSC film. Bilayers of the sequence YSZ|LSC|LSC + tracer and of ~100-200 nm layer thickness as shown in Fig. 15b were used to quantify the tracer diffusion coefficients.

a)   b)

☐ LSC ☐ LSC+tracer

~100-200 nm

~50 nm
~50 nm
~50 nm
~50 nm

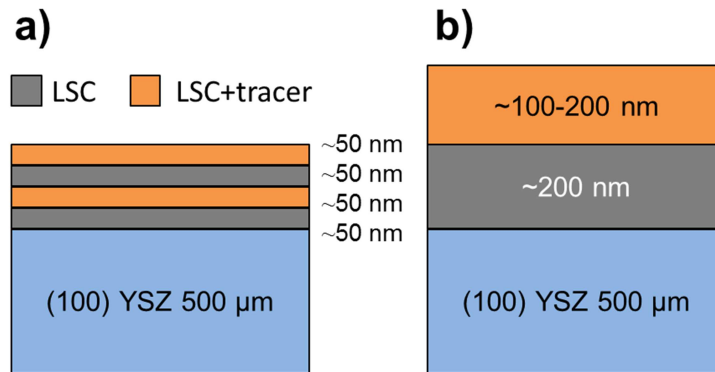~200 nm

(100) YSZ 500 μm   (100) YSZ 500 μm

Figure 15: Sketch of the sample geometries used: a) multilayers to verify spatially homogeneous diffusion, b) bilayers to determine the tracer diffusion coefficients.

After deposition, $10 \times 10 \times 0.5$ mm^3 samples were scratched with a diamond on the substrate-side and fractured into 3-4 pieces of $\sim 3 \times 10 \times 0.5$ mm^3. One of these samples was kept as a reference and the others were annealed for a certain temperature (625-800°C) and time (10-250 h) in air in a chamber furnace to generate cation diffusion profiles in the LSC multilayers.

3.1.2 Sample characterization

Phase purity of PLD targets was investigated by XRD in Bragg-Brentano geometry (X'Pert PRO diffractometer PW 3050/60, PANalytical). Thin films were investigated by optical microscopy and scanning electron microscopy (SEM) to ensure that the samples had a smooth surface with no cracks. The thin film thickness was determined from SIMS measurements using the sputter coefficient of LSC to convert sputter times and currents into depths. These film thickness measurements were referenced by digital holography microscopy (DHM, Lyncée Tec, Switzerland) of SIMS craters and SEM cross-section images of fractured substrates with thin films. The microstructure across 200 nm LSC thin films was analyzed by transmission electron microscopy (TEM) imaging and diffraction (FEI TECNAI F20)

3.1.3 SIMS depth profiling

Diffusion profiles were analyzed by ToF-SIMS measurements, performed on a TOF.SIMS 5 (ION-TOF, Germany) instrument. 25 kV Bi_5^+ clusters were used in high current bunched mode, allowing optimal mass resolution. Areas of 100×100 μm² were investigated using a raster of 512×512 measured points. Positive secondary ions and clusters were analyzed up to mass 317 and secondary ion intensities of all relevant isotopes and clusters were analyzed simultaneously. For depth-profiling, 2 kV O_2^+ ions (500×500 μm², ca. 600 nA) were used for sequential ablation of the surface between measuring mass spectra - resulting in average depth steps of ca. 1.5 nm. A low energy electron flood gun (20 V) was employed for charge compensation.

3.2 Results and discussion

3.2.1 Sample characterization

Very similar diffraction patterns indicating pseudo-cubic perovskite phase were observed for all target materials (LSC, L⁸⁶SC, LSC-T10), and are exemplarily shown in Fig. 16 for LSC and the Fe and Sm co-doped LSC-T10.
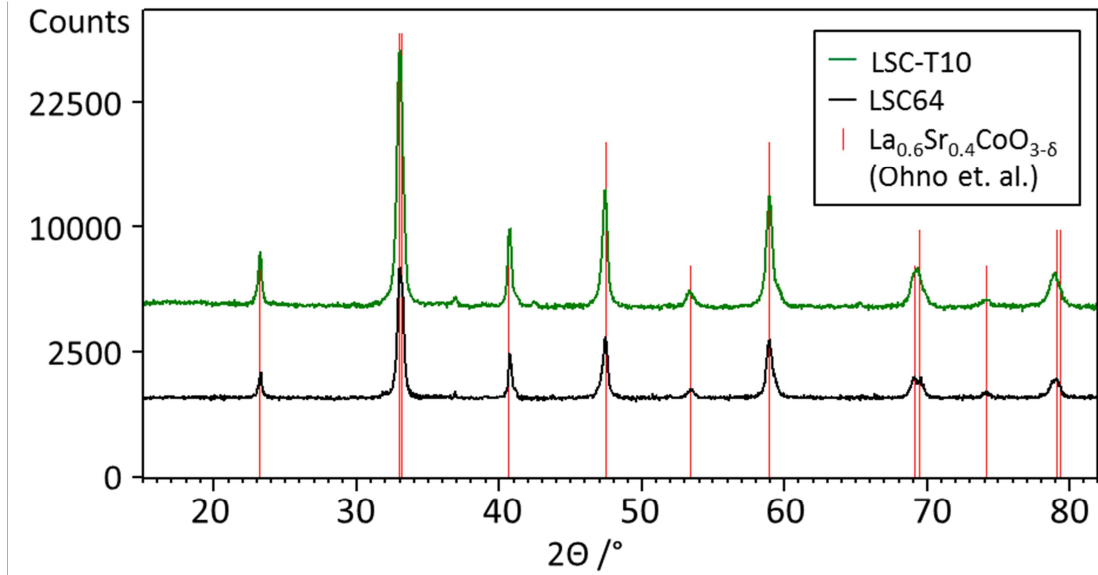
Figure 16: XRD diffraction patterns of the PLD targets LSC-T10 and LSC (baselines shifted for clarity) and stick pattern of rhombohedral La$_{0.6}$Sr$_{0.4}$CoO$_{3-\delta}$ from Ref. [80].

No significant differences in terms of lattice parameters or relative peak intensities were found between pure and tracer containing LSC, therefore we expect negligible lattice strain between LSC|LSC + tracer thin films and undisturbed growth at the corresponding interfaces. Minor impurities at $2\Theta \approx 37°$ and $42°$ could be attributed to Co-oxides, Co$_3$O$_4$ or CoO, as a consequence of the slightly deviating stoichiometry of the powders (Sec. 3.1.1). The stick pattern of rhombohedral R-3m La$_{0.6}$Sr$_{0.4}$CoO$_{3-\delta}$[80] PDF 00-36-1393 (ICDD, 2010[81]) is shown for comparison and corresponds well to the measured diffraction patterns.

The microstructure of 200 nm PLD thin films prepared from the LSC target was investigated by TEM imaging and diffraction. Cross section images of LSC-LT and LSC-HT are shown in Fig. 17. Dense thin films with columnar growth are observed for both deposition temperatures with different column diameters of about 30-35 nm for LSC-LT and 50-70 nm for LSC-HT. In both cases, close to the interface, a zone of about 10 nm with a different structure is observed, consisting of very small grains with diameters of only a few nanometers. TEM diffraction patterns showed that many of these grains adjoining to YSZ grow oriented, but with non-homogeneous orientation. Due to the

large lattice misfit between YSZ and LSC, uniform epitaxial growth is not realized. The observed microstructures with columnar and textured LSC grains for the bigger part of the film are in good agreement with microstructures of $La_{0.58}Sr_{0.4}Co_{0.2}Fe_{0.8}O_{3-\delta}$ PLD thin films reported in literature[82] for similar deposition parameters.
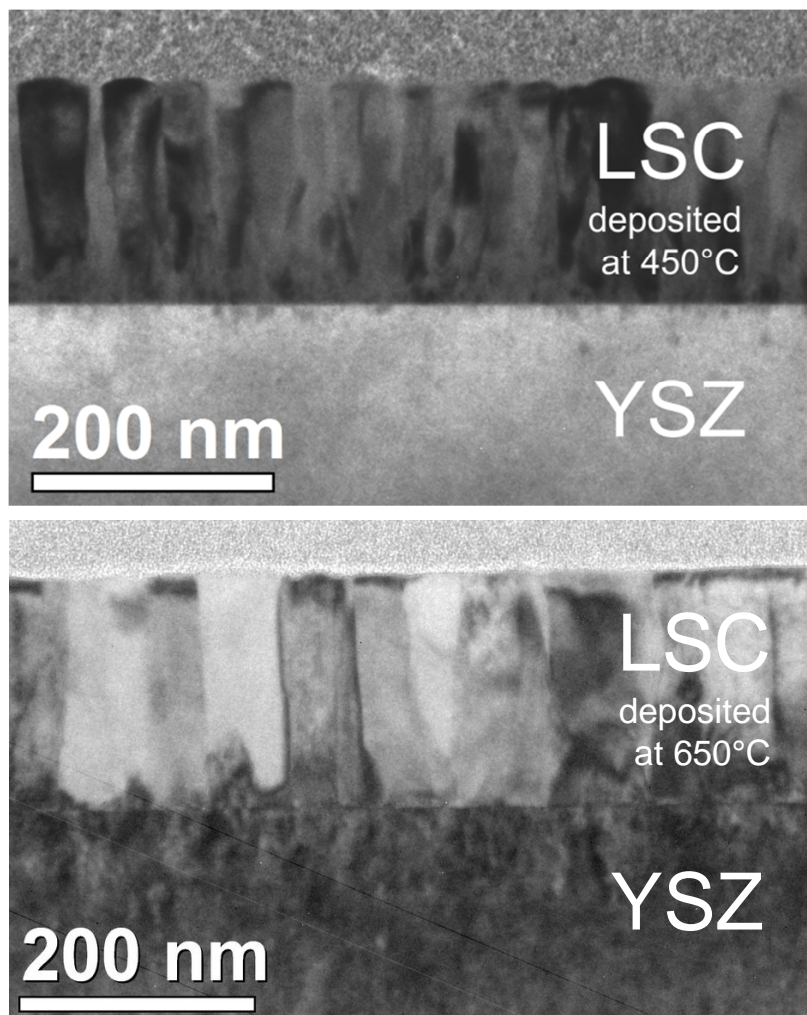
Figure 17: TEM cross section overview images of 200 nm LSC thin films deposited at different temperatures (LT, top, HT bottoms); both show columnar structures for the greater part of the film and only a small region of ~10 nm with smaller grains close to the YSZ substrate.

3.2.2 Diffusion profiles measured by ToF-SIMS

Poisson corrected secondary ion counts of $^{56}Fe^+$, $^{59}Co^+$, $^{84}Sr^+$, $^{86}Sr^+$, $^{87}Sr^+$, $^{88}Sr^+$, $^{139}La^+$, and $^{152}Sm^+$ were used to calculate the normalized tracer levels denoted as: c_{Fe}, c_{Sr}, c_{Sm}. In case of Sr, the value of the isotope fraction of $c(^{86}Sr)$ is calculated following Eq. 3 and normalized with the values measured in thin films prepared by the three different targets c_{LSC}, $c_{LSC+tracer}$ according to Eq. 4.

$$c(^{86}Sr) = \frac{counts(^{86}Sr^+)}{counts(^{84}Sr^+) + counts(^{86}Sr^+) + counts(^{87}Sr^+) + counts(^{88}Sr^+)} \quad (3)$$

$$c_{Sr} = \frac{c(^{86}Sr) - c_{LSC}}{c_{L^{86}SC \ or \ LSC-T10} - c_{LSC}} \quad (4)$$

The ^{86}Sr isotope fraction values were averaged from several measurements for the three different layers and determined as: $c_{LSC} = 0.0983$; $c_{L86SC} = 0.9653$; $c_{LSC-T10} = 0.1996$. By the normalization, the average value of c_{Sr} becomes 1 in a virgin tracer containing layer and 0 in a virgin layer without tracer.

The values c_{Fe} and c_{Sm} are normalized values of the atomic distribution of Co/Fe and La/Sm, respectively, with the same initial average values of 1 and 0 in the different virgin layers. However, a slightly different correction is necessary for the two cases to account for the different secondary ion yields in ToF-SIMS for different elements. Additionally, it is necessary to consider that for the determination of c_{Fe} and c_{Sm} only majority isotopes, and not all isotopes as in case of Sr, were analyzed. The normalization was performed by using correction factors ($corr_{Co}$ and $corr_{La}$) to account for the differences in atomic composition and the measured secondary ion signals.

$$c_{Fe} = \frac{counts(^{56}Fe^+)}{counts(^{56}Fe^+) + counts(^{59}Co^+) \cdot corr_{Co}} \cdot \frac{1}{0.1} \quad (5)$$

$$c_{Sm} = \frac{counts(^{152}Sm^+)}{counts(^{152}Sm^+) + counts(^{139}La^+) \cdot corr_{La}} \cdot \frac{1}{0.1} \quad (6)$$

The correction factors were determined to be $corr_{Co} = 1.491$ and $corr_{La} = 0.724$ for the known stoichiometry (and atomic ratios) of a LSC-T10 layer and the averaged ratio of the secondary ion counts $^{59}Co^{+}/^{56}Fe^{+}$ and $^{139}La^{+}/^{152}Sm^{+}$ measured in virgin LSC-T10 layers. The factor $1/0.1$ reflects the tracer content of 10% and is used to normalize the value from 0.1 to 1 in LSC-T10 layers.

These corrections are possible, because SIMS matrix effects affecting the secondary ion yields should not play a role in the chemically very similar layers LSC and LSC-T10. Therefore all count rates can be expected to be linear which is necessary for the corrections to be valid. The normalization step is possible as only relative values are necessary to determine diffusion coefficients, and was performed to allow the same fitting procedure for all cations. It has to be noted, that only in case of Sr, true tracer interdiffusion is analyzed, while for the other cations interdiffusion of Fe and Co, as well as Sm and La is studied. As no indication of significant differences of the diffusion coefficients in the different layers of diffusion couples were observed, the interdiffusion coefficients of Fe(Co) and Co(Co,Fe), were described by only one diffusion coefficient, and the same was done for the interdiffusion coefficients of Sm(La) and La(La,Sm).

In Fig. 18 typical diffusion profiles before and after annealing are shown. Fig. 18a shows c_{Sr} in alternating 4-layers of LSC and $L^{86}SC$ as sketched in Fig. 15a after different annealing steps. In Fig. 18b, the value of c_{Fe} in a LSC|LSC-T10 bilayer as sketched in Fig. 15b is plotted before and after annealing. All profiles showed very sharp concentration steps after deposition (before annealing). The smoothening of this step due to annealing indicates that cation diffusion has occurred. The symmetry of the profiles in Fig. 18a indicates constant diffusion coefficients through the entire depth of the 200 nm LSC films. Microstructure or strain related variations of diffusion properties were thus largely negligible, which simplifies the quantitative analysis. Only very close to the YSZ interface ($\sim$10 nm) more pronounced diffusion was observed for similar samples with smaller layer thickness. This could be attributed to the higher grain boundary density in this area (see TEM results). However, the effects of this short zone at the YSZ interface on diffusion profiles in the main part of the 200 nm thick layers were negligible.
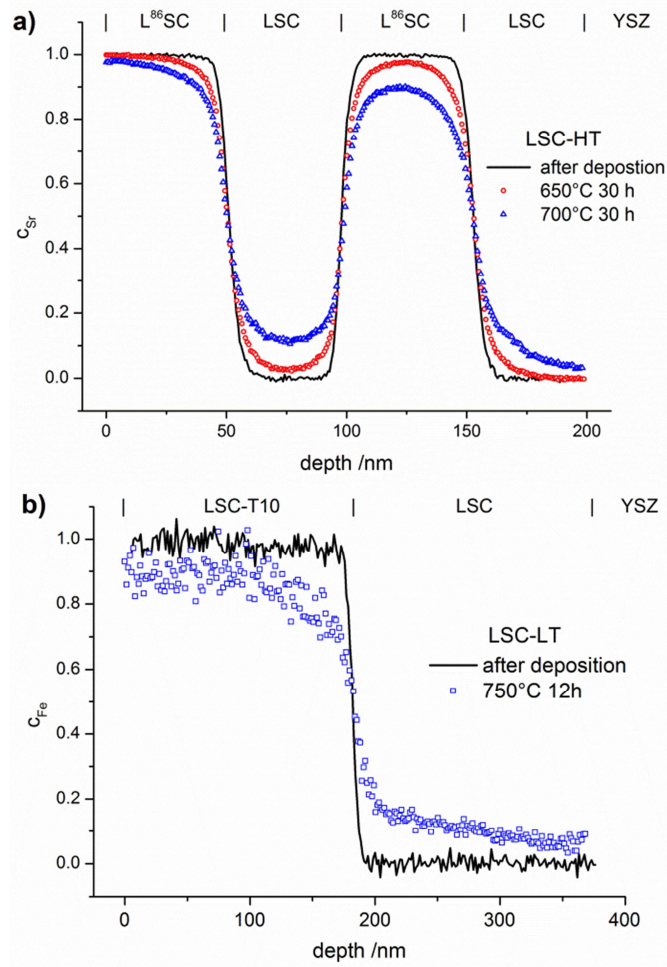
Figure 18: Typical diffusion profiles of: (a) multilayered L^{86}SC|LSC, and (b) bilayered LSC|LSC-T10 thin film. The normalized values c_{Sr} (a) and c_{Fe} (b) are shown.

3.2.3 Fitting procedure

The equation for analyzing depth profiles in order to determine the diffusion coefficient D* is given by Fick's second law:

$$\frac{\partial c}{\partial t} = \Delta(D\Delta c).$$

(7)

For two finite layers of the initial constant concentrations $c_1 = 0$ and $c_2 = c_0$ and one-dimensional bulk diffusion (x direction) the solution of Eq. (7) leads to concentration depth profiles according to[83]:

$$c = \frac{1}{2} c_0 \sum_{n=-\infty}^{\infty} \left\langle erf \frac{h + 2nl - x}{2\sqrt{(Dt)}} + erf \frac{h - 2nl + x}{2\sqrt{(Dt)}} \right\rangle. \tag{8}$$

In this formula, h denotes the thickness of the tracer containing layer, l the film thickness, and t the time. The infinite sum is necessary to convert the analytical solution for semi-infinite media to a finite film, and several approaches for a solution are possible[83].

However, concentration profiles governed by this equation fail to reproduce the measured diffusion profiles. The most probable reason for this is existence of different cation diffusion coefficients in grains and along grain boundaries. For analyzing grain and grain boundary diffusion in polycrystalline materials, a method introduced by Whipple[84] and Le Claire[85] is often used. There, a plot of the concentration vs. $x^{6/5}$ can yield the grain boundary diffusion coefficient. This method, however, is only valid for semi-infinite media, while in our case of thin films only numeric methods could be employed for fitting the tracer depth profiles.

COMSOL Multiphysics 4.0a finite elements software was used to simulate cation diffusion in a 3D model resembling the sample geometry with columnar grains. A modified brick-layer model shown in Fig. 19 was established. The "unit cell" of the geometry (Fig. 19), which consists of ¼ grain with two half grain-boundaries on two adjacent sides, was considered in the simulations. The thickness of half a grain boundary was set to 1 nm, as a typical grain boundary thickness of ~1-2 nm can be expected from literature values for similar oxides.[86, 87] The width of the ¼ grain was chosen (16 nm for LSC-LT, 30 nm for LSC-HT) to match the grain sizes observed in TEM images of the thin films (~32 nm for LSC-LT and ~60 nm for LSC-HT). The layer thickness of the different thin films (tracer / no tracer) was modeled according to the respective layer thicknesses derived via sputter time and sputter rates and currents from SIMS measurements of virgin bi- or multilayered samples. No grain boundary is expected or modeled at the LSC|LSC + tracer interface.
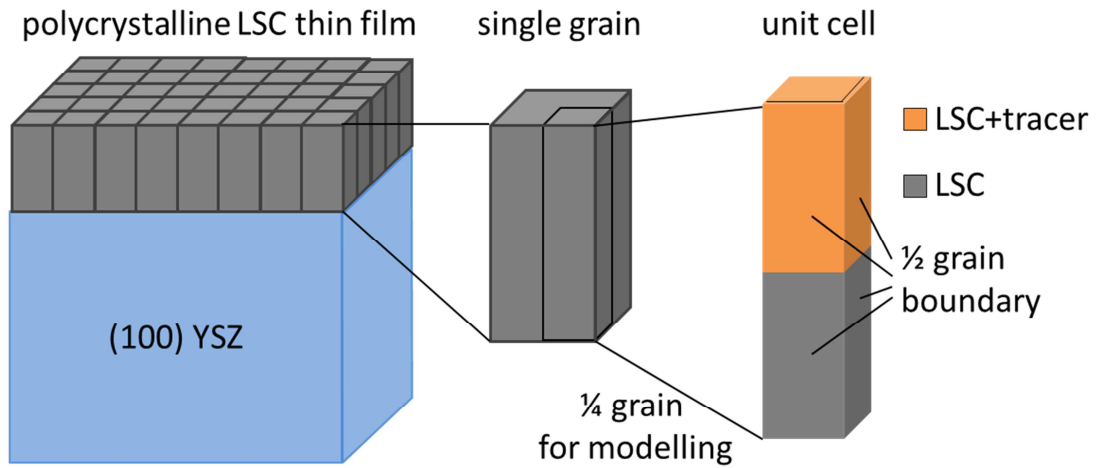
Figure 19: Modified brick-layer model used to model the columnar microstructure of LSC thin films. ¼ grain of the thin film was used as unit cell for finite elements simulation.

Fick's second law (Eq. 7) was solved with different bulk and grain boundary diffusion coefficients. Examples of calculated 3D concentration distributions and diffusion profiles obtained by this method are shown in Fig. 20. A simulation of a symmetric 200 nm|200 nm bilayer with $D_{gb} = 1 \times 10^{-15}$ cm²/s, $D_g = 1 \times 10^{-18}$ cm²/s, and a diffusion time of 100 h is shown for the two different models (different grain sizes) used for LSC-LT (Fig. 20a) and LSC-HT (Fig. 20b). Faster tracer exchange along the fast grain boundaries and exchange of tracer from the grain boundary into the grains (governed by the smaller grain diffusion coefficient) is visible. Depth profiles were calculated by integration in x-y planes and results are shown in Fig. 20c. The different effective diffusion lengths of the two models are only a consequence of the different grain size and grain boundary density.
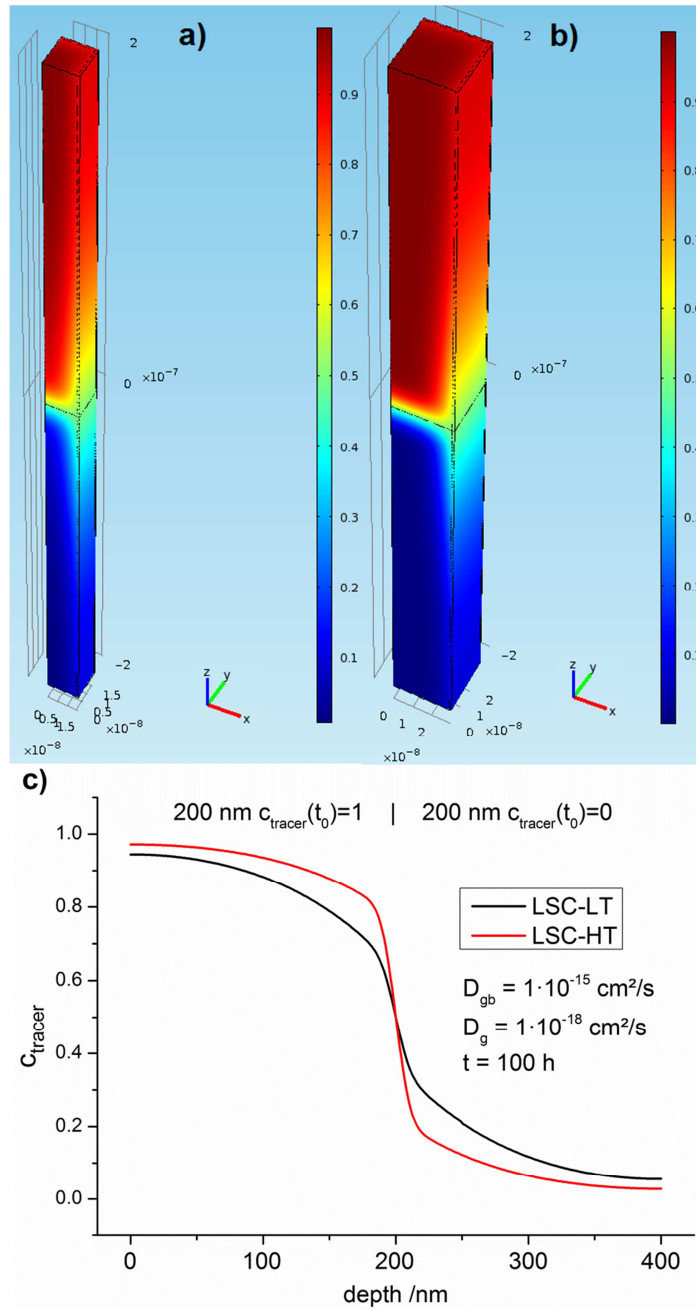
Figure 20: Finite elements simulation of a ¼ grain with two half grain boundaries as unit cell of the model shown in Fig. 19. Concentration for the two different grain sizes of LSC-LT (a) and LSC-HT (b) were modeled with the same parameters. Colors indicate concentrations; the initial concentrations are 1 in the upper part and 0 in the lower part of the unit cell. The corresponding integrated depth profiles are shown in (c) and obvious differences in tracer concentration are only caused by the different grain size.

The diffusion coefficients D_{gb} and D_g were varied manually until the calculated profiles fit the depth profiles recorded by ToF-SIMS. The latter ones were obtained by in-plane integration of the signals in the entire $100 \times 100\ \mu m^2$ area under investigation. Fig. 21 shows typical cation diffusion depth profiles of an LSC bilayer (LSC-T10|LSC|YSZ-substrate) after 12 h at 720°C. The normalized values of c_{Fe}, c_{Sr} and c_{Sm} which were extracted from the measurements are shown together with the fitting curve from finite elements simulation. The model including grain and grain boundary diffusion describes the experimental data well. Also profiles of LSC bilayers prepared at high temperatures (LSC-HT) can be described by the model. This is exemplarily shown in Fig. 21d for cation diffusion after 40 h at 760°C.
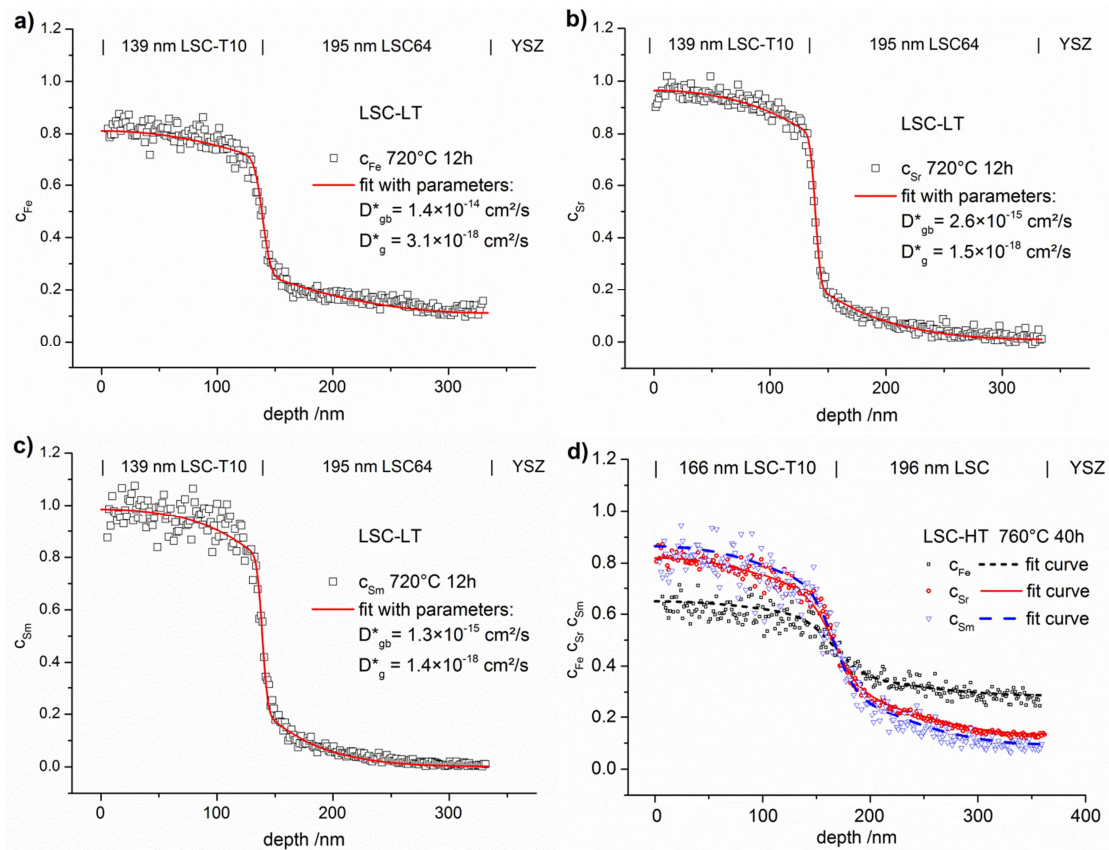
Figure 21: Diffusion profiles of all three cations showing (a) c_{Fe} (b) c_{Sr} (c) c_{Sm} in a LSC-LT bilayer after annealing for 12 h at 720°C and (d) all cations in a LSC-HT bilayer after annealing for 40 h at 760°C. Finite elements fitting curves for obtaining values of tracer diffusion coefficients for grain boundaries and grains are shown.

3.2.4 Temperature dependence and mechanism of diffusion

In this work the temperature range of 625°C-800°C was selected to investigate cation diffusion. The lower boundary is given by the extremely slow diffusion below 625°C and the consequently long annealing times (several 100 hrs) necessary for creating evaluable depth profiles. The upper boundary is caused by the reactivity of LSC with YSZ at high temperatures.[15, 16] At temperatures above 800°C and at diffusion times of several hours, the formation of a secondary phase of several nanometers thickness at the LSC|YSZ interface could be observed in ToF-SIMS depth profiles. This formation of a new phase is distorting the tracer profiles and changes the thickness of the LSC phase, thus making an evaluation of D impossible.

Fig. 22 shows the Arrhenius-type diagram of the diffusion coefficients in grain boundaries and in grains for the different cations. One has to keep in mind that the diffusion coefficients denoted Fe/Co and Sm/La describe interdiffusion of cations in a diffusion couple. For Sr, the interdiffusion of isotopes is studied and consequently indeed a tracer diffusion coefficient is measured.
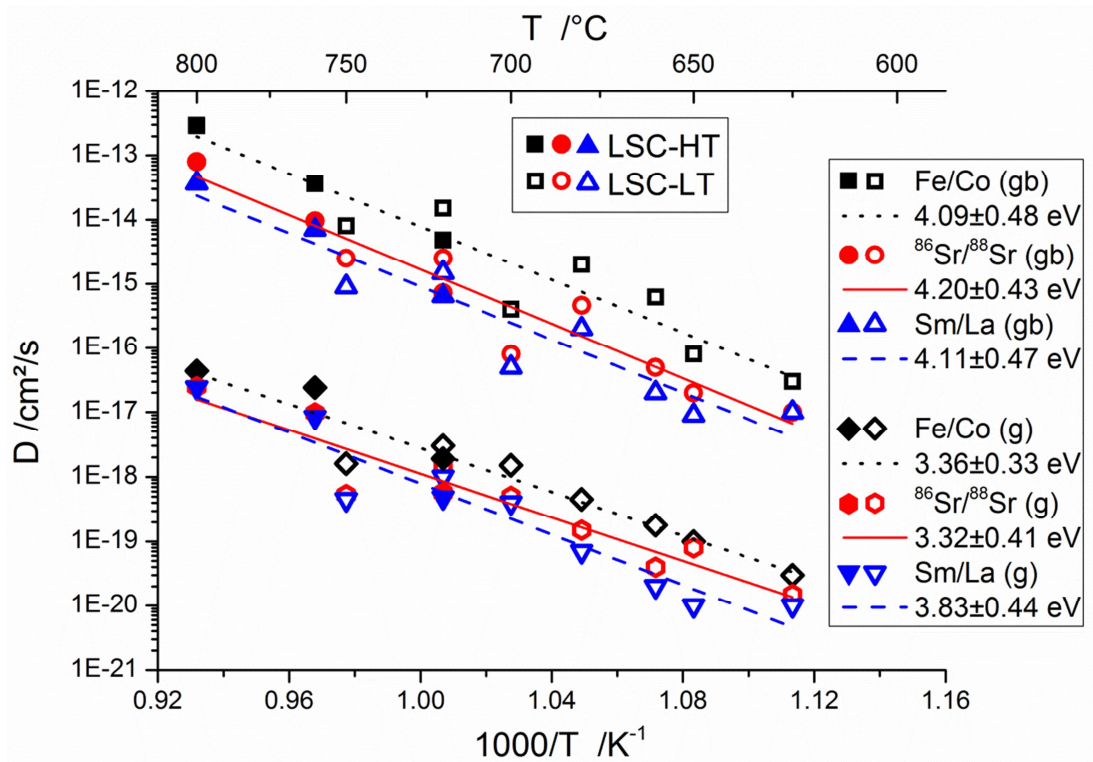
Figure 22: Arrhenius-type plot of tracer diffusion coefficients for grain boundaries and grains. About three orders of magnitude faster grain boundary diffusion and similar activation energies for all cations, ~4.1 eV for grain boundaries (gb) and ~3.5 eV for grains (g), were observed.

From these temperature dependencies of the diffusion coefficients a number of conclusions can be drawn: (i) Within the accuracy of the data, each diffusion coefficient can be described by a single activation energy. A systematic deviation of the D values of LSC-LT from those of LSC-HT bilayers was not found. Different diffusion lengths were thus most probably only a consequence of the different grain sizes (60 nm and 32 nm, respectively). (ii) Grain boundary diffusion was found to be about 3 orders of magnitude faster than diffusion in grains. (iii) All three cations showed very similar activation energies of ~4.1 eV for grain boundaries and ~3.5 eV for grains. (iv) The diffusion coefficients of all cations were found to be typically within one order of magnitude, and consequently the differences between the three cations were much smaller than the differences between the grain and grain boundary diffusion coefficients. Fe/Co showed the highest diffusion coefficients (grain and grain

boundary). This is also visible in Fig. 21. The A-site cations Sr and Sm/La showed very similar D values.

Fig. 23 displays a comparison of the data from this work with data reported in literature for bulk samples of similar MIEC perovskite-type oxides. The activation energies observed in this study are similar to many values found in literature. Also the similarity of activation energies for A- and B-site cation diffusion was repeatedly reported.[71, 74, 77, 88, 89] Concerning the absolute values of the diffusion coefficients, there seems to be large scatter in literature values, which might be partly due to the different measurement techniques employed. Another factor might be that slight deviations from the nominal stoichiometry can have an influence on the concentration of A-site and B-site vacancies and thereby on the measured impurity diffusion coefficients. Because of the exceptionally low temperatures used in this study, values of the diffusion coefficients can only be compared with values extrapolated from literature data. Very similar bulk as well as grain boundary diffusion coefficients can be extrapolated from data for $(Ba,Sr)(Co,Fe)O_{3-\delta}$,[77]. The large difference in grain and grain boundary diffusion also matches with differences found on $(La,Ca)CrO_3$,[69] or $(La,Sr)CrO_3$[90] at higher temperature.
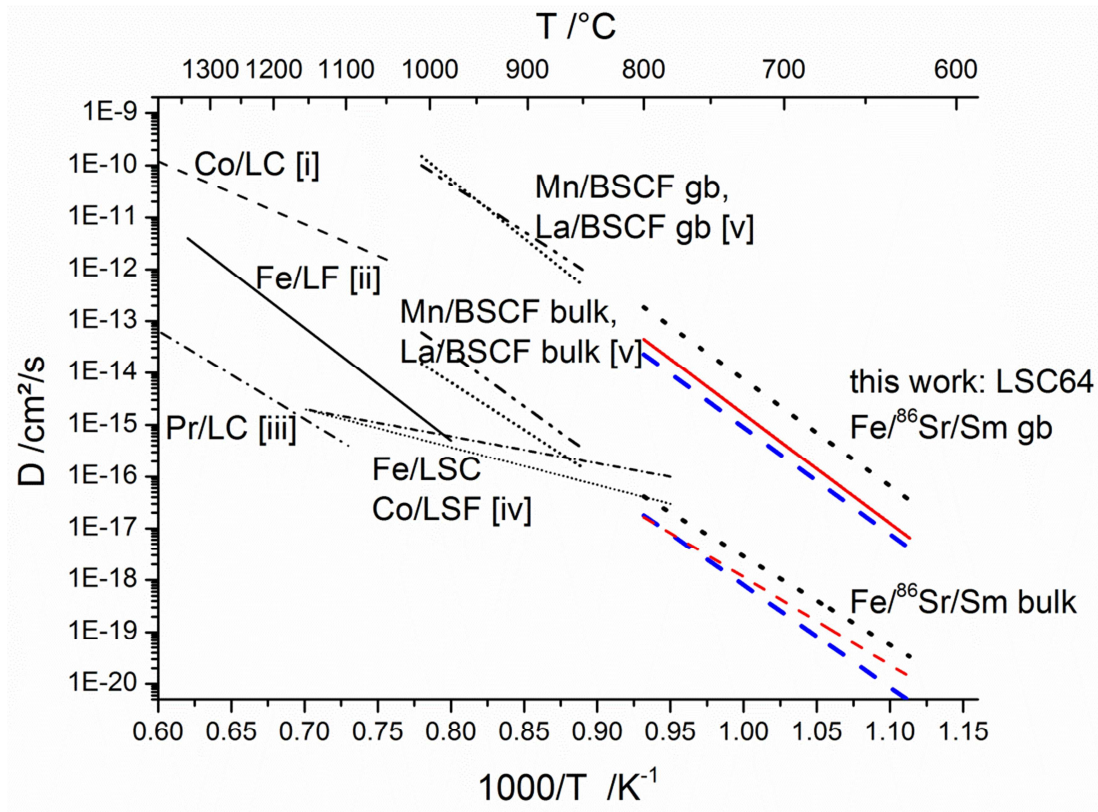
Figure 23: Comparison of diffusion coefficients with values reported in literature for similar mixed conducting perovskite-type oxides obtained by different methods; solid state reaction: [i]Co in LaCoO$_3$,[64] [ii] Fe in LaFeO$_3$;[65] impurity diffusion: [iii]Pr in LaCoO$_3$,[70] [iv]Co in La$_{0.8}$Sr$_{0.2}$FeO$_{3-\delta}$ and Fe in La$_{0.8}$Sr$_{0.2}$CoO$_{3-\delta}$[76] [v]La and Mn in Ba$_{0.5}$Sr$_{0.5}$Co$_{0.8}$Fe$_{0.2}$O$_{3-\delta}$.[77]

The fact that similar activation energies were observed for all three cations (~4.1 eV for grain boundaries and ~3.5 eV for grains) needs further discussion. Since cation defect concentrations most probably do not vary that strongly with temperature, the activation energy is expected to mainly depend on barrier heights of local ion jumps. Considering the perovskite lattice, similar heights for A- and B-site cations seem to be very surprising. The A-site which is occupied by Sr and La(Sm) is twelvefold coordinated by oxygen and much bigger than the B-site, with six-fold octahedral coordination, occupied by Co(Fe). It would consequently be extremely improbable that a cation migrating from A-site to an A-site-vacancy has to overcome about the same

activation barrier as a cation jumping from B-site to a B-site-vacancy. Nevertheless, several studies on perovskite-type oxides such as $(Ba,Sr)(Co,Fe)O_{3-\delta}$,[77] $(La,Sr)(Ga,Mg)O_{3-\delta}$,[71] $SrTiO_3$,[75, 91] and $BaTiO_3$[74, 88] observed similar activation energies for A- and B-site cations. This raises questions about the exact mechanism relevant for cation diffusion, as the simple picture of cation mobility governed by A- and B-site vacancy migration does not explain the experimental data.

Simulations in perovskite oxide systems consistently found that the formation of Schottky defects is energetically highly favorable (about 3-4.5 eV for $LaMnO_3$,[92] $LaFeO_3$,[93] and $LaGaO_3$[94]) compared with cation-Frenkel-defects (about 9 eV[92-94]). This large difference practically rules out cation mobility *via* interstitial sites. The lowest activation energies of 3.9-4.3 eV for a cation vacancy migration in simulations on $LaMnO_3$ were found for A-site vacancies (La) in (100) direction.[92] For the B-site jump the lowest activation energy is on a curved path along the (100) direction, that is activated with 7.7-9.9 eV.[92]

One possible mechanism capable of explaining the similar activation energies would be A-site cations (Sr and La/Sm) migrating via the normal (100) path to an A-site-vacancy, while B-site cations (Co, Fe) migrate by first switching to an A-site vacancy, and from there to a B-site vacancy.[77, 95] Another mechanism would involve a defect complex including both an A-site vacancy and a B-site-vacancy[71, 92, 94] that is governing the mobility of both A- and B-site cations, and is therefore leading to the same activation energy for the diffusion coefficients of all cations. Despite oxygen vacancies are far more numerous than cation vacancies in LSC, their effect on the energy barriers and pathways of cation migration, is sparsely investigated. One recent theoretical study on $SrTiO_3$ finds a reduction of the activation energy of the Sr vacancy migration by about 0.7 eV, when one or two oxygen vacancies are present in the vicinity.[96] Cation mobility in oxides with significant oxygen non-stoichiometry might therefore also be strongly affected by oxygen vacancies. A final conclusion which migration mechanism is relevant for the diffusion investigated in this work is not possible.

3.2.5 Changes in surface chemistry

Many perovskite-type oxides have a tendency towards cation segregation at the surface. For LSC and similar oxides such as $(La,Sr)(Co,Fe)O_{3-\delta}$ or $(La,Sr)MnO_{3-\delta}$, particularly a segregation of Sr to the surface is often observed[23, 25-27, 97, 98] and frequently found to inhibit the oxygen reduction reaction[25-27] as also shown in Sec. 2. The exact driving force of Sr enrichment at the surface is still under debate. Among the factors which are discussed are kinetic demixing under electrical or thermal gradients,[99, 100] or compressive stress on Sr,[101] arising from the fact that the ion radius of Sr^{2+} (144 pm, CN 12) is larger than the radius of O^{2-} (140 pm, CN 6).[102]

Here, the focus is laid on the kinetics of the Sr enrichment and a possible connection to the diffusion of cations is discussed. Irrespective of the driving force, it seems possible that the rate of Sr enrichment is limited by the transport of Sr in LSC to the surface. In order to investigate the possible connection of cation diffusion and the segregation rate, kinetic information on the growth of Sr-rich surface phases is necessary. From ToF-SIMS measurements of the surface, first qualitative information of the process is accessible. Fig. 24 shows the secondary ion intensity of Sr, relative to its bulk value, in the near surface region of 200 nm LSC-HT films on (100) YSZ for different annealing times at 600°C in air. It has to be noted, that due to SIMS-artifacts at the surface, no quantitative information on the amount or the diffusion lengths can be extracted from these measurements. Only the qualitative enrichment of Sr with time and the approximate depth of the Sr enrichment (within the first 2 nm) are extractable information.
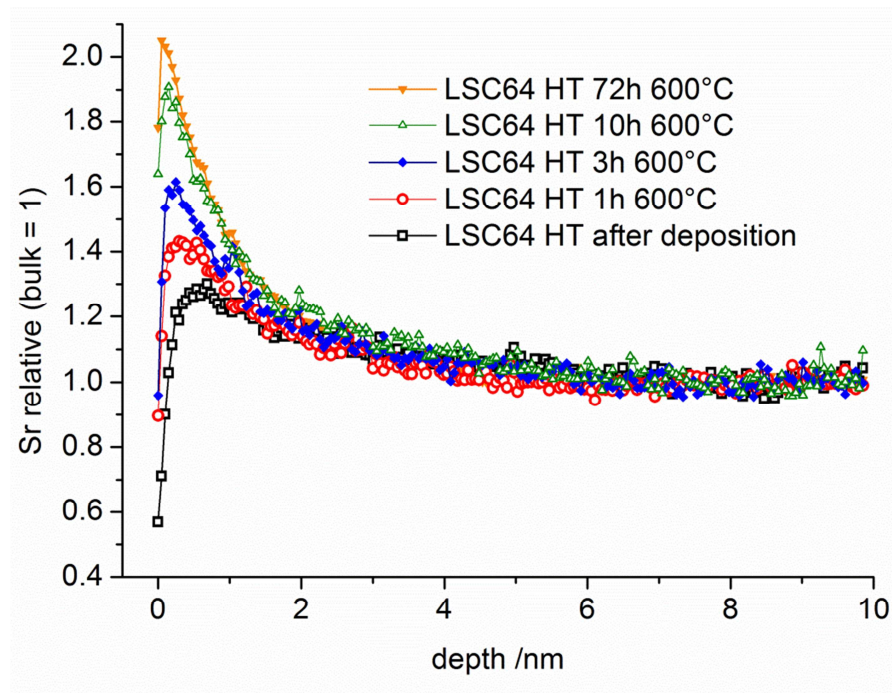
Figure 24: Sr enrichment at the surface of 200 nm LSC-HT thin films after annealing at 600°C for different times. Measurements were done by ToF-SIMS: Sr$^+$ secondary ion intensities relative to Sr$^+$ bulk values are shown.

For quantification of the surface Sr, inductively coupled plasma-optical emission spectrometry (ICP-OES) was adapted as analytical method to quantitatively analyze the Sr enrichment of similar LSC thin films, as reported in Sec. 2. 200 nm LSC-HT thin films annealed at 600°C for 72 h showed an excess of about 0.5 µg/cm^2 Sr ($\sim 3.4 \times 10^{15}$ Sr ions/cm^2) at the surface. This would be equivalent to ~ 1 nm of SrO or Sr(OH)$_2$ which are assumed to be the chemical states in which the surface Sr is present.[98] Connected with this change of composition at the surface was a one order of magnitude increase of the surface polarization resistance of LSC used as a SOFC cathode.

To compare these kinetic results with the cation diffusion parameters of this work, the measured diffusion coefficients need to be transferred into an amount of Sr that is

transported to the surface. First the diffusion lengths of Sr are calculated from the diffusion coefficients according to:

$$l_{diff} = \sqrt{Dt} \ . \tag{9}$$

In Tab. 1 the lengths l_{diff} for the Sr tracer diffusion coefficients from this study, extrapolated to 600°C, are shown. In addition, values from a finite elements simulation considering both, grain and grain-boundaries for the LSC-HT (60 nm grain size) model are given. In these simulations the amount of Sr diffusing over a phase boundary into a phase with a constant concentration level of 0 (i.e. continuous formation of a new phase) was investigated. The amount of segregated Sr was calculated from the resulting profile and transferred back to an effective diffusion length with Eq. 8 to give values comparable to the first two columns.

Table 1: Tracer diffusion lengths according to Eq. 9 for extrapolated values of the grain and grain boundary diffusion coefficients at 600°C for the diffusion times shown in Fig. 24 and for 30 000 h, as an estimate value of aspired durability of a SOFC. The last column represents effective values for combined grain and grain boundary diffusion, see text.

time /h	$D^*_g \sim 1 \times 10^{-20}$ cm²/s	$D^*_{gb} \sim 1 \times 10^{-17}$ cm²/s	Simulation (60 nm grains)
1	0.06 nm	1.9 nm	0.36 nm
3	0.10 nm	3.3 nm	0.7 nm
10	0.19 nm	6.0 nm	1.2 nm
72	0.51 nm	16.1 nm	3.0 nm
30 000	10.4 nm	329 nm	71 nm

However, several considerations need to be made prior to an interpretation of these data in terms of a possibly rate limiting diffusion. First, not diffusion lengths, but the

amount of Sr (M_{Sr}) that is transferred from LSC to the surface and from there into the new phase is of interest. Those two parameters are related as shown for a semi-infinite medium and only one diffusion coefficient.[83]

$$M_{Sr} = \frac{2}{\sqrt{\pi}} N_0 \sqrt{Dt} \qquad (10)$$

For a Sr concentration N_0 in LSC of 0.4/56.2 Å^3 (cell volume) $= 7.1 \times 10^{21}$ Sr ions/cm^3 Eq. 8 can be used to estimate the diffusion length required to segregate ~1 nm of the Sr-rich phase: A value of ~4.8 nm results.

Most importantly the segregation, i.e. the diffusion into a different phase is a chemical diffusion and not tracer diffusion. Hence the expected differences between the chemical diffusion coefficient of Sr (D_{chem}) and the tracer diffusion coefficient (D^*) need to be discussed. Formally, chemical diffusion is a diffusion of neutral components.[103] For charged particles (such as Sr^{2+}), ambipolar diffusion of at least two species is necessary. In our case the other diffusing particles could be either oxide ions (O^{2-}) or electrons. D_{chem} of neutral Sr or SrO includes diffusion coefficients and concentration of all relevant defects.[103] As both possible counter defects (oxygen vacancies, electron holes) have a much higher concentration than Sr vacancies in LSC and are many orders of magnitude faster, their influence can be neglected and only the diffusion of Sr vacancies ($V_{Sr}^{//}$) is relevant.

To a good approximation the chemical diffusion coefficient is therefore given by the Sr vacancy diffusion coefficient. The difference to the tracer diffusion coefficient of Sr is that, even if also there vacancies are necessary for diffusion, the coefficient is referred to the cations, not their vacancies. As the number of vacancies is typically very much smaller than that of ions, (cf. also the high cation vacancy formation energies of 3-4.5 eV discussed in Sec. 3.2.4) a difference of at least 2 orders of magnitude can be expected. That would cause the chemical diffusion coefficient to also be at least 2 orders of magnitude higher than the tracer diffusion coefficient. For completeness it has to be said that the tracer diffusion coefficient is even further smaller than the chemical diffusion coefficient because of different probabilities of back-diffusion and further corrections which are referred to as the Haven ratio (H). As it is typically

smaller than 1, but in the order of 1,[103] a further factor of ~1-2 higher chemical diffusion coefficient compared to the tracer diffusion coefficient can be expected.

Summarizing we can say that chemical diffusion lengths of Sr of ~5 nm in LSC are already enough for a significant electrochemical degradation of as LSC as SOFC cathode. Even though the cation defect concentration and thus the exact ratio between the chemical diffusion coefficient D_{chem} and the tracer diffusion coefficient D^* is not known in our case, D_{chem} most probably exceeds D^* by at least two orders of magnitude. Hence the tracer diffusion length that is sufficient to cause a chemical diffusion length of 5 nm is 0.5 nm or lower (Eq. 7). For combined grain and grain boundary diffusion such an effective diffusion length is achieved already after about 2 h at 600°C.

According to these considerations it is extremely difficult to control Sr segregation by limiting the diffusion of Sr. Inhibiting Sr segregation over technologically interesting durations of several 10000 hours, e.g. 30000 h as in the table, by freezing the cation lattice, and thus keeping Sr from segregating to the surface, would require very low chemical diffusion coefficients of $D_{chem} < 1.5 \times 10^{-21}$ cm^2/s corresponding to $D^* < 1.5 \times 10^{-23}$ cm^2/s. From extrapolation of the measured bulk tracer diffusion coefficients, it becomes clear that such low diffusion coefficients could only be reached at temperatures below 500°C even in the absence of fast grain boundary diffusion. Therefore, optimizing the microstructure and thus avoiding fast grain boundary diffusion is also not a promising approach. Moreover, working at the low temperatures (below 500°C) is not a successful strategy, as the polarization resistance of the oxygen reduction reaction on LSC is too high for reasonable SOFC cathode operation.

Therefore we can conclude that Sr diffusion in LSC is too fast for avoiding segregation to the surface within the limits set by its applicability as SOFC cathode. It also means that diffusion of Sr in LSC is not rate limiting for the growth of Sr-rich surface phases and we suppose the same for similar perovskite oxides. A deeper knowledge of the driving forces and of the exact mechanism of cation segregation in perovskite oxides seems to be necessary to tailor materials properties and/or microstructures for optimal performance and stability in SOFCs.

3.3 Conclusions

Cation tracer diffusion was investigated in $La_{0.6}Sr_{0.4}CoO_{3-\delta}$ thin films prepared by PLD on single crystalline (100) YSZ substrates. By using high quality bi- and multilayered diffusion couples and ToF-SIMS, cation tracer depth profiles were measured before and after thermal annealing steps in air at comparatively low temperatures of 625-800°C. The profile shapes as well as the grain size dependence of the profiles indicates that fast grain boundary diffusion strongly affects the measurements. A numerical analysis using finite element calculations allowed the extraction of cation diffusion coefficients for all cations and grains as well as grain boundaries. B-site Fe/Co interdiffusion showed the highest diffusion coefficients, followed by the A-site cations Sr and Sm/La. However, differences were surprisingly small and also similar activation energies of D were found for all cations, which strongly suggest a coupled migration mechanism for A- and B-site cations. Activation energies were slightly higher for grain boundary diffusion (~4.1 eV) than for grain diffusion (~3.5 eV) and grain boundary diffusion showed about 3 orders of magnitude larger diffusion coefficients. Moreover, the potential correlation between the diffusion of Sr and surface enrichment and segregation of Sr was investigated. Sr mobility was found to be by far high enough to explain significant surface segregation within short times even below 600°C. Diffusion of Sr in LSC is thus indirectly shown to be not rate limiting for Sr segregation to the surface. Suppression of cation segregation to the surface at SOFC operation temperatures therefore requires further knowledge and control of the driving forces governing segregation.

4 Tensile Lattice Strain Accelerates Oxygen Surface Exchange and Diffusion in La$_{1-x}$Sr$_x$CoO$_{3-\delta}$ Thin Films

This chapter contains in large part material published as scientific paper in the journal "ACS Nano".[104]

The influence of planar lattice strain on the oxygen exchange kinetics and oxygen diffusion in LSC is the topic of this chapter. In recent publications lattice strain was shown to influence many important material properties such as the electronic structure and charge transfer,[97, 105, 106] phase transitions,[107] interface cation chemistry,[108-112] surface and bulk oxygen transport,[113-115] and the concentration of oxygen vacancies at the surface.[97, 116] Also an influence on the oxygen surface exchange and transport has been indirectly shown.[24, 117] The reasons for these effects on the atomistic scale can be found in changes in interatomic bond lengths and bond strengths. Simulations on LaCoO$_3$ [115] revealed that these changes can influence the activation barriers of the curved path[118-120] of oxygen migration in perovskite oxides and can strongly enhance mobility in distinct directions and thus also chemical diffusion of oxygen in MIECs. These promising results, demonstrating that a modification of lattice strain can lead to significant kinetic improvements at the elementary process level, provided the motivation to study these effects at a collective level experimentally.

Isotope exchange depth profiling (IEDP) was chosen as the measurement technique, due to the simple underlying methodology[121] and its direct way of investigating the oxygen exchange reaction and diffusion kinetics. While in literature IEDP is often performed on bulk samples, it should be emphasized that establishing and measuring tracer concentration variations in very thin films of 20 nm is far from trivial and rarely done. For LSC this seems particularly challenging since critical lengths (L$_{crit}$ = D/k) in the μm-range up to 150 μm are reported for bulk LSC samples.[14, 122-124] Accordingly, the experimental conditions were determined for which a significant ^{18}O concentration gradient within LSC exists, and those were restricted to a very limited temperature

window and short diffusion times of mostly only about 5 minutes. Further the effect of chemically induced tracer incorporation, which could not be avoided, and its effect on the accuracy of the determined valued for k* and D* is discussed.

The lattice strain of LSC was tailored by depositing epitaxial thin films of about 20 nm thickness on different single crystalline and (100) oriented substrates $SrTiO_3$ (STO) and $LaAlO_3$ (LAO). The sample preparation and strain analysis was done by collaboration partners based on a recent work[97] investigating the influence of lattice strain on surface electronic and chemical states of $La_{0.8}Sr_{0.2}CoO_{3-\delta}$. For different strain states the temperature dependence of the collective kinetic parameters were probed (coefficients of oxygen surface exchange, k*, and oxygen tracer diffusion, D*). Our results demonstrate that tensile strain can strongly enhance oxygen exchange rates and diffusion coefficients compared to the compressive state. This enhancement was found consistent across various samples that included the effect of chemical surface modification and the LSC-composition ($La_{0.8}Sr_{0.2}CoO_{3-\delta}$, denoted LSC82 and $La_{0.6}Sr_{0.4}CoO_{3-\delta}$, denoted LSC64).

4.1 Experimental

4.1.1 Sample Preparation

LSC films with thicknesses of about 20 nm on single crystal STO, LAO, and MgO were prepared by cooperation partners by pulsed laser deposition, using a KrF excimer laser at $\lambda = 248$ nm, 10 Hz pulse rate, and 400 mJ pulse energy under $p(O_2)$ of 10 mTorr at 700°C. After deposition, the sample was cooled at 10 K/min to room temperature for ~2 hours under $p(O_2)$ of 2 Torr. The target used for LSC82 film deposition is purchased from MTI Corporation, USA. LSC64 target was prepared using the (Pecchini) nitrate/citrate route, the following materials were used: Co 99.995%, $SrCO_3$ 99.995%, La_2O_3 99.999%, HNO_3 99.999%, Citric acid monohydrate 99.9998% (all Sigma-Aldrich)

4.1.2 Structural Characterization

A Veeco/Digital Instrument Nanoscope IV was used by cooperation partners to perform tapping mode atomic force microscopy (AFM) for characterizing the surface morphology before and after chemical etching. X-ray diffraction (XRD) 2θ-ω scans and reciprocal space mapping (RSM) were performed by cooperation partners to characterize the crystal structure and strain states of the LSC films, respectively. The measurements were performed using a high resolution four-circle Bruker D8 Discover diffractometer, equipped with a Göbel mirror, 4-bounce Ge (022) channel-cut monochromator, Eulerian cradle and a scintillation counter, using Cu Kα_1 radiation.

4.1.3 ^{18}O tracer exchange

For ^{18}O tracer exchange experiments, single crystalline substrates ($10 \times \sim 3 \times 0.5$ mm^3) with LSC thin films on top were placed inside a quartz tube and heated (12 K/min) to the specified annealing temperature. Then the quartz tube was evacuated (0.02 mbar) and filled with 200 mbar tracer oxygen (97.1% ^{18}O isotope enriched, Campro Scientific, Germany). The evacuation process was performed in about 5 minutes and the tracer filling took 10 seconds. After annealing for a certain time (4-36 min), the sample holder was removed from the tube furnace and the quartz tube was cooled (ca. 60 K/min) while retaining the gas pressure at 200 mbar ^{18}O$_2$. At 80°C the tube was opened and the sample was removed and quenched to room temperature in ambient air.

4.1.4 SIMS depth profiling

ToF-SIMS measurements were performed on a TOF.SIMS 5 instrument. 25 kV Bi$^+$ primary ions were used in a novel operation mode optimized for oxygen tracer experiments described in the following chapter, thus allowing < 100 nm beam

diameter and an exact determination of the oxygen isotope fraction (measured natural abundance ^{18}O value 0.206% ± 0.004). Areas of 100×100 μm^2 were investigated using a raster of 512×512 or 1024×1024 measured points. Negative secondary ions were analyzed. For depth-profiling, 2 kV Cs$^+$ ions (500×500 μm^2, ca. 105 nA) were employed for sequential ablation of the surface between measuring mass spectra - resulting in average depth steps of ca. 0.2 nm. This distance was chosen as the smallest meaningful step size for sputtering - 0.2 nm is about the distance of adjacent oxide-ion layers in (100) direction of LSC. For charge compensation, a low energy electron flood gun (10 V) was used.

4.2 Results and discussion

4.2.1 Structure and strain state of the LSC thin films

The perovskite LSC82 has a rhombohedral unit cell with a pseudocubic lattice constant of $a_{pc} = b_{pc} = c_{pc} = 3.851$ Å. Two different single-crystal substrates STO (100) (a = 3.905 Å) and LAO (100) (a = 3.793 Å) were used to produce a tensile and compressive planar strain within the pseudocubic LSC82, respectively. At room temperature, based on the lattice mismatch between the film and the substrates, STO introduces 1.4% tensile and LAO introduces -1.5% compressive planar strain into the LSC82 films. At the experimental temperatures up to 475°C, the expected tensile strains induced by STO decrease to 1.0%, while the compressive stains induced by LAO increase to -1.9% due to the different thermal expansion coefficients of the film and substrates. Normal XRD scans (Figs. 25a, 25b) of the as-deposited LSC films grown on both substrates, hereafter denoted as LSC/LAO and LSC/STO, clearly showed only (00l) diffraction peaks, which indicates single phase (001) LSC//(001) STO and (001) LSC//(001) LAO. XRD reciprocal space maps measured at room temperature around the (103) Bragg reflection of the pseudocubic LSC thin films (Figs. 25c, 25d) confirm that the LSC film is fully strained by the STO and LAO substrates respectively since the in-plane components of the reciprocal lattice vectors for both the film and the substrate

are matching well. While some strain relaxation away from the interface can be expected, the sharp film peaks aligning with substrates peaks in reciprocal space maps indicate that the films are mostly uniformly strained without significant relaxations in them. This is reasonable because the films are very thin, ~20 nm, and can sustain a high quality of epitaxy with the substrate. In addition, it can be expected that these films retained their strain states at the elevated temperatures in the experiments reported here, as was demonstrated in a previous work using the same type of strained LSC films with *in situ* XRD up to 500°C.[97]
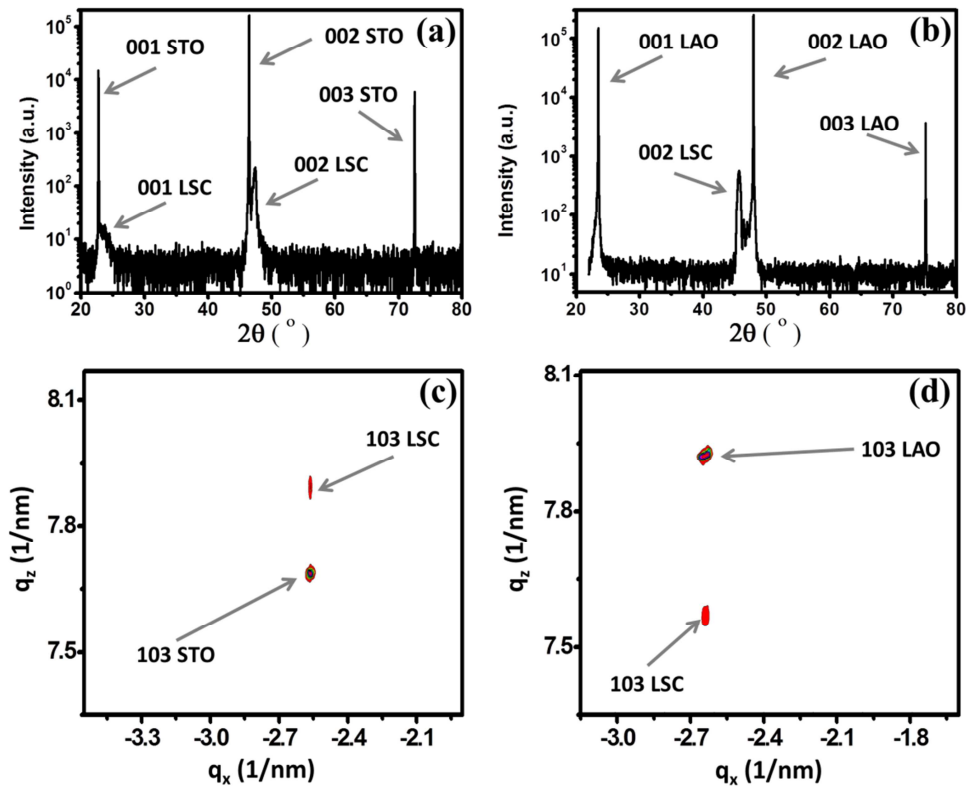
Figure 25: The 2θ-ω scans in logarithmic intensity scale of (a) LSC/STO (b) LSM/LAO show only (00l) diffraction peaks of LSC. X-ray diffraction reciprocal space maps for (c) LSC/STO and (d) LSC/LAO thin films. The arrows in (c) and (d) show the (103) reflections of the LSC thin films and the substrates.

The LSC films grown on STO and LAO exhibited a smooth surface (Figs. 26a, 26b) with an overall root mean square roughness (RMS) of 0.64 ± 0.06 nm and 0.56 ± 0.05 nm respectively. The color-contrast shown in the AFM images for both films corresponds to a peak-to-valley height difference of only 1-2 nm. The surfaces of these two sets of films is similar to each other, enabling a comparison of oxygen exchange kinetics between them that may have only minimal (if any) artifacts due to the surface morphology differences.
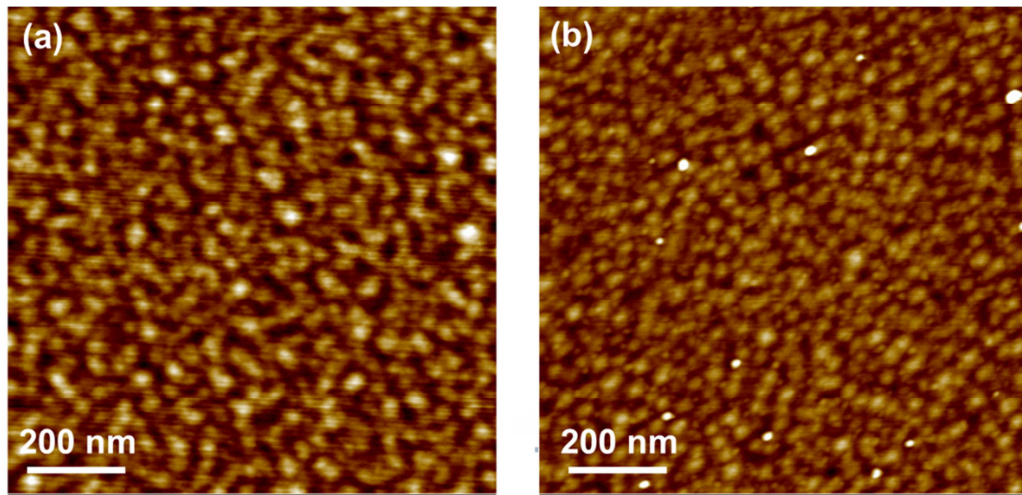
Figure 26: LSC morphology on (a) STO and (b) LAO showed smooth surfaces with RMS roughnesses of 0.64 ± 0.06 nm and 0.56 ± 0.05 nm, respectively, imaged by atomic force microscopy.

4.2.2 SIMS depth profiles

Poisson corrected secondary ion counts of $^{16}O^-$ and $^{18}O^-$ were used to calculate the ^{18}O tracer fraction c:

$$c = \frac{counts(^{18}O)}{counts(^{16}O) + counts(^{18}O)} . \tag{11}$$

[17]O⁻ (natural abundance 0.038%) was ignored due to interference with the stronger
[16]OH⁻ secondary ion signal. The tracer fraction c was then normalized according to:

$$c' = \frac{c - 0.00205}{0.971 - 0.00205}.$$

(12)

By this normalization step the experimental boundaries of tracer fraction, given by the natural abundance of ^{18}O (0.205%) and its isotope fraction in the annealing gas (97.1%), are taken into account. Thin film thicknesses were calculated from SIMS measurements by using the Cs^{+} ion current and sputter time, assuming the same sputter coefficient for all LSC films. The sputter coefficient was determined in a previous work from multiple LSC films sputtered in SIMS, with their thicknesses being measured by cross-section-SEM and digital holography microscopy (DHM Lyncee Tec, Switzerland). The same normalization was used to transfer sputter times into depths. For location of the LSC|substrate interface, the secondary ion signals of CoO^{-}, AlO^{-} and TiO^{-}, respectively, were used. The sharpness of the interface in SIMS measurements was characterized by the drop of the CoO^{-} counts from 90% to 10% of the CoO^{-} counts measured in the center of the LSC-film, yielding typical values of 2-3 nm (a very low value for SIMS depth profiling[125-127]). Profiles of CoO^{-} are shown for different annealing temperatures in Supplementary Information. At the interface, several effects such as ionic mixing during sputtering, surface roughness and sputter-induced roughness add up to spread the almost atomically sharp interface. The center of this "interface zone" was treated as "the interface" and used for film thickness calculation. Thickness calculations from SIMS depth profiles were in good agreement with XRR measurements of the films. Typical depth profiles are shown in Fig. 27 for LSC82 thin films on STO and LAO. The main features of all profiles are a surface value in tracer fraction of a few percent up to 30% - below the ^{18}O fraction of 97.1% in the annealing gas, a pronounced decrease of the tracer fraction throughout the LSC film and a final sharp decrease close to the film/substrate interface. Details of the profile such as the sharp drop in the very first nanometer as well as the temperature/time settings and the influence on the error margins of k* and D* will be discussed later.
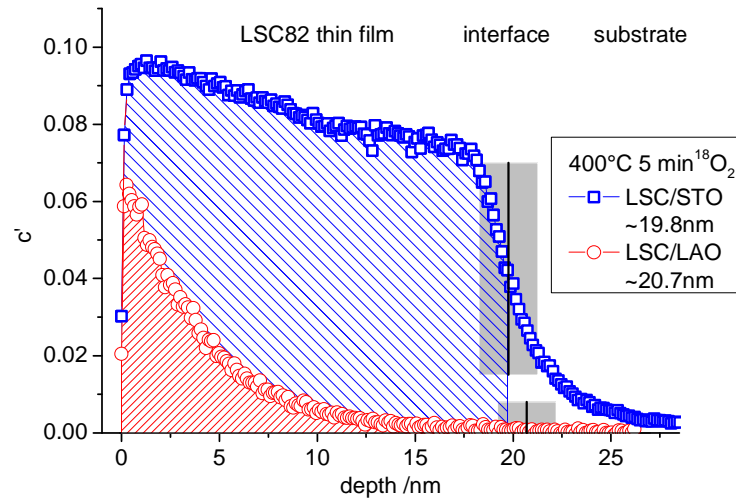
Figure 27: Tracer depth profiles of 20 nm epitaxial (100) LSC82 films with tensile strain on STO and compressive strain on LAO. Profiles resulted from oxygen tracer exchange for 5 min at 400°C. Obvious differences in amount of tracer incorporated as well as in slope are pointing to strong differences in oxygen exchange kinetics in connection with the strain state.

In Fig. 27 it is also exemplarily shown that the resulting tracer depth profiles in LSC82 thin films strongly depend on the substrate and thus on the strain states of the films. It is apparent that the total amount of tracer exchanged is much higher for the tensile strained LSC/STO system, indicating a significantly higher surface exchange coefficient there. Besides that, also the gradient of the two tracer profiles is very different. While LSC/LAO drops to half the near-surface level within about 3 nm, the slope of the ^{18}O-fraction in LSC/STO is much smaller. This points to LSC/STO having also the higher diffusion coefficient.

4.2.3 Determination of k* and D*

Depth profiles of the normalized tracer fraction c' were used to calculate the tracer surface exchange coefficient k* and the tracer diffusion coefficient D*. Assuming the substrates to be ideally blocking for oxide ions, the LSC thin film can be considered as

a thin sheet with tracer incorporation from a source of constant tracer concentration on one side (the surface). For symmetry reasons, the profiles resulting from this geometry are exactly one half of a profile generated in a plane sheet of twice the thickness and tracer incorporation on both sides. The corresponding solution of Fick's second law,

$$\frac{\partial c}{\partial t} = D^* \frac{\partial^2 c}{\partial x^2}$$
(13)

for a change from c_1 to c_2 can therefore be applied for our films and the transient of tracer fraction with depth and time is given by[83]

$$c' = \frac{c(x,t) - c_1}{c_2 - c_1} = 1 - \sum_{n=1}^{\infty} \frac{2L \cos(\beta_n x / d) \exp(-\beta_n^2 D^* t / d^2)}{(\beta_n^2 + L^2 + L) \cos(\beta_n)} .$$
(14)

In this equation, d denotes the film thickness, t the time and L is the quotient of film thickness and critical length that is derived from d, k* and D*:

$$L = \frac{dk^*}{D^*} .$$
(15)

The β_n factors are solutions of the equation:

$$\beta_n \tan \beta_n = \frac{dk^*}{D^*} = L$$
(16)

and can only be numerically analyzed for each L. A procedure for determining β_n is given in Ref.[128]. In our analysis a recursive fitting of Eqs. (14) and (16) was performed to the experimental data and thus of L, k* and D* using 12 roots β_n (n = 1-12).

Because of non-idealities of real samples and measurement related limitations, the real depth profiles differ from calculated profiles especially at the surface and at the interface. In all measurements, in the first 1-1.5 nm, close to the thin film surface, a lower ^{18}O fraction than expected from the main part of the depth profile was found

(cf. Fig. 27). This might be caused by ^{18}O tracer back-diffusion, while keeping the samples in ambient air ($< 80°C$). However, tracer exchange and diffusion at temperatures below $80°C$ (between annealing and SIMS analysis) are considered to be negligible – reference samples were measured immediately after and 6 months after annealing and almost no differences in their tracer depth profiles were found. Only the very first data points < 1 nm showed a minimally lower ^{18}O fraction after 6 months at room temperature. Hence, it is more likely that this effect occurs due to ^{16}O-rich adsorbates from ambient air ($-O_2$, $-OH$) at the surface.

A sharp drop of the ^{18}O fraction takes place within the interfacial zone already observed for the CoO^- signal (cf. Fig. 27) ^{18}O fractions in this zone are a mixture of the values in the thin film and in the substrate. Owing to these non-idealities, on both sides of the depth profiles in LSC - at the surface and towards the interface - 1.5 nm were ignored for fitting but included for length calculation. Any significant effect of interfacial cation diffusion on the determined k^* and D^* values can thereby be neglected. This interface zone of 3 nm should not be confused with the depth resolution of the ^{18}O fraction, which is significantly higher. Fig. 28 illustrates this fitting procedure, showing the measured depth profile (squares), the actual fit within the set boundaries (solid line) and the idealized tracer depth profile (dotted line) for k^*, D^* and thin film thickness d (d is evaluated from the CoO^- signal, evaluation is not shown here). Applying this procedure to the two profiles in Fig. 27 yields $k^* = 9.67 \times 10^{-11}$ cm/s, $D^* = 8.0 \times 10^{-16}$ cm^2/s for LSC/LAO and $k^* = 5.83 \times 10^{-10}$ cm/s, $D^* = 1.9 \times 10^{-14}$ cm^2/s for LSC/STO and thus a much faster oxygen exchange and diffusion in the tensile LSC film at $400°C$.
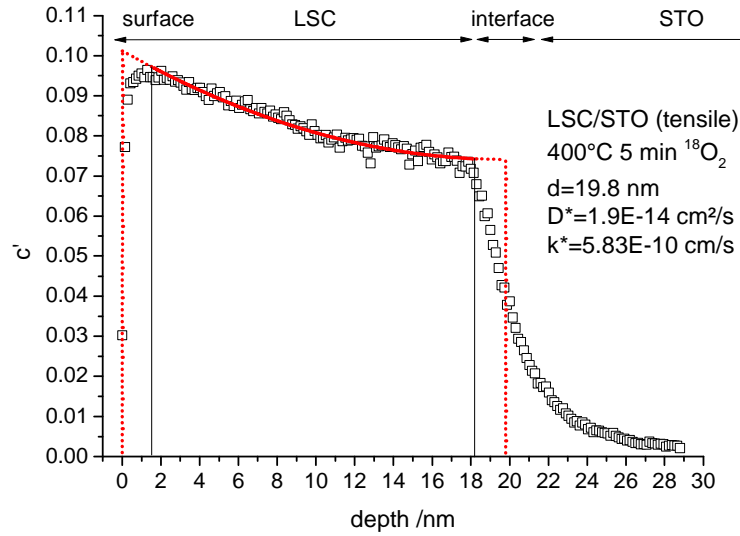
Figure 28: Tracer depth profile of tensile strained LSC82/STO after annealing in $^{18}O_2$ for 5 min at 400°C illustrating the fitting method. The solid line denotes the actual fit, the dotted line shows the idealized profile for the film thickness d and fitting parameters D* and k*.

For a completely blocking substrate the normalized tracer fraction is expected to be constant in LSC close to the interface and to be zero beyond the interface throughout the substrate (compare dotted line Fig. 28). To represent an ideally blocking substrate, the undoped substrates (LAO, STO, MgO) were used. Although these oxides can show significant oxygen diffusion at temperature above 600°C[129, 130] for given experimental conditions (below 500°C, few minutes), tracer profiles extended only very slightly into the substrate. The effect is measureable for all substrates and is more pronounced for samples with higher tracer levels in LSC. Ionic mixing from SIMS doubtlessly also contributes to tracer being carried over into the substrates. However, some residual tracer diffusion in the single crystalline substrates seems to be present, which is most probably caused by impurities. Significant tracer incorporation into the substrate would lead to falsely too low values of k* and D* when analyzing by means of Eqs. (14) and (16). For all investigated profiles relevant in this work, however, the ^{18}O level in the substrate is very low with the total ^{18}O-amount being always less than 3% of that in LSC even at the highest temperatures. Therefore, an analysis using Eqs. (14) and (16) is assumed to lead to reliable k* and D* values.

4.2.4 Temperature and strain dependence of k* and D*

Several annealing temperatures in the interval 280°C-475°C were selected for oxygen tracer exchange in order to investigate the temperature dependence of k* and D* from tracer depth profiles. Different time settings were necessary, depending on the temperature, to keep errors of k* and D* as small as possible. For each temperature/time setting a LSC/STO and LSC/LAO pair was annealed in one run to ensure that differences in the tracer profiles are only due to differences in the properties of the thin films. Fig. 29 shows typical ^{18}O depth profiles for both strain states and different temperatures. For all annealing temperatures, tensile LSC/STO was found to have both a higher k* and a higher D* value than compressively strained LSC/LAO. At temperatures above 400°C, tracer profiles for LSC/STO are very flat, due to high values of D*. For such flat profiles the determination of D* becomes very erroneous or even impossible.

Mathematical errors of the entire fitting process were difficult to determine as a consequence of the two-step-iterative fitting procedure. As k* and D* are determined in a step for given β_n and a given/self-consistent L, the system is under-parameterized and calculated errors for k* and D* are consequently too low. These calculated errors would be below 1% for k* and about 1-10% for D* for low values of D*; they are increasing to undefined values for very high D* (flat tracer profiles). Another approach would be to estimate errors by calculating the standard deviation of the measurement points considered for the linear regression lines of the temperature dependence (Fig. 30). This would yield relative errors of $\pm 9\%$ for k* and $\pm 16\%$ for D* in the respective temperature range.
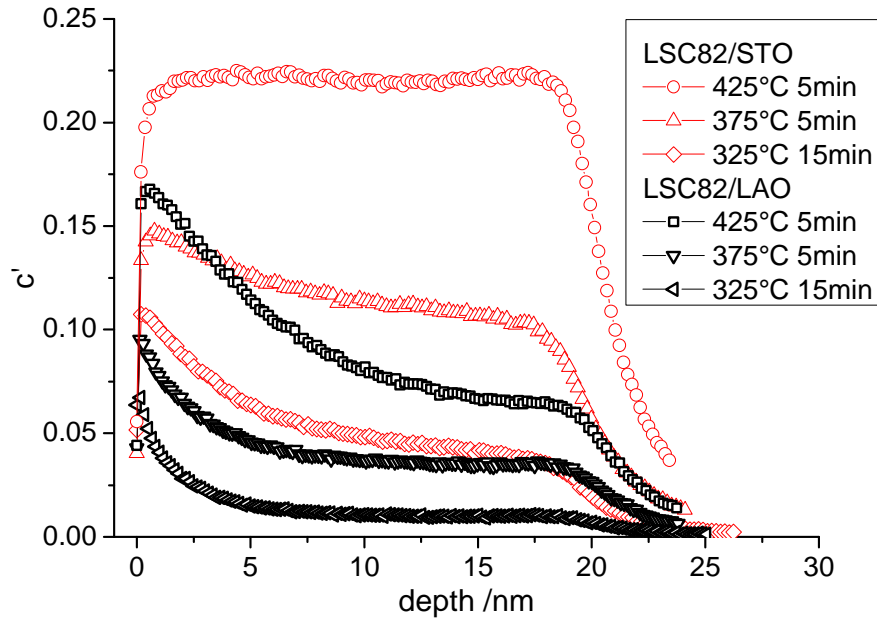
Figure 29: ^{18}O depth profiles in 20 nm LSC82 thin films at different temperatures. For each temperature/time setting, both strain states LSC/STO and LSC/LAO were annealed together in $^{18}O_2$. Tensile LSC/STO incorporates more ^{18}O and has the flatter drop of ^{18}O fraction towards the interface.
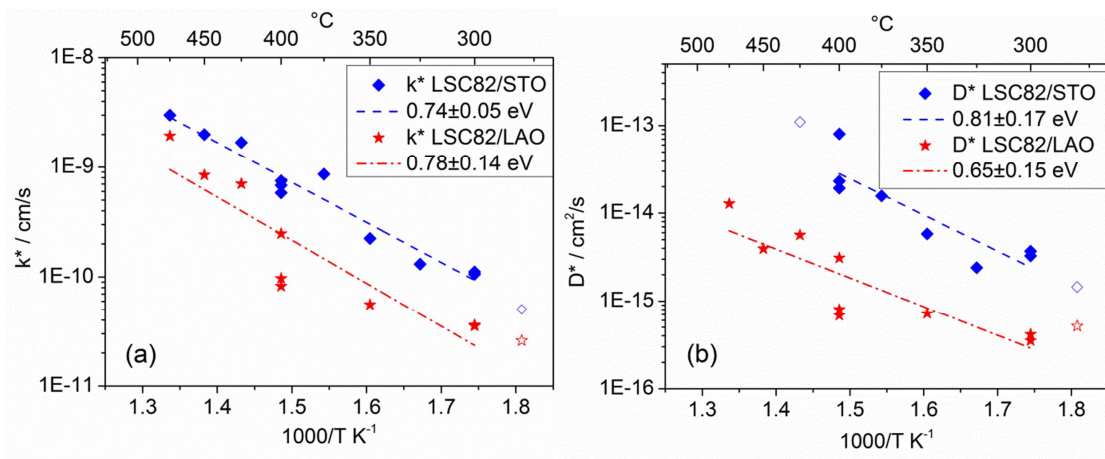
Figure 30: Arrhenius-type diagrams showing the temperature dependence of the coefficients k*(a) and D*(b) for LSC82 thin films extracted from fittings of tracer depth profiles.

Fig. 30 displays Arrhenius-type plots of the parameters k* and D* that were determined for LSC82. k* and D* at the lowest temperature and D* of LSC/STO at the highest temperature (open or missing symbols) are not reliable or are very ill defined, an issue that will be discussed in more detail in Sec. 4.2.5. A linear regression line is shown for the reliable data points. The average differences between the kinetic properties of the strained films are about a factor of 4 in k* and about a factor of 10 in D* with the tensile strained LSC/STO having the higher values. For the temperature range covered here, 280°C-475°C, the values of the activation energies for k* are almost the same for both strain states, 0.74±0.05 eV for tensile, 0.78±0.14 eV for compressive strain. Also activation energies of D* are similar for both strain states (0.81±0.17 eV tensile, 0.65±0.15 eV compressive); because of the uncertainty of individual D* values (flat profiles) the significance of the slight difference in activation energies is uncertain.

There are two important observations about these activation energies found in the thin films – the first is related to their comparison to those reported for bulk LSC samples, and the second is related to their seemingly negligible sensitivity to strain. First, very different activation energies of 1.32 eV for k* and 2.21 eV for D* are reported in literature[122] for LSC82 bulk samples above 600°C. This very strong difference becomes obvious in Fig. 31 where literature data are extrapolated to the temperature regime investigated in this study. Interestingly, the extrapolated lines of high temperature (bulk sample) measurements and low temperature (thin film) measurements of LSC82/LAO for k* and D* both intersect at temperatures close to 450°C and for LSC82/STO close to 550°C. This is an indication that the very different activation energies from bulk and thin films are caused by an intrinsic change within LSC at about 500°C (for the strain-neutral state) rather than an artifact of the preparation of the samples. Unfortunately, measurements at higher temperatures could not be performed on the thin films in this work (as discussed later) to finally prove this interpretation. However, literature data on the temperature dependence of the oxygen vacancy concentration in LSC indicate a change of the kinetic parameters and of the activation energy at about 500°C,[14] This reported transition behavior is in excellent agreement with our findings on the thin film LSC at temperatures lower than 500°C, as explained below.
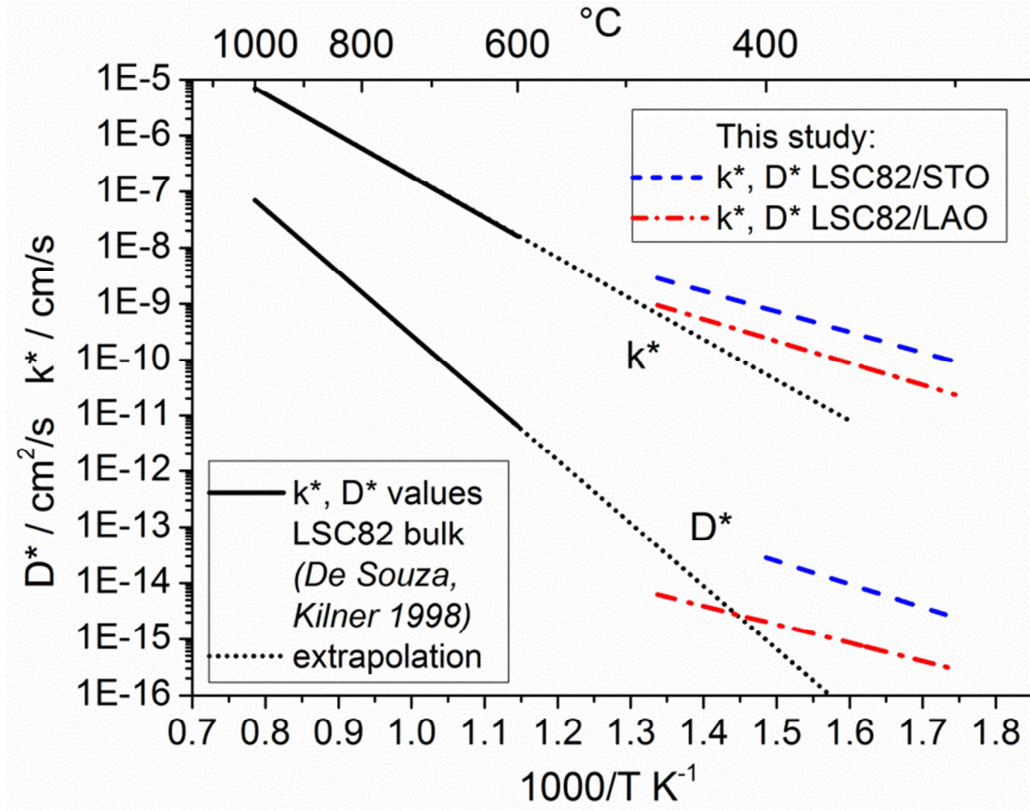
Figure 31: Arrhenius-type diagram comparing literature values of k* and D* obtained on bulk LSC82 [122] to values of differently strained LSC82 thin films investigated in this study.

First it can be noted that the temperature dependency of D* arises both from the enthalpy of oxygen vacancy formation, ΔH^0, and the activation energy for oxygen vacancy migration, E_a. D* is proportional to the product of oxygen vacancy diffusion coefficient, D_V, and the concentration of oxygen vacancies, $[V_O^{\cdot\cdot}]$,

$$D^* = f_c[V_O^{\cdot\cdot}]D_V = \frac{f_c k_B T}{z e_0}[V_O^{\cdot\cdot}]u_V .$$

(17)

Therefore, the change of both D_V and $[V_O^{\cdot\cdot}]$ with temperature contribute to the calculated values of the activation energy here. In Eq. (17) f_c denotes the correlation factor related to crystal structure – typically 0.69 for perovskite-type materials,[131] k

Boltzmann's constant, T the temperature, z the charge number, e_0 the elementary charge, and u_v the vacancy mobility. At temperatures below 500°C almost no change of δ was observed in LSC64 bulk samples (with non-zero values of δ), while for temperatures above 500°C δ increases strongly with temperature.[14] This reflects that the enthalpy of oxygen vacancy formation in LSC is very small below 500°C.

Assuming very little change of the oxygen vacancy concentration with temperature (with a very small formation enthalpy) below 500°C not only in bulk samples[14] but also in thin films, our relatively low activation energy should then reflect almost solely the temperature dependence of the oxygen vacancy diffusion coefficient. This is in good agreement with activation energies of vacancy transport of 0.78-1.08 eV in $La_{0.6}Sr_{0.4}CoO_{3-\delta}$[132] and $LaCoO_{3-\delta}$[133, 134] and in other perovskite-type oxides: 0.6 eV in $SrTiO_3$,[130] 0.86 eV in $Sr(Ti,Fe)O_3$,[135] 0.74 eV in $La_{1-x}Ca_xAlO_{3-\delta}$,[136] 0.6-0.8 eV in $(La,Sr)(Ga,Mg)O_{3-\delta}$.[137, 138] At temperatures, where there is a strong change in δ (>500°C, with a non-zero formation enthalpy), consequently, a higher activation energy is observed for D* than in our study (280°C-475°C).

In order to quantify this difference, the formation of oxygen vacancies $V_O^{\bullet\bullet}$ is described by:

$$O_O^\times + 2h^\bullet \rightleftharpoons \frac{1}{2}O_2 + V_O^{\bullet\bullet} \qquad (18)$$

and the corresponding mass-action law leads to:

$$K = \frac{\sqrt{p_{O_2}}\,[V_O^{\bullet\bullet}]}{[h^\bullet]^2[O_O^\times]} = K_0 e^{-\frac{\Delta G^0}{k_B T}} = K_0' e^{-\frac{\Delta H^0}{k_B T}} \qquad (19)$$

with ΔG^0 denoting the standard Gibbs energy and ΔH^0 the standard reaction enthalpy for vacancy formation. At high temperatures and sufficiently high oxygen partial pressures, the hole concentration can be assumed to be fixed by the Sr-doping level and thus constant. The vacancy concentration is then given by

$$[V_O^{\bullet\bullet}] = \frac{[h^\bullet]^2 [O_O^\times]}{\sqrt{p_{O_2}} K_0^{/}} e^{-\frac{\Delta H^0}{k_B T}} = K_0^{//} e^{-\frac{\Delta H^0}{k_B T}}$$ (20)

and depends on the enthalpy of the vacancy formation reaction Eq. (18). Accordingly the tracer diffusion coefficient becomes

$$D^* = f_c \cdot D_V^0 \cdot K_0^{//} \cdot e^{-\frac{(E_a + \Delta H^0)}{k_B T}}$$ (21)

with

$$D_V = D_V^0 \cdot e^{-\frac{E_a}{k_B T}}.$$ (22)

From Eq. (21) it is apparent that experimentally determined values of the activation energies of D* are the sum of E_a and ΔH^0 at high temperatures $>500°C$. The difference of ~1.5 eV between the high temperature literature value and our activation energy should therefore be close to the activation energy of oxygen vacancy formation ΔH^0. Literature values for ΔH^0 exist for bulk LSC64 (0.89 eV),[139] and are also similar for bulk $La_{0.6}Sr_{0.4}Co_{1-x}Fe_xO_{3-\delta}$ ranging from 0.8eV[140] for x = 0.2, to 1.0 eV [141] for x = 1. Interestingly, for LSC64 thin films an even higher value of 1.29 eV is reported[142] which is observed together with a smaller oxygen vacancy concentration compared to bulk samples. In this approximate model, activation energies of D* in the order of 2 eV are very realistic at high temperatures, and the differences in activation energies can be explained quite well.

As mentioned above, the discrepancies between activation energies at high and low temperatures are higher for D* (avg. 1.48 eV) than for k* (avg. 0.56 eV). Because the oxygen vacancies are thought to play an important role in the surface reactivity of perovskites in oxygen reduction,[143, 144] the activation energy change of k* may also depend on the temperature dependence of δ on the surface. Furthermore, the vacancy formation energy on the surface of oxides, including LSC, is generally lower than that in the bulk.[115, 145, 146] However, it would be necessary to know the exact rate

determining step (rds) of the reaction as well as the temperature dependencies of all involved charge carriers or surface species. The concentration of minority electrons, for example, which are considered crucial for ORR[147, 148] would be showing a different increase with temperature than oxygen vacancies. At this point, it can only be speculated what the reason is for the lower discrepancy between the activation energies of k* on bulk LSC at high temperature and on thin film LSC at the lower temperatures.

Although the exact temperature for the proposed change of regimes at around 500°C could not be measured, further reports exist in literature about transitions of bulk LSC82 in the same temperature range. A semiconductor to metal transition[149] as a result of a change of the rhombohedral angle,[12] a proposed transition of the cobalt spin state (intermediate-high),[150] and a change of thermal expansion[151] are reported. One or more of these transitions are assumed to be connected to the regime-change in the temperature dependence of oxygen non-stoichiometry[14] in LSC, and to the low activation energies of k* and D* in the thin film LSC samples in this study.

Second, it can be noted that the activation energies for k* and D* do not present a change with strain beyond the uncertainty margins. In a previous work, it was shown theoretically that the lattice strain alters the oxygen vacancy formation and migration energies,[115, 116] with a trend of increasing tensile strains associated with lower energies of vacancy formation and migration. Moreover, prior experiments demonstrated a strain effect on the oxygen vacancy content and charge transfer properties[97] in LSC. In this work, the effective activation energies of k* and D* are relatively insensitive to strain, while the magnitude of k* and D* increases when strain varies from compressive to tensile state. In light of Eqs. (19-22), the impact of planar lattice strain in the LSC/LAO and LSC/STO thin films is either on the oxygen vacancy content, or on their mobility, or both. The tensile strain could be favoring a lower vacancy formation enthalpy, but also equally a lowering of the migration barrier. One order of magnitude increase in tracer diffusion coefficient at about 400°C would arise from a 0.14 eV reduction in the vacancy formation enthalpy and/or in the migration barrier (Eq. 21). While this is reflected in the magnitude of D*, a reduction of 0.14 eV is not detectable

in our measured activation energies because of the uncertainty margins being close to 0.15 eV (Figure 30).

Using k* and D* to calculate the critical length (film thickness for which L = 1) leads to different values for the two strain states with 100-150 nm for LSC/LAO and 300-400 nm for LSC/STO in the investigated temperature range. Both values are much smaller than values of 3-150 μm reported for bulk LSC in literature.[14, 122-124] However, due to the different activation energies of k* and D* in literature, critical lengths strongly depend also on temperature. Critical lengths of more than 50 μm are found at 1000°C while 3-5 μm are reported 600°C for LSC82 bulk samples.[122] Extrapolating those data (as shown in Fig. 31) to 400°C, without considering the activation energy change, leads to a critical length of about 150 nm, which is well in range of the measured values in this study for thin films.

4.2.5 Limitations of the method and the temperature range

Although it is desired to measure only the profiles caused by tracer diffusion, chemical diffusion could not be avoided under the given experimental conditions. It was particularly challenging to realize very short diffusion times of only 4 or 5 minutes to still obtain reasonable concentration gradients in LSC. In literature[32, 122, 152] it is often suggested to extensively pre-anneal the films either in oxygen or in ambient air before tracer experiments in order to chemically equilibrate the material and thus to avoid chemical diffusion. Here this procedure would not improve the situation, because further stoichiometry changes during evacuation before tracer exposure are hardly avoidable. Trying to avoid the problem by a very fast evacuation and refilling process would here be in vain, as the time constant of chemical equilibration is too short. This time constant can be estimated from impedance measurements performed on similar thin films on YSZ (time constant of the semicircle featuring the chemical capacitance), and is about 1-5 seconds at 400°C. Extrapolating the time constant for the lower temperatures yields higher values, but they are yet still below one minute at 280°C. One might pre-equilibrate the sample, quench it to room-temperature, perform the

tracer exchange at room temperature and heat the sample back to annealing temperature. Then, however, the heating step would have to be much faster than the annealing time (typically 5 minutes here), which was not possible in our set-up. Hence, a simultaneous occurrence of tracer and chemical diffusion could not be avoided in this study. The only viable way to completely avoid a chemical contribution in ^{18}O profiles would be to use continuous gas flows at high flow rates with fast changes from ambient to tracer-enriched oxygen retaining the same $p(O_2)$ during the whole procedure, which would be extremely $^{18}O_2$ consuming and costly.

Oxygen non-stoichiometry of $La_{1-x}Sr_xCoO_{3-\delta}$ adapts to evacuation by increasing δ. After re-filling with $^{18}O_2$ to 200 mbar, δ returns to the original value by incorporation of oxygen into LSC. As only ^{18}O isotope is available for this readjustment of δ, an ^{18}O tracer profile from chemical diffusion is created. This "chemical" tracer profile depends in size and shape on the change of δ and the coefficients k_{chem} and D_{chem}. Simultaneous with the formation of this chemical tracer profile, and also continuing after the usually fast chemical incorporation/diffusion process, tracer exchange and tracer diffusion takes place in the system governed by k^* and D^*. As both processes have different driving forces and different time constants, a very complex, combined diffusion profile is generated over time.

A way to handle this problem and to still measure meaningful values for k^* and D^* is to keep the amount of ^{18}O incorporated by chemical driving forces very low compared to the amount of ^{18}O incorporated *via* pure tracer exchange. Then resulting profiles are still very close to profiles generated by only tracer exchange and diffusion while chemical incorporation/diffusion can be neglected. For annealing at low temperatures this can only be realized by long annealing times. For very long annealing times, though, another limiting effect becomes relevant: Longer annealing times inevitably lead to profiles with smaller relative drops of tracer fraction as shown in Fig. 32. Due to the flatter profiles, D^* becomes more and more ill-defined. For even higher annealing times, finally also k^* becomes undefined as the thin film gets almost completely filled with tracer. Therefore, an ideal time setting has to be found for each temperature, for which the influence of chemical tracer incorporation is negligible, but

not too much tracer is incorporated so that simultaneous determination of k* and D* remains possible with acceptable errors.
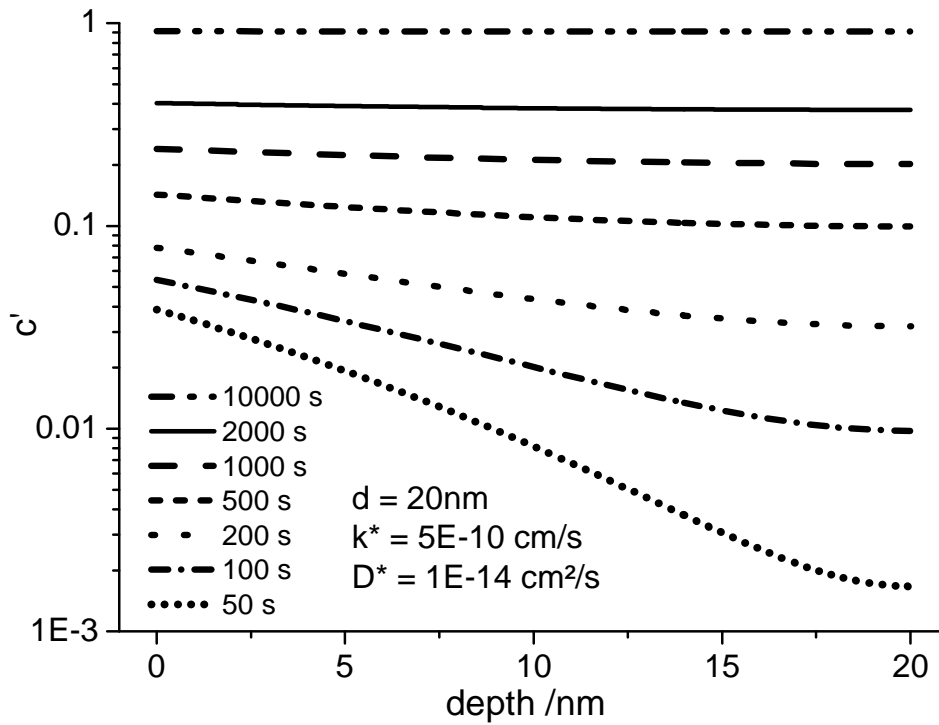
Figure 32: Simulated depth profiles using Eqs. (14) and (16) for different annealing times with typical values of d, k and D*. A logarithmic y-scale is used to show that the relative drop in the profiles decreases with annealing time, leading to higher errors in D*.*

The influence of chemical tracer incorporation at low temperatures could be clearly shown in additional experiments at 280°C and different annealing times (1-36 min). The amount of tracer incorporated into LSC for small times does not follow the expected behavior for pure tracer diffusion. Rather, a bigger amount of tracer than expected is incorporated in the first minutes. Furthermore it was observed that tracer profiles in which an influence of chemical tracer incorporation is expected (low temperatures/times) could not be fitted satisfactory with the formulas valid for tracer diffusion (Eqs. 14 and 16). A steep drop in tracer fraction at the surface followed by a

flat diffusion tail towards the interface was observed - features that could not be adjusted simultaneously. From variation of annealing time in these measurements it was concluded that the tracer close to the surface followed by a steep drop is incorporated by chemical driving forces. Therefore, k* and D* values for LSC82/LAO (see Fig. 30) at 280°C for which these effects could be observed, were also not included in activation energy calculations (the open symbols in Figs. 30a, 30b).

4.2.6 Effect of chemical surface modification

The formation of Sr enrichments at the surface and its removal by chemical etching was extensively described in Sec. 2. Here, by etching 5 seconds in diluted (0.12 mol/l) HCl, about 3 nm of the LSC thin films were removed from the surface. Tracer profiles after annealing as-prepared and etched LSC films on STO and LAO in $^{18}O_2$ at 400°C for 5 minutes are shown in Fig. 33. Etched thin films exhibited a higher surface exchange coefficients compared to as-prepared films. This fact corresponds to the larger tracer amount in etched films, clearly visible in Fig. 33. A small contribution of the increase of k* might also be caused by a slight roughening of the surface by the etching process. Differences in D* are found only for LSC/STO at 400°C and most probably reflect the large uncertainties for the very flat profiles, rather than true differences. However, the fact that after removing about 3 nm from the film surface the same effect of tensile over compressive strain on oxygen exchange is observed is further evidence that the films are fully strained over the whole 20 nm thickness. Also it can be excluded that possible differences of the surface cation composition of LSC/LAO and LSC/STO from preparation are the cause for their differences in respect to surface oxygen exchange of the two strain stated. ^{18}O exchange of etched samples was performed together with non-etched samples, annealing parameters and k* and D* values are given in Tab. 2.
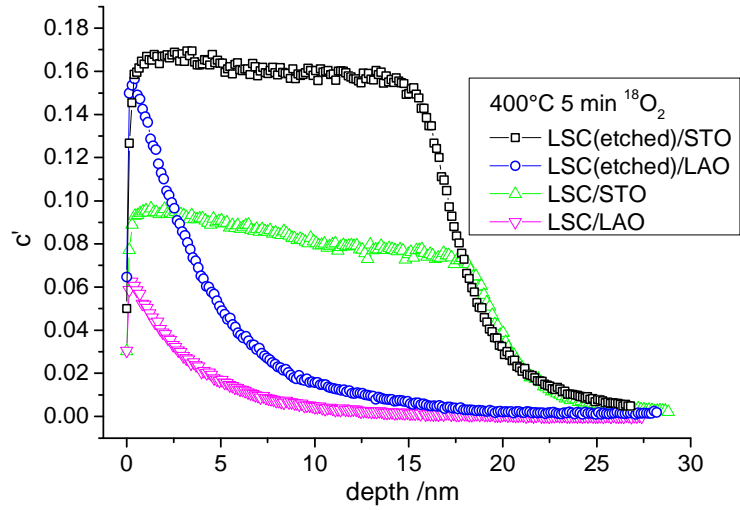
Figure 33: Tracer depth profiles comparing etched and as-prepared LSC82 thin films annealed together at 400°C for 5 minutes. Etched thin films exhibit a higher tracer surface exchange coefficient k*.

Table 2: Annealing parameters and fitted values of k* and D* of etched LSC82 thin films. For D* values higher than 10^{-13} cm^2/s, no significant evaluation of D* is possible due to the almost flat tracer depth profiles.

Sample	Time in $^{18}O_2$ / min	Temperature / °C	k* / 10^{-10} cm/s	D* / 10^{-15} cm^2/s
LSC(etched)|STO	5	400	10.1	43
LSC(etched)|LAO	5	400	2.61	0.77
LSC|STO	5	400	5.83	19
LSC|LAO	5	400	0.967	0.80
LSC(etched)|STO	5	450	24.2	(>100)
LSC(etched)|LAO	5	450	9.34	3.7
LSC|STO	5	450	20.1	(>100)
LSC|LAO	5	450	8.45	3.9

4.2.7 Films without predominant strain

In addition to strained LSC films, 20 nm LSC82 thin films grown on MgO without predominant strain state were investigated. The aim was to use LSC on MgO as a strain-neutral reference-sample to investigate whether the differences in oxygen surface exchange and diffusion observed in strained samples are caused by an activating effect of tensile strain or by inhibition from compressive strain, or if both effects are present. In Fig. 34, depth profiles of LSC thin films on MgO are compared to strained films on STO and LAO at 300°C and 400°C. The deduced parameters k* and D* for 300°C, 350°C and 400°C are given in Tab. 3.

Thin films on MgO exhibit k* and D* values between those of the two strained films, but values are closer to the tensile strained LSC on STO, especially for low temperatures. This would suggest that both an activating effect for tensile strain and an even stronger deactivating effect of compressive strain are present. It has to be stated though, that for an unambiguous comparison an epitaxial (100) thin film on a blocking substrate without any strain throughout the whole temperature range would be needed. In case of the thin films on MgO it is probable that values of k* and D* are also affected by grain boundaries or different orientations of the surface. A final conclusion is therefore problematic. Recent experimental data and simulations[97, 112, 115] also suggest that both an activating and a deactivating effect can be observed depending on strain states. Those are attributed to changes of the near-surface oxygen vacancy concentration and electronic structure indicated by presence of Co^{2+} states measured by scanning tunneling microscopy and changes of the activation barrier in simulations on oxygen migration in the $LaCoO_3$-system.
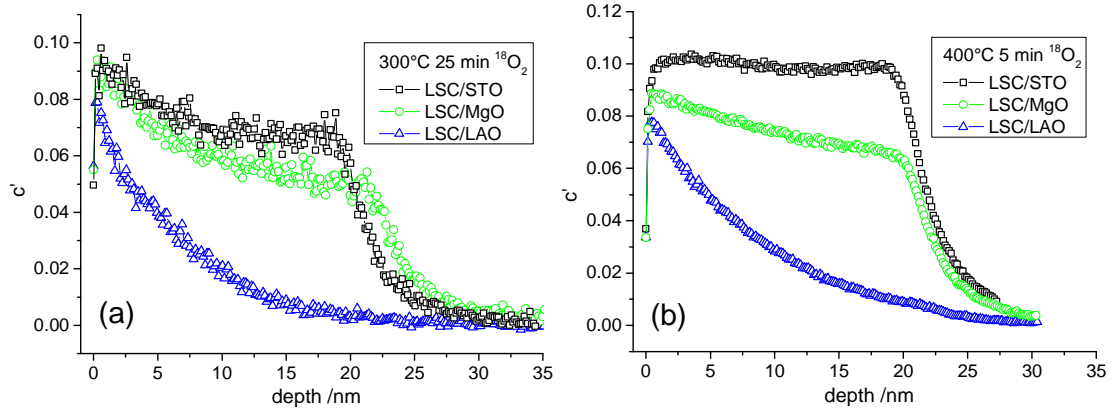
Figure 34: Tracer depth profiles comparing epitaxial and strained LSC82 on STO and LAO to non-epitaxial LSC82 on MgO without predominant strain at 300°C (a) and 400°C (b).

Table 3: Annealing parameters and fitted values of k* and D* of strained epitaxial LSC82 thin films compared to polycrystalline films on MgO without predominant strain.

Substrate	Time in $^{18}O_2$ / min	Temperature / °C	k* / 10^{-10} cm/s	D* / 10^{-15} cm^2/s
STO	25	300	1.06	3.7
MgO	25	300	1.02	2.4
LAO	25	300	0.353	0.35
STO	5	350	2.24	5.8
MgO	5	350	1.63	5.3
LAO	5	350	0.557	0.72
STO	5	400	7.51	(80)
MgO	5	400	5.87	26
LAO	5	400	2.47	3.1

4.2.8 Different compositions of LSC

The strontium level in $La_{1-x}Sr_xCoO_{3-\delta}$ is known to strongly affect the electronic band structure as well as the oxygen non-stoichiometry.[14, 153-155] Two different LSC-compositions, LSC82 and LSC64 were therefore investigated at different temperatures. Fig. 35 displays profiles for both compositions measured after annealing in $^{18}O_2$ at 375°C for 5 minutes and Tab. 4 contains the fitted values of k* and D*. Obviously, the higher Sr substitution level led to a higher surface exchange rate and diffusion coefficient in LSC64 thin films.
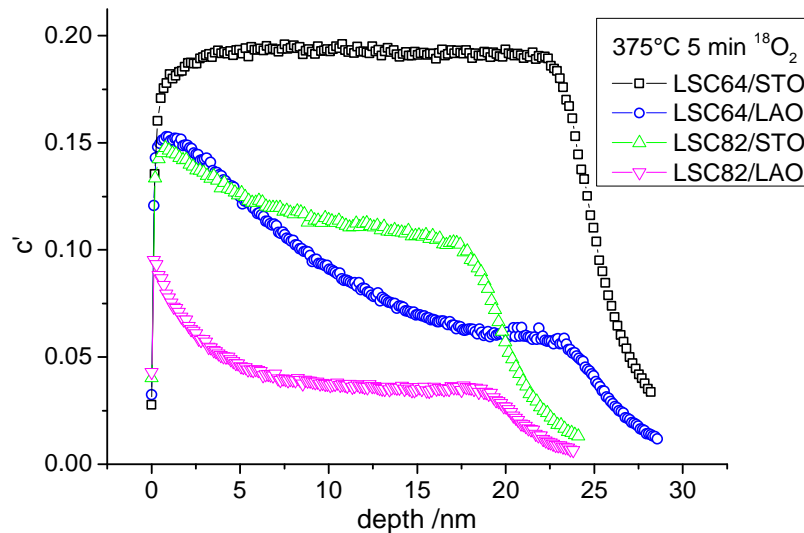
Figure 35: Tracer depth profiles comparing epitaxial and strained LSC films with the compositions $La_{0.8}Sr_{0.2}CoO_{3-\delta}$ (LSC82) and $La_{0.6}Sr_{0.4}CoO_{3-\delta}$ (LSC64). The higher Sr content in LSC64 leads to higher k and D* compared to LSC82, and the same tendency is found for the strain states (tensile > compressive) in both compositions.*

Table 4: Annealing parameters and fitted values of k* and D* of strained LSC82 and LSC64 thin films at 325 and 375°C. For D* values higher than 10^{-13} cm²/s, no significant evaluation of D* is possible due to the almost flat tracer depth profiles.

Sample	Time in $^{18}O_2$ / min	Temperature / °C	k* / 10^{-10} cm/s	D* / 10^{-15} cm²/s
LSC64|STO	5	375	17.8	> 100
LSC64|LAO	5	375	8.21	8.1
LSC82|STO	5	375	8.63	16
LSC82|LAO	5	375	3.10	6.3
LSC64|STO	15	325	4.65	> 100
LSC64|LAO	15	325	1.24	0.95
LSC82|STO	15	325	1.31	2.4
LSC82|LAO	15	325	0.359	0.55

Besides the higher absolute values, the same general dependence on the strain state was found with higher k* and D* for tensile strained LSC/STO. As a result of the higher diffusion coefficient, profiles of LSC64/STO are almost completely flat – therefore it can be concluded that D* is higher than for LSC82, but it is not possible to determine a value for D*. This effect of the higher Sr substitution level leading to faster oxygen exchange kinetics can be consistently found in results obtained on bulk LSC[122, 143, 156-158] and is often attributed to the higher concentration of oxygen vacancies in LSC64 and its different electronic structure. Also the higher D* value of LSC64 can, at least partly, be attributed to the higher oxygen vacancy concentration.

4.3 Conclusions

Oxygen tracer profiles generated in differently strained epitaxial 20 nm $(La,Sr)CoO_{3-\delta}$ thin films were measured after annealing in $^{18}O_2$ atmosphere. Both the surface exchange coefficient k* and the diffusion coefficient D* were extracted simultaneously

from depth profiles, despite the very small thickness. Within the entire temperature interval of 280-475°C and for two compositions (LSC82 and LSC64), both k* and D* are always found to be higher for tensile strained LSC on STO compared to compressively strained LSC on LAO. An enhancing effect of chemical etching on k* is measured for both strain states and attributed to the removal of a surface Sr enrichment. Activation energies of both k* and D* in the range 280°C-475°C are much lower than those reported for bulk LSC at higher temperatures. This difference is suggested to be due to the temperature independence of the oxygen non-stoichiometry, δ, at temperatures lower than 500°C, causing higher activation energies above 500°C and much lower ones in this study below 500°C. While the enhancements in k* and D* of tensile LSC films with respect to the compressively strained LSC thin films is highly reproducible, the exact values of k* and D* and their temperature dependence are prone to some errors. The reason is that the investigation method is close to its geometrical limit - the sample thickness of 20 nm is very small to extract a well evaluable SIMS depth profile on a good mixed conducting oxide as LSC. In addition, the temperature/time settings for annealing have to be well adjusted to extract both k* and D* and to minimize the influence of chemically-driven tracer incorporation. The consistency of the strain-dependence of k* and D* across all samples that were systematically surveyed here, together with the previous theoretical predictions, suggest that lattice strain is an important parameter to control the reactivity of perovskite cathodes to oxygen reduction reaction.

5 A Novel ToF-SIMS Operation Mode for sub 100 nm Lateral Resolution

This chapter contains in large part material submitted as scientific paper to the journal "Applied Surface Science".

ToF-SIMS has become a very popular technique for obtaining well resolved elemental and isotopic maps in two or three dimensions.[159-162] While SIMS is a very sensitive technique for qualitative analysis, a quantitative elementary analysis from secondary ions is often not possible due to the complex sputter and ionization processes and matrix related differences in secondary ion intensities.[163-165] Isotopic analysis of a single element by SIMS is usually less problematic. However, mass fractionation or nonlinearities of the detection system can account for errors in the determination of isotope fractions. Mass fractionation is most troublesome for H and D[166] and only a minor problem for elements with higher mass such as oxygen.[167, 168] Detection related errors can occur for all elements: a bad signal/noise ratio for minority isotopes and detector saturation/dead time effects as well as ion interaction in case of majority isotopes can cause serious problems for determining correct isotope fractions.[169-171] The isotope analysis of oxygen with ToF-SIMS is of special interest for functional oxides and examples demonstrating its potential for gathering thermodynamic and kinetic parameters of oxygen exchange and ion transport in oxides are given in the previous chapters. Several techniques for analyzing tracer distributions are employed, such as depth profiling,[121, 172] laterally resolved analysis of electrochemically active zones[173, 174] or of angle polished depth profiles,[175] and also combined analysis for experiments requiring 3D data.[127]

However, the analytical challenges for the ToF-SIMS measurements in the above chapter could not be satisfyingly performed in the common measurement modes. Adapting the beam guidance of the primary ion beam led to a novel operation mode for ToF-SIMS, which was developed together with G. Holzlechner. The novel ToF-SIMS

operation mode is called "collimated burst alignment" (CBA) mode, and is described in this chapter. Its main features are an improved lateral resolution, accuracy of isotope fractions and adjustability of primary ion currents. Mass spectra were analyzed in detail in order to understand the reasons of improved characteristics, particularly of improved accuracy of isotope fractions. Several application examples of the CBA mode are shown in order to demonstrate its excellent performance and capabilities for investigating scientific problems in materials research. Although isotope analysis of oxygen is primarily discussed, the novel operation mode is also adjustable for isotope analysis of other elements and applicable as imaging mode with high lateral resolution. It is further shown that the higher ion currents of the CBA mode compared to other imaging modes still retain the possibility of measuring with reasonable mass resolution in burst mode.

5.1 Experimental

5.1.1 Instrumental details

Time of flight secondary ion mass spectrometry was performed on a TOF.SIMS 5 (ION-TOF, Germany) instrument. 25 kV Bi_1^+ and Bi_3^{++} were used as primary ions in different operation modes. The novel CBA mode and the related CBA-burst mode are compared to the BA and BA-burst mode. In both burst modes, 8 ion pulses were analyzed. Areas of 12×12 μm² to 150×150 μm² were investigated using a raster of 256×256 or 512×512 measured points. Negative secondary ions were analyzed and detailed information on the settings is provided with the particular application examples. For depth profiling and ablation of the surface, 2 kV Cs^+ ions (500×500 μm², ca. 120 nA) were employed. For charge compensation, a low energy electron flood gun (20 V) was used.

5.1.2 Conventional ToF-SIMS operation modes

The primary ion column in TOF.SIMS 5 instruments has 3 lenses, enabling operation with different primary ion beam guidances. Three main operation modes are suggested by the manufacturers. High current bunched (HCBU) mode enables to measure with high currents and high mass resolution but very low lateral resolution. Burst alignment (BA) mode is a versatile mode, allowing reasonable lateral resolution (~250 nm) at moderate primary ion currents. By operating the BA mode in the so called burst mode, the usually low mass resolution (m/Δm ~200) can be improved to m/Δm > 6000 at the cost of lower currents. The collimated mode is an imaging mode, allowing a lateral resolution of about 100 nm at very low currents and low mass resolution. Application of the burst mode to increase mass resolution is impracticable due to the low currents. The important characteristics of these operation modes are summarized in Tab. 5 and respective beam guidances are outlined in Fig. 36.

Table 5: Primary ion gun operation modes and important characteristics for a Bi-cluster liquid metal ion gun (LMIG) on a ToF-SIMS 5 instrument.

Operation Mode	HCBU	BA	Collimated	CBA
Lens Source	~3150 V	~3300 V	~3900 V	~3750 V
Lens Mag	~14.8 kV	0 V	0 V	12 – 13 kV
DC-current	~15 nA	0.4 – 0.7 nA	50 pA	70 – 100 pA
Crossovers	2	1	0	1
Lateral Resolution (lr)	2-10 μm	~250 nm	~100 nm	Bi^+: 96 < lr < 136 nm Bi_3^{++}: 68 < lr < 96 nm
Mass Resolution Burst	~11000 ×	Unit (~200) > 6000	Unit (~200) (>6000)	Unit (~200) > 6000
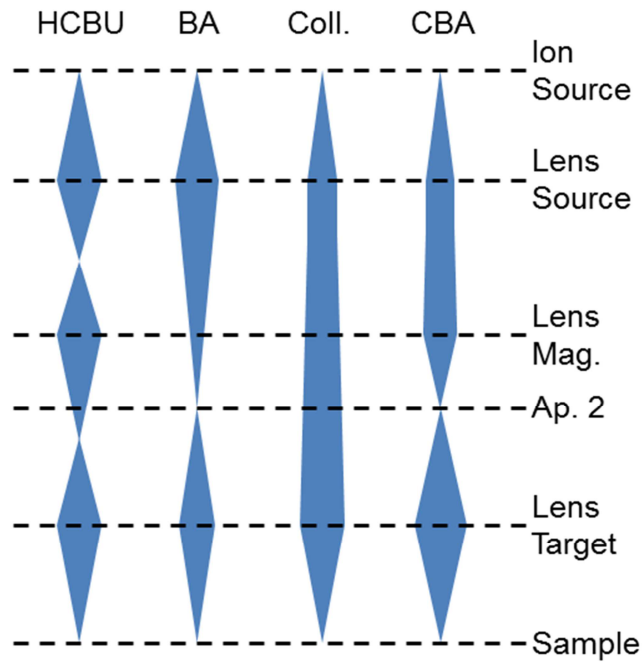
Figure 36: Schematics of beam guidance in several TOF.SIMS 5 operation modes.

5.1.3 CBA mode

The notation "collimated burst alignment" (CBA) mode was chosen for the novel operation mode as it shares characteristics with both the collimated mode and the BA mode. In the upper part of the ion gun, the beam is almost parallel, very similar as in the collimated mode. In the lower part of the ion gun, the beam is focused into a crossover (at Aperture 2) before it is focused on the sample, exactly as in BA mode (cf. Fig. 36).

For adjusting the CBA mode, we suggest to start from the BA mode. First, the voltage on Lens Source (i.e. the lens closest to the Bi-emitter, cf. Fig. 36) is increased. Consequently, the beam focus is widened and thus the beam becomes more parallel. Second, the voltage on Lens Magnification is also increased until the beam is focused into a crossover at Aperture 2 (as in BA mode). In the lower part of the column, the beam is then focused on the sample with similar settings of Lens Target as in BA mode.

Everyday adjustments for measurements are therefore almost identical to those of the BA mode. More details on the adjustment and operation of the CBA mode is given in Ref. [176].

As the voltages of Lens Source and Lens Magnification can be very finely controlled, the CBA mode is almost continuously adjustable from the BA mode. Increasing both lens voltages chiefly means trading a lower primary ion current for increased lateral resolution. This reduced current, however, is not necessarily a disadvantage for measurements; in case of oxygen isotope analysis for example, O^- has a very high secondary ion yield and the reduction of the primary ion current can even be necessary to avoid ion interaction and detector dead time effects and to maintain the accuracy of the measured oxygen isotope fractions. This requirement is much better met in CBA mode compared to the BA mode. The correlations of dead time effects, integration times, Poisson correction and accuracy of isotope fractions in CBA and BA mode are explicitly described elsewhere.[176]

Regarding the adjustability of the CBA mode, the values of currents and lateral resolution given in Tab. 5 are values optimized for measurements on the functional oxides employed in this study. However, using lens voltages between the values given for BA and CBA mode could be advantageous for measurements in other systems, leading to ion currents and resolution values between those given in Tab. 5 for BA and CBA. Using the CBA mode as high resolution imaging mode also enables to measure with simultaneously high lateral and mass resolution in burst mode as demonstrated in Sec. 5.3.

One disadvantage of the CBA mode is the slightly higher beam angle at the target compared to the BA mode. Although the differences are not severe, this leads to a lower depth of focus, and consequently makes the exact adjustment of the sample height important in CBA mode. It should be mentioned, though, that depth of focus is of minor significance for ToF-SIMS measurements, as height differences and high sample roughness lead to unwanted shading or geometry related artifacts and have to be avoided anyway.[177, 178]

5.2 Measurements making use of the high lateral resolution

5.2.1 General remarks on lateral resolution and static SIMS

Lateral resolution is an important characteristic not only for ToF-SIMS, but for all imaging techniques. The term resolution originates from optical microscopy [179] and today lateral resolution it is defined in ISO 22493:2008 as "the minimum spacing at which two features of the image can be recognized as distinct and separate".[180] However, several different approaches are common in the SIMS community to measure values of primary ion beam quality (such as sharpness) that are then called "lateral resolution" as pointed out by Senoner et. al.[181] In the same contribution, the coherences of the point spread function of the primary beam and image resolution, and the role of contrast and noise for measuring with a certain lateral resolution are described in detail. Further, a method to determine the lateral resolution is suggested [181]. As different measurement methods are used in the SIMS community and many of them do not meet the ISO definition, values for lateral resolution are often not directly comparable. For determination of the lateral resolution of the CBA mode, the method and criterion suggested by Senoner et. al.[181] was employed. Lateral resolutions (lr) of 96 nm $<$ lr $<$ 136 nm for Bi_1^+ and 68 nm $<$ lr $<$ 96 nm for Bi_3^{++} were determined on a BAM-L200 certified reference sample with details on the measurements and evaluation of lateral resolution in CBA mode being given in Ref. [176].

Static SIMS and dynamic SIMS are two different methods and approaches for investigations with SIMS. The main difference is the current of primary ions and the damage inflicted by them to a target surface. Dynamic SIMS works with high currents and accepts the damage of the target surface and uses the ablation for depth profiling. Static SIMS uses much lower currents in order to keep the damage of a target area small. Measuring for a certain time on the same surface area should therefore yield the same undisturbed signal, if the ion dose per area is under the so called "static limit".[182] This limit varies with the primary ions, their energy, and the target surface. Often either disturbing less than 10% of a target surface [183] or an ion dose of

$\sim 10^{12}$ primary ions per cm^2 [162] is given as static limit (a typical surface consists of $\sim 10^{15}$ atoms/cm^2). Although ToF-SIMS and static SIMS are sometimes synonymously used, it has to be noted that by improving the lateral resolution it becomes more difficult to remain within the static limit. The connection becomes clear when imagining a primary ion source with ideal (atomic) lateral resolution. For realizing this lateral resolution, all surface atoms have to be hit by primary ions and removed to be detected as secondary ions. However, this type of operation is clearly dynamic SIMS.

A quick calculation for a typical measurement in the CBA mode, assuming a Bi$^+$ primary ion current of 0.04 pA at a measurement frequency of 40 kHz and a 100×100 nm^2 square and homogeneous primary ion spot, yields about 13 shots at the same target spot to reach a dose of 10^{12} ions per cm^2, the estimated static limit. A typical point spread function of a primary ion beam with higher intensity in the middle of a 100×100 nm area reduces the static limit to even less. Also using Bi$_3^{++}$ as primary ions reduces the shots to reach the static limit by a factor of 1.5 at the same primary ion current. By this calculation it can be shown that CBA mode can still be operated within the static limit condition, but care has to be taken. It has to be noted that measuring with lateral resolutions ≤ 100 nm bears the risk of violating the static limit without being aware of it. Further improving the lateral resolution of ToF-SIMS instruments to values below 20 nm [184] as is desired by manufacturers and researchers alike, might even be completely incompatible with the limits of static SIMS.

5.2.2 ^{18}O incorporation into YSZ via Pt electrodes

The oxygen reduction reaction on platinum and incorporation of oxygen into solid electrolytes is a model reaction for many applications (fuel cells, sensors, catalysis). Here SIMS measurements are presented for visualizing the electrochemically active sites of the model system Pt(O$_2$)|yttria stabilized zirconia (YSZ) by means of ^{18}O tracer incorporation. The tracer experiments were conducted at ~290°C and ^{18}O was incorporated into YSZ (111) single crystals (9.5 mol% Y$_2$O$_3$) on square shaped (100×100 μm^2) Pt thin film electrodes by applying a cathodic dc voltage. The tracer (^{18}O$_2$ gas) was locally supplied to the Pt microelectrode by a quartz capillary and different voltages were used (between -2.1 and -2.5 V); for experimental details the reader is referred to Ref. [173]. After ^{18}O incorporation and before SIMS measurements, the Pt electrodes were removed from YSZ by etching in hot nitro-hydrochloric acid. This important step guarantees a surface without height differences for SIMS analysis and additionally avoids measurement artifacts caused by distortions of the extraction field of secondary ions by areas with different electrostatic charge (Pt, YSZ) during the dynamic sputter process. Similar measurements have already been reported in literature,[173, 185-189] but here it is shown that applying the novel CBA measurement mode (and hereby improving the lateral resolution) helps unveiling further details of the oxygen incorporation process as shown in Fig. 37.

Measurements were performed in CBA mode with Bi$^+$ primary ions. ^{18}O distribution images of 130×130 μm^2 and 12×12 μm^2 size were measured with a resolution of 512×512 and 256×256 pixels, respectively, and detail images were integrated over 900 image scans. Line integration within the detail images was used to investigate the lateral distribution of the active area for oxygen incorporation. The integration area was chosen on a straight Pt edge to minimize the blurring effect of the electrodes waviness – cf. the rectangular box in Fig. 37b. The lateral profiles resulting from line integration are depicted in Figs. 37c and 37d in linear and logarithmic scale, respectively. These images show the tracer fraction as a function of lateral position.
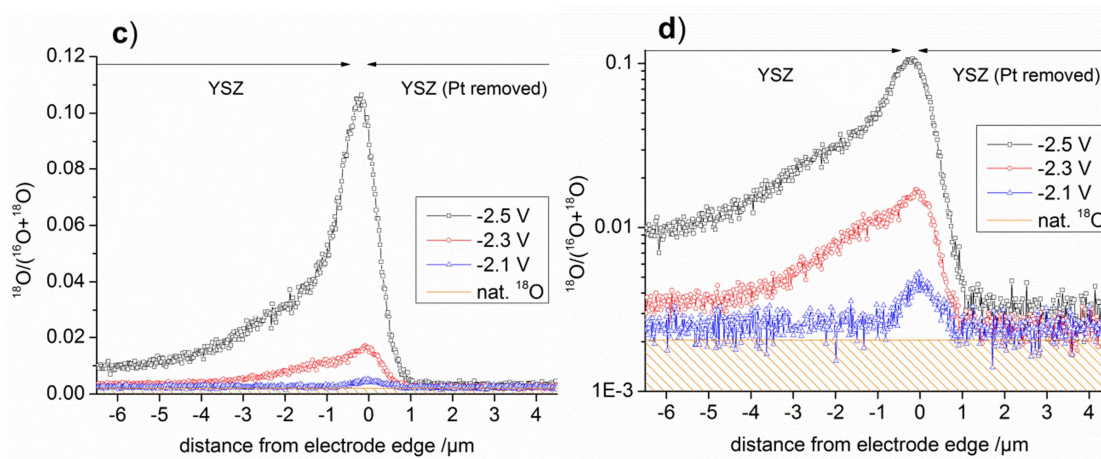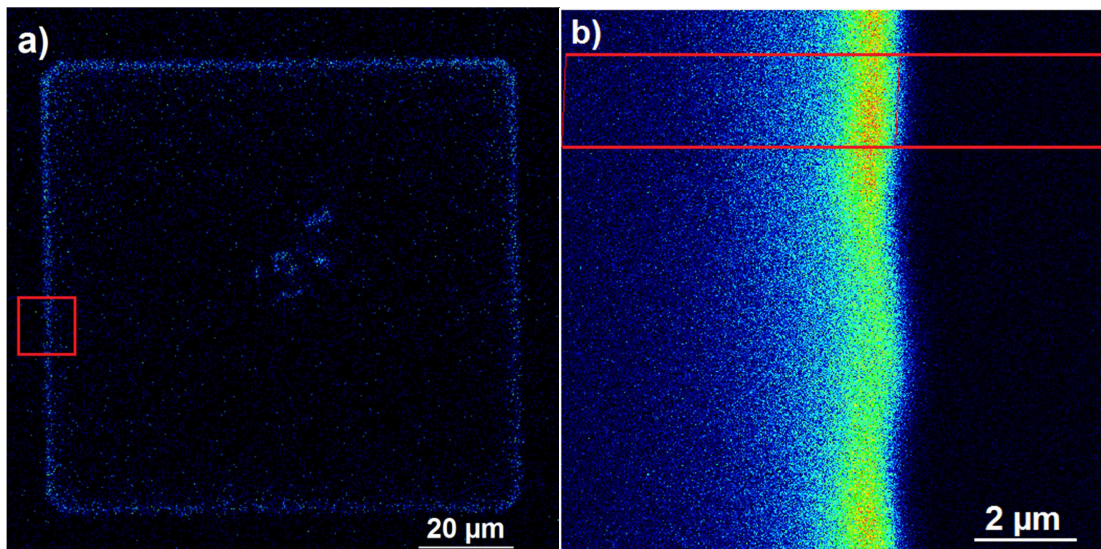
Figure 37: a) Overview image of (111) YSZ after ^{18}O incorporation with -2.5 V set voltage (Pt electrode removed); b) detail image of a former Pt|YSZ phase boundary (highlighted area in a); c,d) linear and logarithmic plot of the ^{18}O fraction in the line scan/integration area in b) and of equivalent experiments using lower overpotentials.

Three different reaction sites for oxygen incorporation and exchange can be distinguished in the lateral profiles in Figs. 37c, d:

(i) Beneath the Pt electrode, caused by oxygen incorporation at the Pt|YSZ interface.[173, 190] Grain boundaries in Pt are suggested to offer a pathway for oxygen

through the gas tight thin film. Since the size of Pt grains is only about 100 nm and the differences in ^{18}O fractions are very low, the grain boundaries cannot be resolved in these measurements. The amount of tracer incorporated within the given time (i.e. the faradaic current during the incorporation experiment) is in acceptable agreement with data from electrochemical measurements.[190, 191]

(ii) The increased tracer incorporation in a zone close to the triple phase boundary (TPB) extending along the free YSZ surface was already discussed to proceed via an electrolyte surface path [173, 191]. This means O_2 adsorbs on the electrolyte and electrons for reduction are supplied by YSZ. At the given temperatures ($\sim$290°C) the Pt electrodes are electrochemically highly blocking and stoichiometry polarization takes place in YSZ upon high cathodic polarization. This leads to an increased electron concentration within the electrolyte in the vicinity of the electrode, and caused the strong increase in oxygen incorporation rate on the YSZ surface close to the TPB.

(iii) On YSZ surface regions far enough from a polarized electrode to be not affected by stoichiometry polarization, tracer incorporation proceeds via a "classic" entropy driven oxygen tracer exchange process. This process could only be monitored in case of the lowest polarization (η = -2.06 V) on the YSZ part far away from the electrode edge (blue curve in Figs. 37c and 37d, x-scale -6 to -2 μm)

The oxygen incorporation on stoichiometry polarized YSZ close to the TPB (path ii) causes a strongly asymmetric lateral profile. In Ref. [173] this asymmetry could only be resolved for very high cathodic polarization. The improved resolution of the CBA mode now allows us to visualize this asymmetry also for lower cathodic overpotentials. The broadening along the free YSZ surface strongly depends on the polarization, in agreement with the strongly voltage dependent electron concentration due to stoichiometry polarization in YSZ. A plot of the relative tracer fractions close to the Pt|YSZ edge is shown in Fig. 38. The sharpness of the ^{18}O drop beneath (removed) Pt is between 400 and 500 nm for all electrode polarizations (84% to 16% intensity drop).
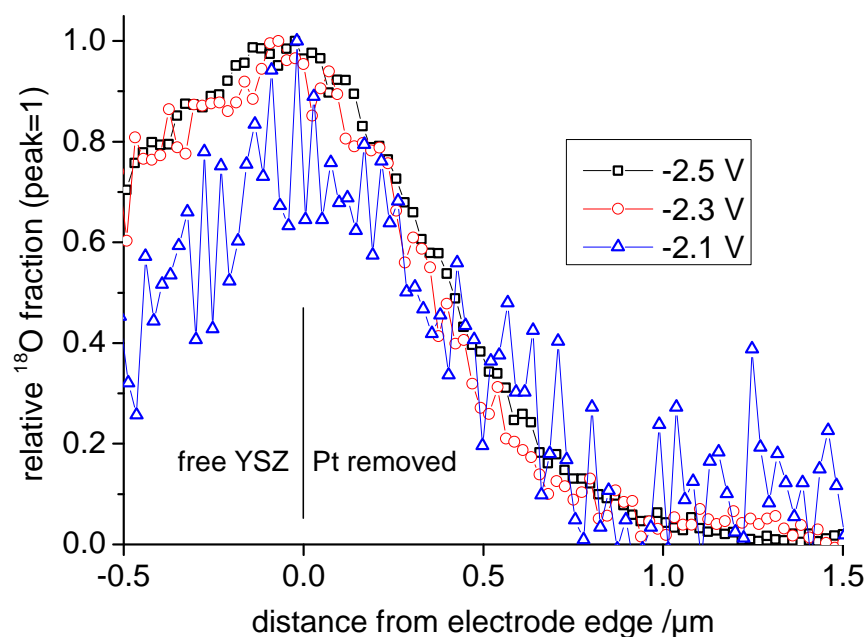
Figure 38: Extension of oxygen incorporation beneath a Pt electrode. Tracer fractions related to the respective maximum tracer fractions are plotted for different set voltages.

In the present study the sharpness is limited by the following effects: diffusion of tracer in YSZ during the experiment (about 280 nm diffusion length for given time and temperature),[192] lateral resolution of the beam (~100 nm), waviness of the electrode edge in the integration area (100–200 nm, estimated from SEM images) and slight beam shifts during ToF-SIMS measurements. The experimentally found decay length of the lateral tracer profile beneath Pt of 400–500 nm can thus be concluded to be predominantly caused by other factors than by a true broadening of the electrochemically active zone along the Pt|YSZ interface. Only the broadening along the free YSZ surface reflects an electrochemical effect. Consequently it can be concluded from these new, highly resolved measurements, that the active zone of oxygen incorporation on Pt|YSZ upon high cathodic polarization shows a very asymetric extension along the free YSZ surface and virtually no extension beneath the Pt electrode.

5.2.3 Oxygen diffusion in oxidized steel

As a second example demonstrating the important role of lateral resolution for unveiling structural details, measurements on steel are presented. Model steel samples were first oxidized with oxygen of natural isotope distribution. In a second step, an ^{18}O tracer exchange experiment was performed in order to study the diffusion of oxygen in the oxidized grain boundaries. As tracer diffusion lengths of several μm were realized, samples were angle-polished in order to transform tracer depth profiles into lateral profiles. ToF-SIMS measurements were performed in CBA mode with Bi_3^{++} primary ions. An overview image of the ^{18}O secondary ion distribution of 50×50 μm^2 measured with 512×512 pixels and integrated over 200 images is shown in Fig. 39a. Detail images of 12×12 μm^2 were measured with 256×256 pixels and integrated over 300 images (Figs. 39b, c).

The visualization of diffusion paths along grain boundaries and the determination of the decrease of tracer concentration with depth are possible from the overview image. By applying the CBA mode in small areas and increasing the integration time, it was possible to resolve more details of grain boundary regions. An inhomogeneous ^{18}O distribution is discernible along grain boundaries (Fig. 39b) in some areas, even point-type ^{18}O enrichments become visible (Fig. 39c). It is found that triple junctions show a higher ^{18}O concentration than boundaries between 2 grains (Fig. 39b). These observations suggest that quasi 1D oxygen diffusion along triple junctions may play an important role also in integrated diffusion depth profiles. By investigating a cutting-plane, these filaments typically lead to point-type ^{18}O enrichments as discernible in Fig. 39c.

Modeling of such a system to extract diffusion coefficients is therefore very complex. The more important are highly resolved images to discern or even quantify these effects in detail. Only considering integrated depth profiles (as shown in Fig. 40) cannot provide these detailed information and misinterpretation of such depth profiles can be avoided.
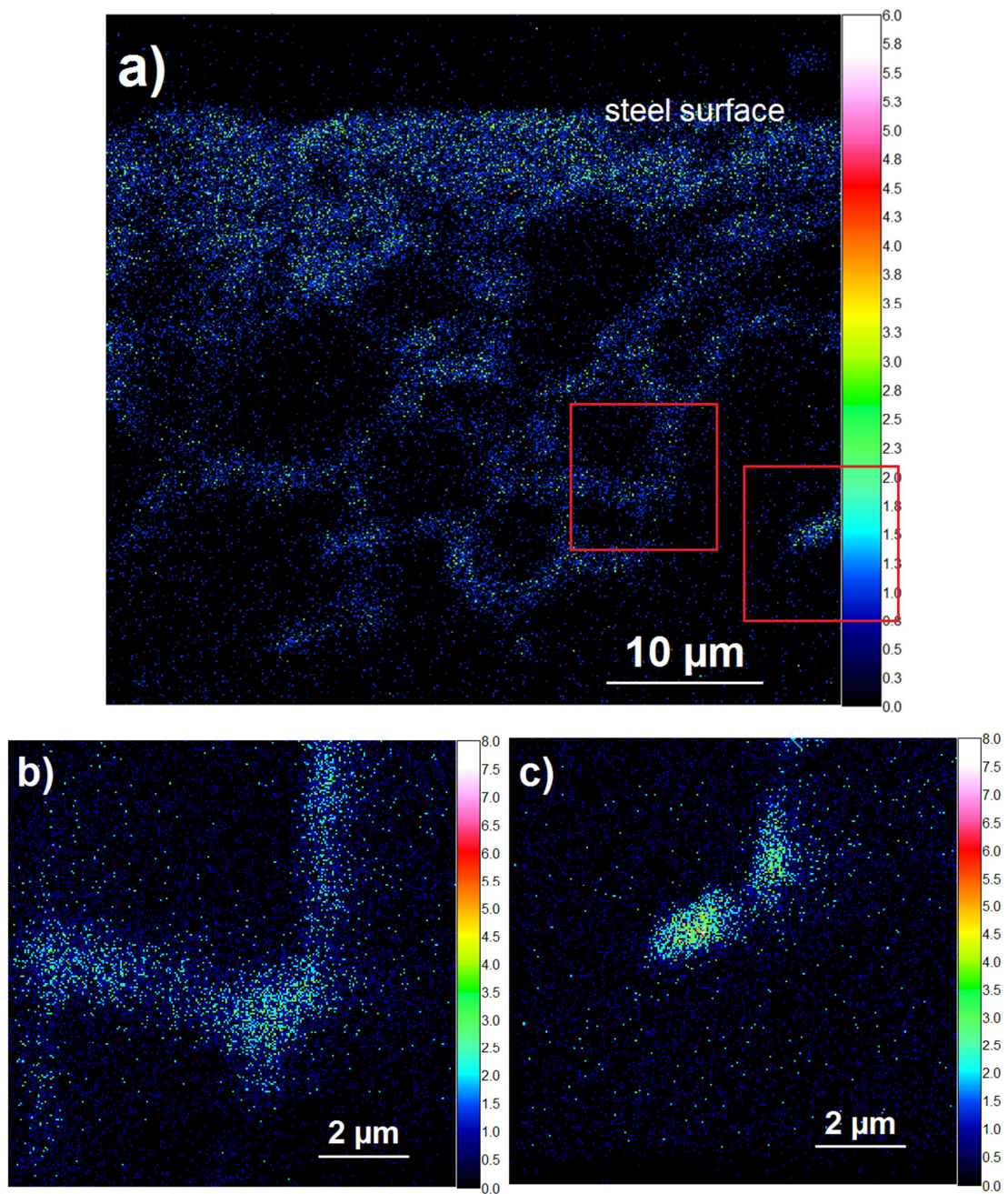
Figure 39: a) $^{18}O^-$ lateral map visualizing tracer diffusion in an angle polished, oxidized steel sample; b,c) $^{18}O^-$ detail images of the areas depicted in a).
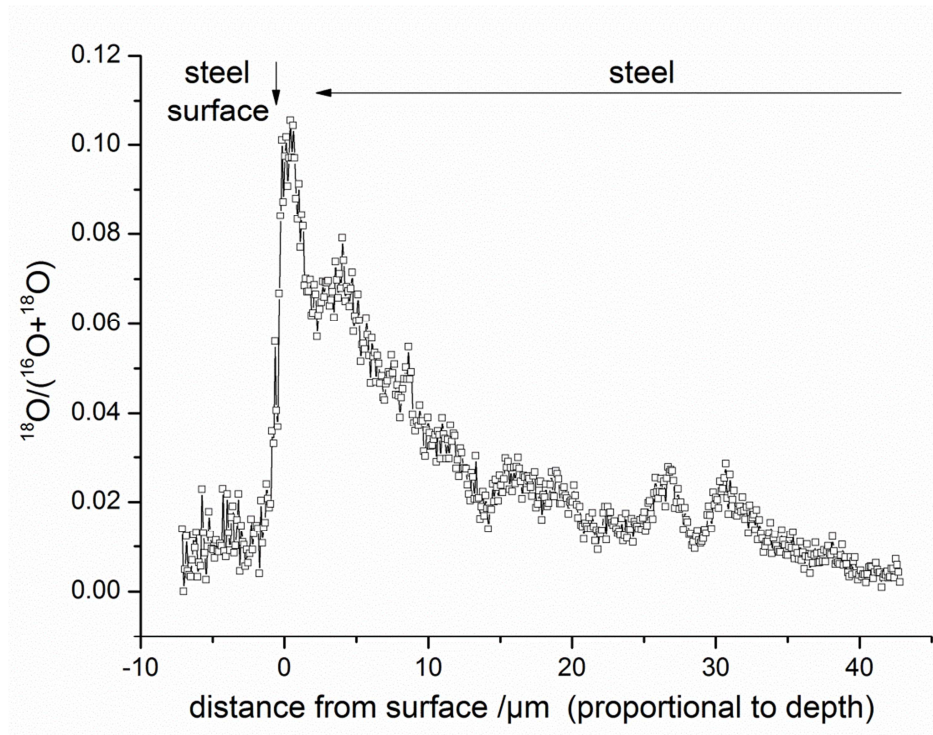
Figure 40: ^{18}O tracer depth profile extracted via line integration from the measurement also shown in Fig. 39a.

5.3 Mass resolution in CBA-burst mode

The corrosion of copper in humid environment is of great interest for electronics and semiconductor technology. Migration and diffusion processes of copper between differently charged electrodes are examined in this example under wet conditions and electric bias. Beside the well-known growth of copper dendrites from the cathode to the anode, different corrosion products of copper (e.g. copper salts, copper oxides) are partially spread over the surface [193] during the corrosion process. Secondary electron images of copper dendrites on silicon nitride (Fig. 41) demonstrate the higher lateral resolution obtainable with the CBA mode compared to the BA mode. Among the corrosion products are also sulfur-containing compounds. The majority isotope of sulfur ^{32}S, however, has a mass interference with $^{16}O_2$ which is often present in

significant intensities. Hence, both a high mass resolution and a high lateral resolution are required to get insight into these corrosion phenomena.
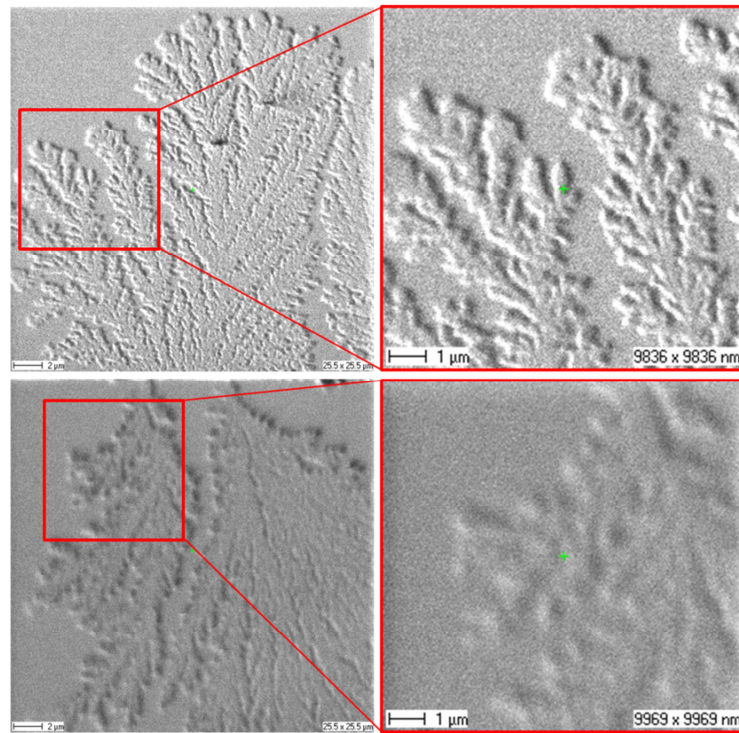
Figure 41: Measurements of copper dendrites on silicon nitride. Differences in image resolution achieved in CBA mode (top) and BA mode (bottom) are shown for secondary electron overview images (left) and detail images (right).

Typical ToF-SIMS imaging modes only have unit mass resolution and are thus unable to separate $^{16}O_2$ and ^{32}S. In BA and CBA mode it is possible to reach a higher mass resolution by operating them in burst mode. By chopping the primary ion beam to packages of ~1.5 ns in burst mode it is possible to reach mass resolutions $m/\Delta m$ higher than 6000. The major downside of the burst mode is the strong loss of intensity (ca. a factor 30). Intensity can be improved again by applying several consecutive bursts (shown for 8 bursts in Fig. 42) given that there are no mass interferences in the mass range claimed by the additional bursts. Fig. 42 also shows that the separation of

^{32}S$^-$ and ^{16}O$_2^-$, which requires a mass resolution of m/Δm > 1800, can be easily done in CBA burst mode.
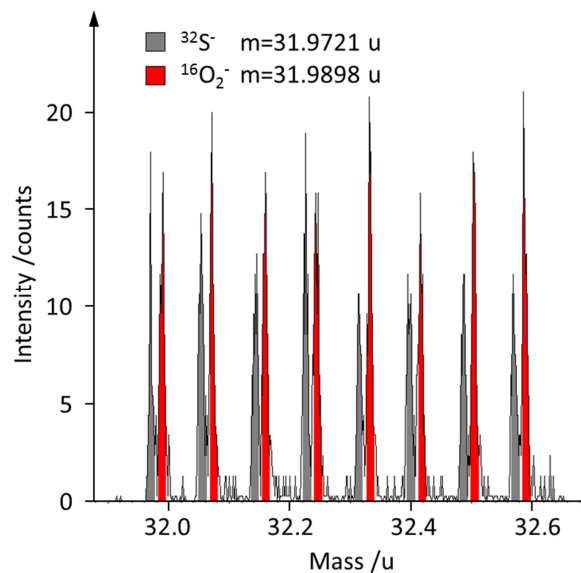
Figure 42: Mass spectra obtained in CBA burst mode with 8 bursts allowing the separation of ^{16}O$_2^-$ and ^{32}S$^-$. The mass scale is only valid for the first burst.

This mass separation makes imaging of the sulfur distribution possible. In Fig. 43a an overlay image of ^{16}O$^-$ (green) and ^{32}O$^-$ (red) is shown. While the oxygen image resembles the dendrite structures of copper, high intensities of sulfur are only found in several places. The images in Fig. 43 were created from a measurement in CBA mode of 85×85 µm^2 measured with 1024×1024 pixels and integrated over 25 images. Point-like sulfur enrichment is found at the tips of copper dendrites, while line-shaped enrichment is visible at both edges of the anodes. The distribution images of both mass 32 signals, ^{32}S$^-$ and ^{16}O$_2^-$ are displayed in Figs. 43b, c showing that the enrichment in the S-signal has no counterpart in the ^{16}O$_2^-$ distribution image and further verifying that mass separation was successful.
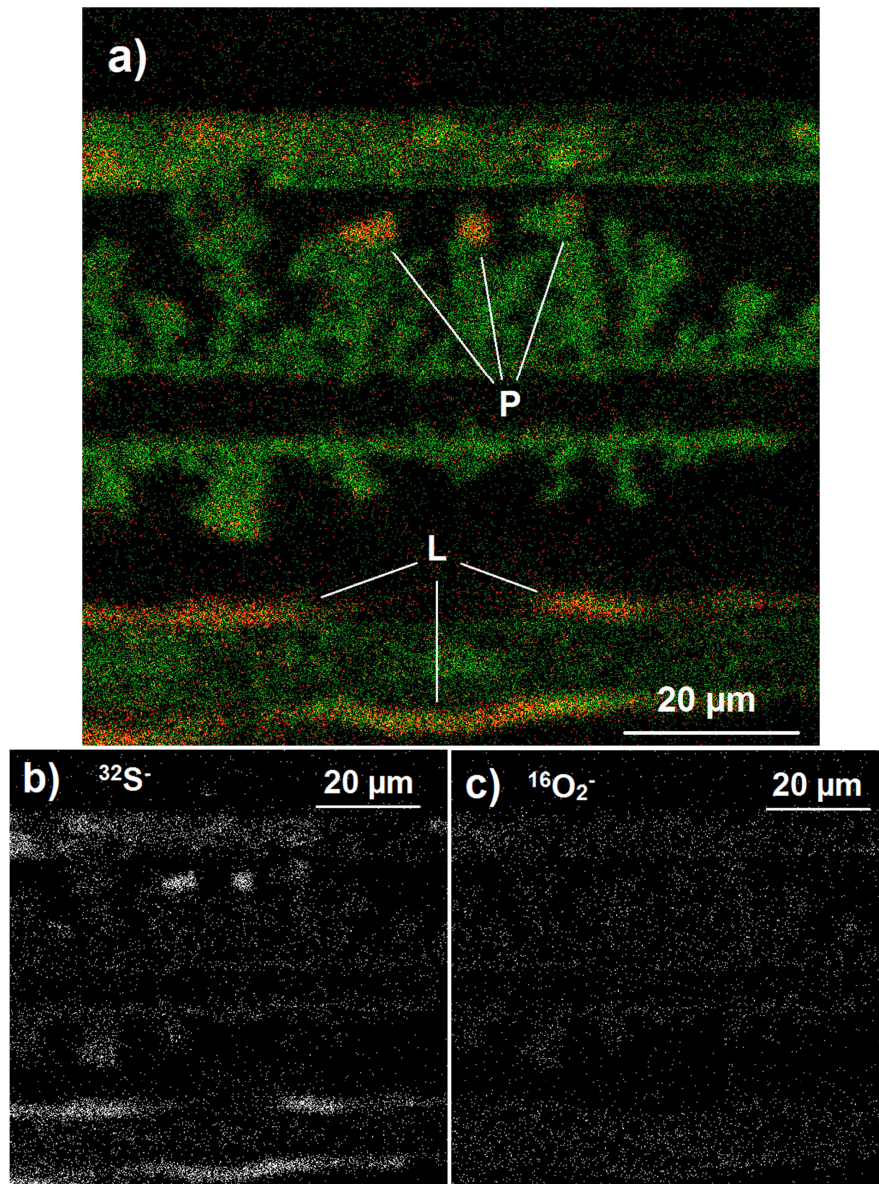
Figure 43: a) Overlay image of $^{16}O^-$ (green) and $^{32}S^-$ (red) showing point-shaped (P) and line-shaped (L) accumulation of sulfur; b) $^{32}S^-$ image of the same area separated in CBA-burst mode from the $^{16}O_2^-$ distribution image shown in c).

5.4 Accuracy of isotope fractions and its role in isotope exchange depth profiling

The accuracy of isotope fraction measurements is especially important for geologic samples, but it also plays a role for tracer diffusion experiments on functional oxides. Oxygen has three stable and naturally occurring isotopes, ^{16}O as majority isotope (~99.76%) and ^{17}O (~0.04%) and ^{18}O (~0.2%) as minority isotopes. The natural isotope distribution of oxygen varies slightly in water, atmosphere and lithosphere. The values for the natural isotope fraction $^{18}O/^{16}O$ most commonly used in literature are from National Institute of Standards and Technology (NIST) $2.05(14) \times 10^{-3}$ and the Vienna Standard Mean Ocean Water (VSMOW) definition of International Atomic Energy Agency, $^{18}O/^{16}O = 2.00520 \times 10^{-3}$. Typically in air, water and oxygen containing solids, oxygen isotope ratios within this range of variation are found. However, it should be noted that bottled oxygen, which is often used in preparation or annealing steps, usually does not have natural isotope distribution. Depending on preparation and purity, often significantly higher $^{18}O/^{16}O$ ratios up to 5×10^{-3} can be expected in bottled oxygen.[194]

5.4.1 Isotope exchange depth profiling on functional oxides

Isotope exchange depth profiling (IEDP) is a methodically simple approach. First, tracer depth profiles are established by tracer gas exchange at elevated temperatures, then the diffusion profiles are frozen-in at room temperature and measured e.g. with ToF-SIMS. When using oxygen tracer enriched gas, kinetic parameters such as the oxygen exchange coefficient k* and the tracer diffusion coefficient D* can be obtained. In a typical IEDP experiment oxygen exchange is investigated on a 200 nm thin film of $La_{0.6}Sr_{0.4}CoO_{3-\delta}$ (LSC), a mixed ionic and electronic conductor, on 500 μm yttria stabilized zirconia (YSZ, 9.5 mol% Y_2O_3). Thermal oxygen exchange was performed for 5 min in 200 mbar $^{18}O_2$ (97.1% enriched) at 376˚C. The depth of the film was

determined from sputter coefficients based on reference measurements analyzed by digital holography microscopy.

SIMS measurements were then performed in three different modes with Bi^+: in CBA mode, in BA-burst mode with integration as described by DeSouza et. al.,[195] and in BA mode. Different isotope fraction profiles are determined by these 3 methods as shown in Fig. 44 and reproduced in two measurements each. Parameters affecting the correct determination of oxygen tracer fractions are discussed in literature.[169, 196, 197] Essentially, the reason for the differences here can be found in the high $^{16}O^-$ secondary ion intensity in BA mode. Although Poisson correction is applied for all measurements, in BA mode $^{16}O^-$ counting by the detector is falsely too low (see also Ref.[176]). This is a result of saturation effects that are not sufficiently correctable by Poisson statistics and of interaction of secondary ions. Mass spectra $^{16}O^-$ measured in BA and CBA mode are shown in Fig. 45. Because of the wrong counting of $^{16}O^-$ and the correct counting of $^{18}O^-$, a too high ^{18}O tracer fraction is measured in BA mode. For the measurements in CBA mode, both isotopes intensities are within the linear counting regime of the detector, thus correct values of the isotope fractions can be expected.

In order to extract the parameters k* and D*, the profile was then modeled as 1D-diffusion problem in COMSOL Multiphysics 4.0 software with 2 fit parameters: (i) the surface exchange coefficient k* of LSC and (ii) the diffusion coefficient D* of LSC. The slope of the profile in YSZ is too small to allow determination of a reasonably accurate diffusion coefficient of YSZ. Therefore the diffusion coefficient of YSZ was taken from electrical reference measurements on YSZ single crystals at 376°C ($1.3 \cdot 10^{-10}$ cm^2/s) and not further varied. This value also corresponds well to data reported in literature [198]. Fitting functions agree very well with all measured data in CBA and BA-burst mode. The sharp edge at the LSC|YSZ interface simply reflects the step in diffusion coefficient, which is much larger in YSZ. Values of k* and D* are shown in Fig. 44 for the respective depth profiles.
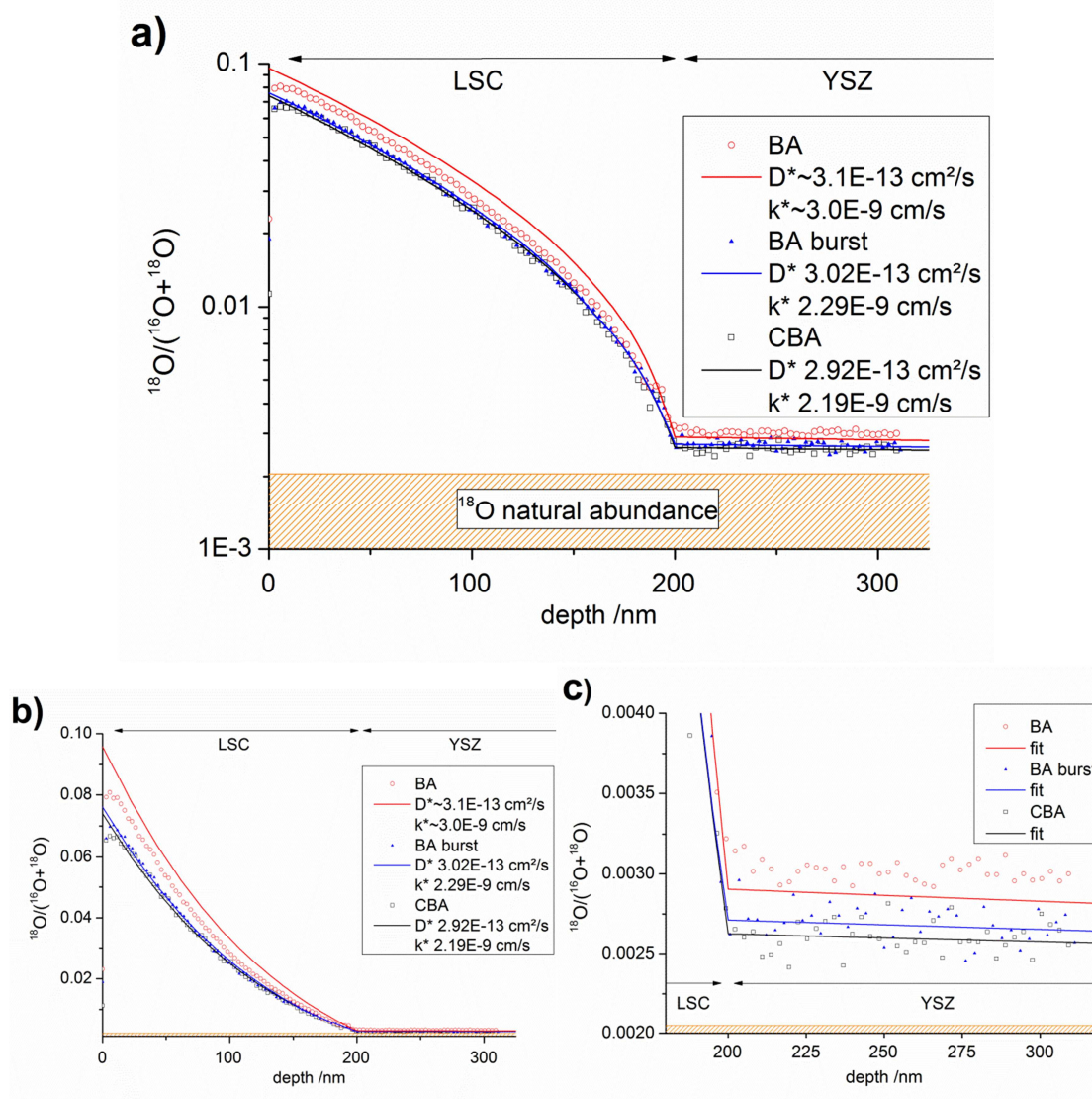
Figure 44: ^{18}O isotopic fraction in (a) logarithmic and (b) linear plot. c) Magnification of (b) showing the different ^{18}O fractions in YSZ.

For this example, the values of $k^* = 2.19 \cdot 10^{-9}$ cm/s and $D^* = 2.92 \cdot 10^{-13}$ cm²/s can be extracted from the CBA measurement. Measurement in BA-burst mode yield only slightly higher values of $k^* = 2.29 \cdot 10^{-9}$ cm/s and $D^* = 3.02 \cdot 10^{-13}$ cm²/s. For the same depth profile measured in BA-mode, the quality of the fit is considerably lower. This indicates that the changes of the deduced isotope fractions lead to a non-physical

diffusion profile. In contrast to the profiles obtained with the other measurement modes, the front-part (LSC) of the diffusion profile or the back-part (YSZ) cannot be reproduced with one and the same data set of D* and k*.

Using a fit curve which overestimates the tracer fraction in LSC and underestimates the fraction in YSZ yields k* = $3.0 \cdot 10^{-9}$ cm/s and D* = $3.1 \cdot 10^{-13}$ cm^2/s, and thus a significantly higher k* value which is a result of an erroneous isotope fraction measurement.
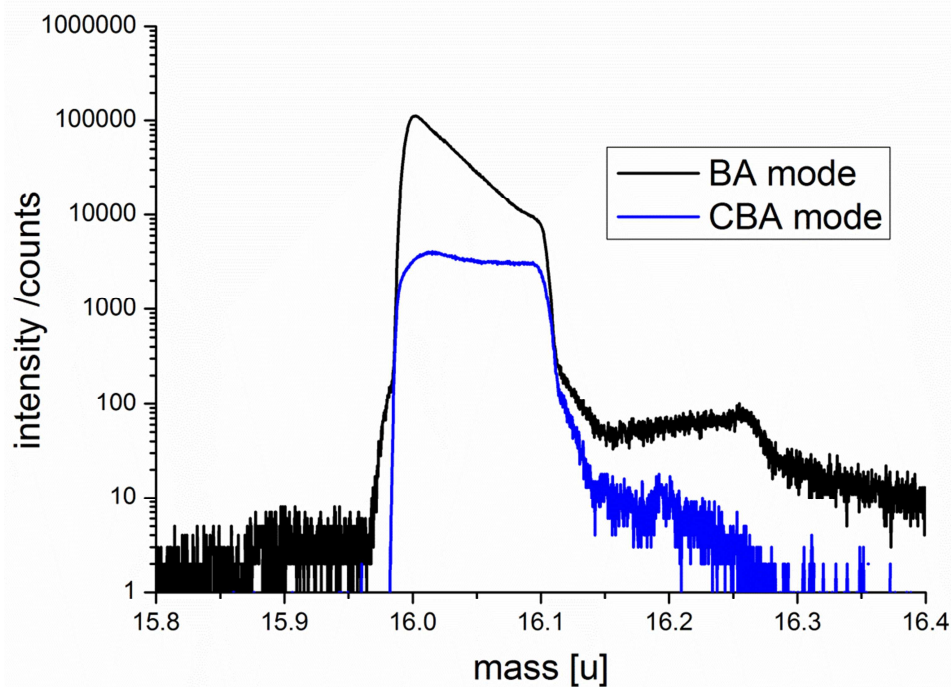
Figure 45: Mass spectra of the $^{16}O^{-}$ signal measured with ~50 ns pulse width in BA and CBA mode. In BA mode, detector saturation effects as well as intensity preceding and succeeding the main signal as result of ion interactions are visible.

The correct determination of isotope fractions can therefore only be performed in a certain intensity window of secondary ions, which depends on many parameters (isotopes analyzed, detection system, secondary ion yield, etc.). The CBA mode offers

the possibility to adjust the primary ion beam current such that the secondary ion intensity is inside this window thus avoiding systematic errors resulting from either too high or too low secondary ion intensity.

5.5 Conclusions

The novel CBA operation mode for ToF-SIMS measurements exhibits excellent performance and was successfully applied to several scientifically relevant examples in materials research. By adapting the beam guidance from burst alignment mode, it is possible to achieve lateral resolutions below 100 nm at higher currents than in other imaging modes. Besides application as imaging mode, the CBA mode offers the possibility to adjust the primary ion beam currents over a wide range, making it ideal for isotope analysis. The higher lateral resolution of the CBA mode helped unveiling important details of electrochemically active zones of Pt|YSZ and fast diffusion paths in oxidized steel. Stepless adjustment of the beam currents can avoid detection non-linearity effects and allows measurement of correct isotope fractions. Measuring in CBA mode offers also the possibility to achieve both high lateral and a high mass resolution. This enabled detection of sulfur species on Cu dendrites despite the presence of $^{16}O_2$ signal. Accurate isotope fraction determination in CBA mode was demonstrated to be important when analyzing diffusion coefficients and oxygen exchange coefficients, for example of LSC thin films on YSZ. It was also shown that it is possible to remain within the boundaries of static SIMS when measuring with CBA mode.

6 Investigations of La$_{0.6}$Sr$_{0.4}$CoO$_{3-\delta}$ Thin Films by Complementary Impedance Spectroscopy and Isotope Exchange Depth Profiling

6.1 Introduction

Several analytical methods exist to investigate the catalytic activity towards the ORR of mixed ionic and electronic conducting electrodes. Two different approaches were employed in this study, electrical impedance spectroscopy and ^{18}O isotope exchange depth profiling. EIS was already described in Sec. 2 and it is a powerful tool to investigate the electrical and electrochemical properties of MIEC electrodes on ionic conducting substrates. From resistive and capacitive contributions, many parameters such as the catalytic activity of surfaces, oxygen non-stoichiometry, diffusion parameters and conductivities, transport reactions across solid|solid phase boundaries, or the formation of impurity phases can be indirectly probed. However, the correct interpretation of impedance spectra is crucial for the validity of the extracted parameters. The interpretation can be trivial for simple cases but in complex systems it is often very difficult and far from being unambiguous. Oxygen isotope exchange and subsequent depth profiling (as also described in Sec. 4) has the simpler methodology, in terms of interpretation even though the experiment itself is more elaborate. Here, the properties of oxygen exchange are probed by providing isotopic tracer via the gas phase and establishing a depth profile in a sample. From this depth profile, ion exchange and diffusion related parameters can be extracted.

While impedance spectroscopy is a quite common method to investigate thin films,[31, 48, 199, 200] oxygen tracer experiments are mostly performed on bulk samples.[122, 175, 201] To the best of the author's knowledge no study so far reported experiments with both techniques being applied on the same films. A first attempt was made here and results are reported in the following. As electrical measurements require an oxygen ion conductor, YSZ was used as substrate for the MIEC La$_{0.6}$Sr$_{0.4}$CoO$_{3-\delta}$ thin films which

were investigated. LSC films with two different microstructures (LSC-LT and LSC-HT) as described in the preceding chapters were analyzed.

6.2 Experimental

Dense $La_{0.6}Sr_{0.4}CoO_{3-\delta}$ thin films with 200 nm thickness were deposited on $10 \times 10 \times 0.5$ mm³ YSZ (100) single crystals by using the following PLD parameters: 7.0 cm target-substrate distance, 0.04 mbar O_2, 400 mJ laser energy at 10 Hz pulse frequency, 27 min deposition time, 12 K/min cooling. Two different deposition temperatures measured with a pyrometer (Heitronics KT-19.99) were used to prepare the samples denoted LSC-LT (450°C) and LSC-HT (650°C). LSC thin films were then microstructured by photolithography. Thus, circular microelectrodes with 200 μm diameter were prepared. Oxygen isotope exchange experiments were performed by heating to 400°C in air (12 K/min), then switching to 200 mbar 97.1% ^{18}O isotope enriched oxygen (Campro Scientific) for 5 min and then cooling to room temperature with 60 K/min to freeze the tracer diffusion profile. The isotope diffusion profiles were subsequently measured by depth profiling with ToF-SIMS (TOF.SIMS 5, ION-TOF). 25 kV Bi^+ primary ions were used in the novel CBA mode described in Sec. 5. Negative secondary ions were analyzed in areas of 100×100 μm² using a raster of 512×512 measured points. For depth-profiling, 2 kV Cs^+ ions (500×500 μm², ca. 105 nA) were used for sequential ablation of the surface between measuring mass spectra. For charge compensation, a low energy electron flood gun (10 V) was employed. Following the SIMS measurements, the same samples (though different microelectrodes) were investigated by electrochemical impedance spectroscopy similar to the investigations in Sec. 2.2.1. Here, 200 μm microelectrodes were contacted by gold covered steel needles (EGON 0.4, Pierenkemper) and measured with an Alpha-A high performance frequency analyzer (Novocontrol, Germany) versus a macroscopic LSC counter electrode at 400°C in air. AC frequencies of 1 MHz to 0.08 Hz with 10 mV effective amplitude were applied to measure impedance spectra.

6.3 Results

In Fig. 46 impedance spectra are shown, measured on circular 200 μm microelectrodes of the differently prepared LSC thin films. Several features are visible in both spectra. At the highest frequencies a part of a semicircle is visible. This semicircle can be attributed to the spreading resistance of YSZ underneath the microelectrode. This resistance depends on the size of the microelectrode and is inversely proportional to the ionic conductivity of YSZ. From this relation and reference measurements of the temperature dependence of the YSZ conductivity it is possible to calculate an average temperature of the microelectrode.[199] Here the set temperature of the furnace was chosen such that the YSZ spreading resistance was equivalent to a temperature of $400 \pm 1\,°$C.

At lower frequencies the impedance contributions of the electrode become visible. A Warburg-like shape of the electrode contribution with almost a 45° straight line at medium frequencies, followed by a semicircle-like part at low frequencies is found. Even if these general features are similar for LSC-LT and LSC-HT several differences can be observed between their impedance spectra. Most obvious, the total electrode resistance is smaller for LSC-LT. Differences of the shape are also visible in the intermediate frequency part shown in the inset in Fig. 46. LSC-HT approaches the 45° range from larger phase angles (semicircle like) while LSC-LT exhibits a very flat spectrum part above ca. 100 Hz. Impedance contributions in this frequency range are often attributed to the electrode|electrolyte interface.[48]
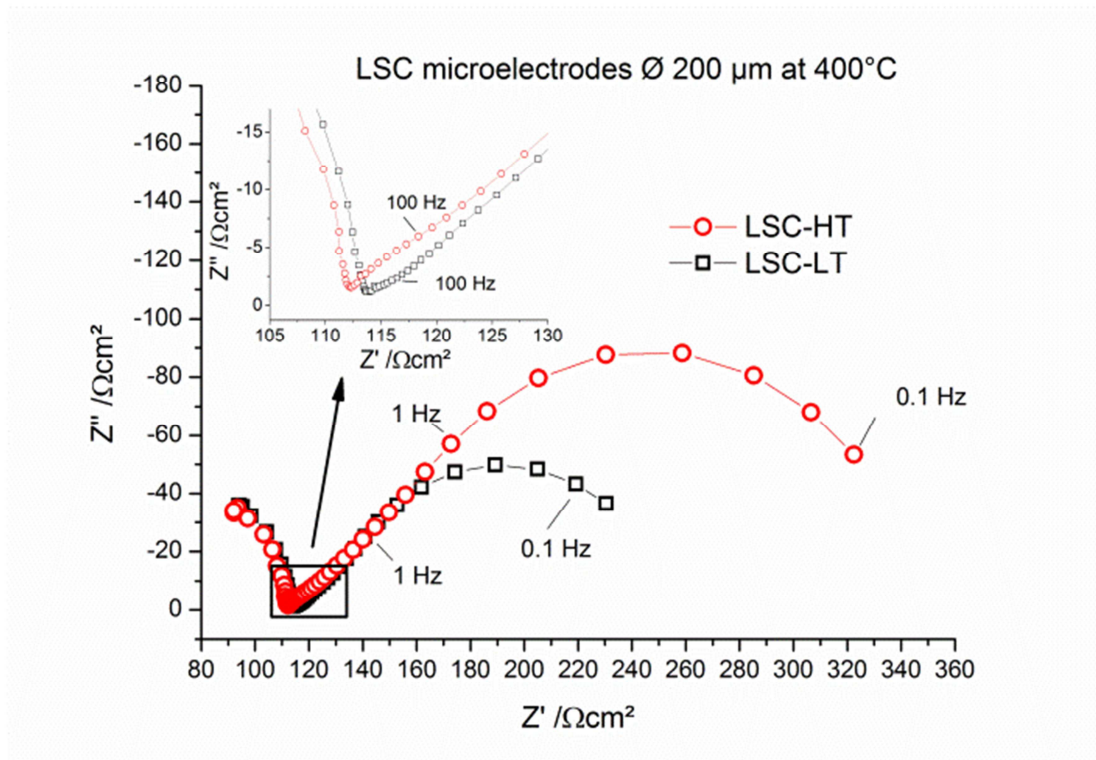
Figure 46: Nyquist plot for EIS measurements on LSC microelectrodes on YSZ. LSC-LT has the lower total electrode resistance. The medium frequency part exhibiting differences between the two spectra is shown as inset.

In Fig. 47 the oxygen isotope depth profiles measured by ToF-SIMS on the same samples after annealing in ^{18}O enriched atmosphere at 400°C for 5 min are shown. The isotope fractions c are calculated as in Sec. 4.2.2 in Eq. 11. Both depth profiles show a surface isotope fraction of about 10% followed by a drop in concentration in the LSC thin film which can be attributed to the limited ionic conductivity of LSC. Then, at 200 nm depth, a transition to a very flat profile in YSZ follows which reflects the high ionic conductivity there. Several differences can be observed between the profiles. First, the total amount of incorporated ^{18}O is higher in LSC-LT. In a rough approximation the total amount of exchanged isotope is related to the tracer surface exchange coefficient k* of LSC. The differences in the decay of tracer fraction in LSC reflect differences in the tracer diffusion coefficient D*. The general tendency of LSC-

LT having the lower polarization resistance in EIS and showing the higher exchange rate of tracer is matching well, but for an exact determination and comparison of oxygen transport parameters and resistance contributions, fitting methods are necessary to analyze both sets of data.
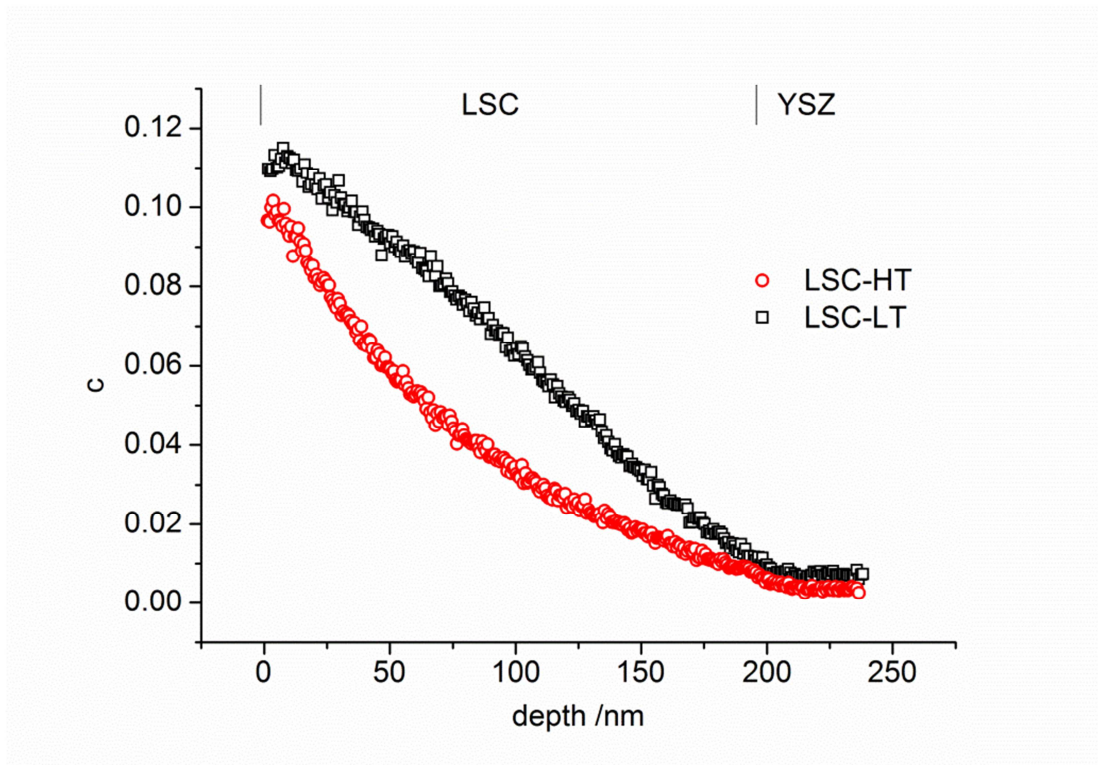
Figure 47: Oxygen isotope depth profiles measured on the same samples as in Fig. 46. A different amount of ^{18}O incorporated into YSZ, a different bending of the ^{18}O concentration curves of LSC-LT and LSC-HT, and a different drop at the interface are discernible.

6.4 Data analysis

6.4.1 Impedance spectroscopy

Generalized equivalent circuits for mass and charge transport in differently conducting systems are extensively discussed by Jamnik and Maier.[49] The equivalent circuits shown in Fig. 48a,b are slightly adapted from Ref.[49] They correspond to the complete model of a mixed conducing electrode with surface related resistance R_s, ionic transport resistance R_{diff} (here a sum of 50 equivalent resistances R_{TL} in a transmission line) and interfacial resistance R_{if} (cf. Fig. 48b). A reduced model for surface controlled oxygen exchange and negligible R_{diff} is shown in Fig. 48a. In the models in Fig. 48, C_s, C_{if} and $C_{diff} = 50\ C_{TL}$ denote the capacities of surface, interface, and the chemical bulk capacitance (in a transmission line), respectively. Q is a constant phase element with the impedance:

$$ Z_Q = \frac{1}{(i\omega)^n P} . \tag{23} $$

For $n = 1$, Q is equivalent to a capacitor with capacitance P. By using Q instead of C in RC elements (sometimes called "Cole Element") it is possible to model depressed semicircles, which are regularly observed due to non-idealities in samples.

The model shown in Fig. 48c is an incomplete equivalent circuit which was used to fit only the low frequency part of the impedance spectra. For this model, the spreading resistance of the electrolyte R_{YSZ} was determined beforehand and fixed. Then only low frequency points, i.e. the main part of the large semicircle, were used for fitting (LSC-HT: 8 Points 1-0.1 Hz, LSC-LT: 7 Points 0.6-0.07 Hz. This arc was attributed to the electrode surface reaction, and the additional resistance value includes all other contributions to the total electrode resistance (e.g. R_{if}, R_{diff}).
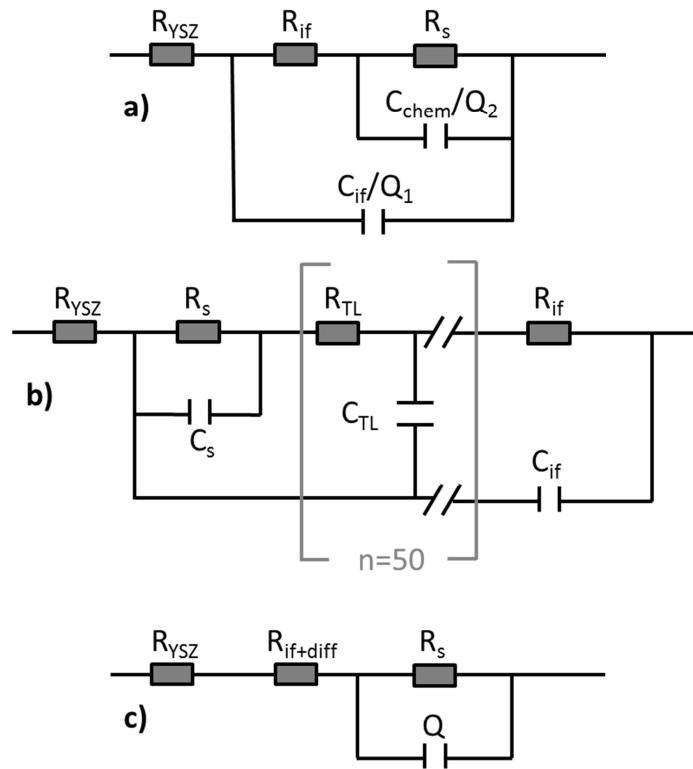
Figure 48: Equivalent circuits used for fitting of impedance spectra. The circuits shown in (a) and (b) are adapted from circuits derives in Ref.[49] with $R_{diff} = 50R_{TL}$ and $C_{chem} = 50C_{TL}$. The incomplete equivalent circuit shown in (c) was used to fit only the low frequency impedance using a beforehand determined and fixed value of R_{YSZ}.

The results of fitting the impedance spectra with these different equivalent circuits are shown in Figs. 49a,b,c. The fits using the reduced circuit (Fig. 48a) could often be applied in literature[34] to quantify spectra of similar electrode materials at higher temperature.
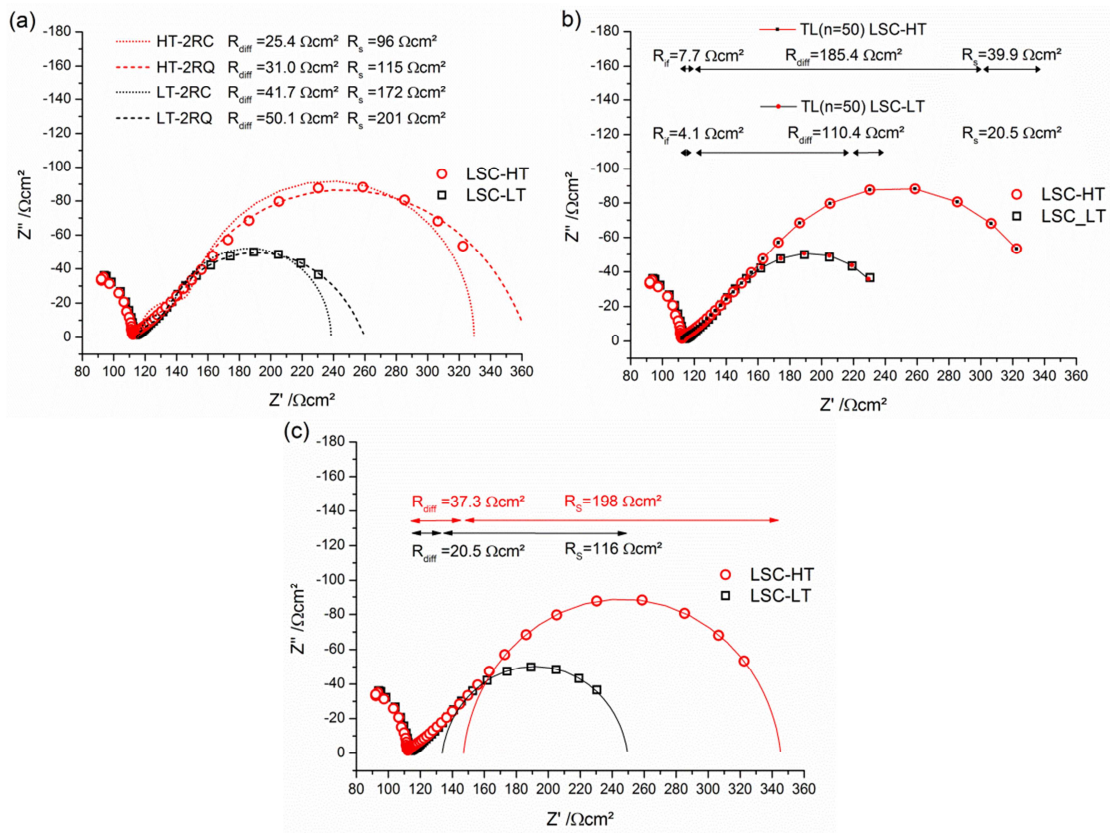
Figure 49: Fitting curves for the impedance spectra generated with the different equivalent circuits. For the fits in (a),(b),(c) the corresponding models in Figs. 48a,b,c were used.

Here, however, the corresponding model is not suited well to fit the impedance spectra. The fits give a larger resistance for the electrode surface and a small resistance for the LSC|YSZ interface, but neither the high frequency part nor the low frequency part are well reproduced. As in this model the oxygen diffusion resistance in LSC is neglected, the failure to reproduce the spectra gives evidence that diffusion (indicated by the 45° angle) may indeed contribute significantly to the total electrode resistance. Fitting with the equivalent circuit in Fig. 48b, which includes diffusion in a transmission line of 50 identical elements, reproduces the measured points from the impedance spectra very well (cf. Fig. 49b). The fitting parameters of this model suggest a very small interface resistance, and a small surface resistance. The major part of the electrode resistance is there explained by the resistances in the transmission line which

model the ionic conductivity of LSC. This distribution of resistances would suggest that the overall oxygen reduction kinetics in these LSC films is limited by bulk diffusion. By using the fitting model with only one RQ element in Fig. 48c, the low frequency part of the impedance spectrum is also well reproduced with a single slightly compressed semicircle (n~0.96). Assigning this resistance to the electrode surface leaves only a minor part of the total electrode resistance to the contributions of diffusion and the LSC|YSZ interface. In this model, the surface exchange of oxygen would be rate limiting, a contrary interpretation than derived from the fit in Fig. 49b. This discussion reveals that an unambiguous conclusion of the rate limiting step is hardly possible based on these impedance data alone.

6.4.2 Isotope exchange depth profiling

Two different models were used to analyze the oxygen isotope depth profiles in Fig. 47 with COMSOL finite elements software. The simpler model consists of three parameters, k^*, D^*_{LSC} and D^*_{YSZ}. The value of D^*_{YSZ} was fixed at 2×10^{-10} cm^2/s in accordance with literature data[198] and only k^* and D^*_{LSC} were varied to fit the measured depth profiles. This model could not exactly reproduce the experimental results (see Figs. 50a,b). Particularly the profile in LSC-HT shows pronounced deviations from the fit result. Spatially varying diffusion coefficients in LSC were therefore allowed in a second model. For LSC-HT this included three larger zones in LSC and a short zone (10 nm) directly at the LSC|YSZ interface. The LSC-LT films were analyzed in terms of two zones of different D^* without an interface region due to absence of a sharp drop there (cf. Fig. 47). The latter represented an interface resistance. With this second model more exact fits of the isotope depth profiles were achieved and parameters for surface exchange and diffusion could be extracted, see Figs. 50c,d.

From the fit parameters it is possible to calculate resistive contributions [48, 103, 202] In Eq. 24, this is exemplarily shown for the surface exchange coefficient.

$$k^q = \frac{k_B T}{4e^2 R_s c_0} \qquad (24)$$

Here, k^q is the electrical surface exchange coefficient, k_B is Boltzmann's constant, T the temperature e the elementary charge and c_0 the total concentration of lattice oxygen (0.088 mol/cm^3 from x-ray diffraction data of $La_{0.6}Sr_{0.4}CoO_{3-\delta}$[80] and $\delta \sim 0.03$). An analogous calculation is possible for the diffusion parameters using $\frac{D^q}{thickness}$ instead of k^q. As for this calculation the electrical parameters k^q and D^q are relevant, and in the isotope exchange experiment only the tracer parameters k* and D* can be determined, a correction factor is necessary to consider their different values[103] (Eq. 25). For the diffusion coefficients this factor is the Haven ratio H, we therefore obtain

$$D^q \cdot H = D* \qquad (25)$$

And in perovskite-type oxides a typical value of H = 0.69 can be expected[131] which was used in this work. This Haven ratio, however, is only defined for diffusion. As for the surface exchange likewise a difference between k^q and k* can be expected, as first approximation the same ratio was used according to

$$k^q \cdot H = k*. \qquad (26)$$
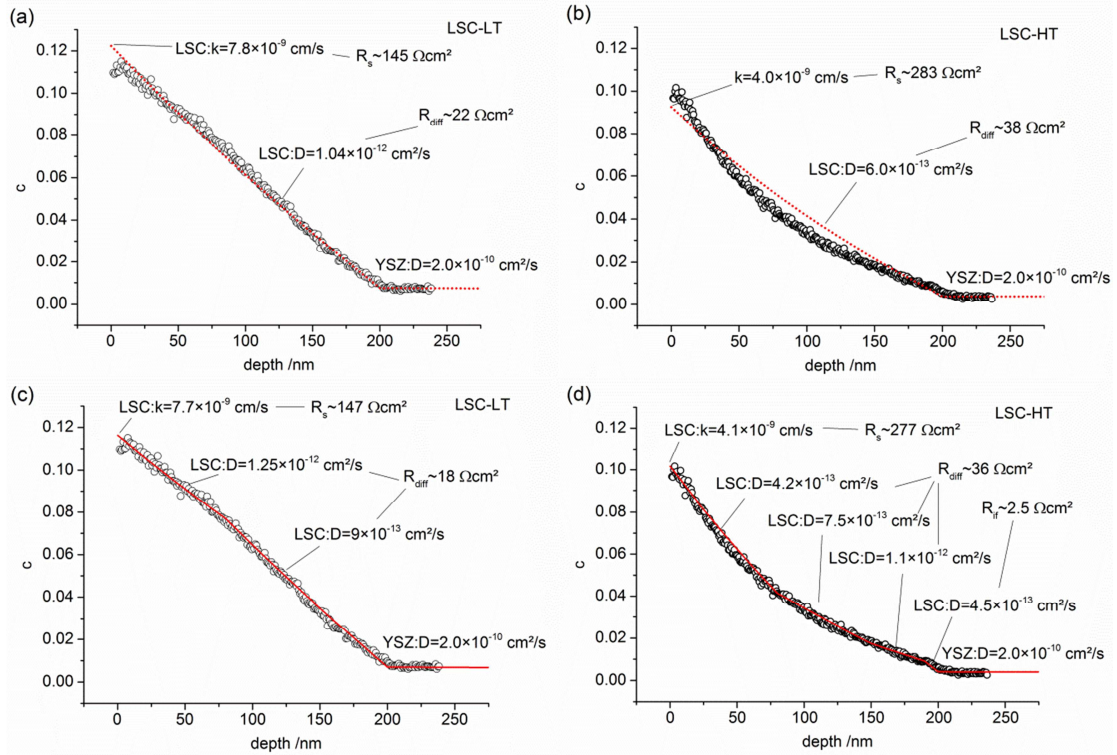
Figure 50: Fitting curves for the tracer depth profiles using only one diffusion coefficient for LSC (a,b) and using variable diffusion coefficients (c,d) for LSC-LT (a,c) and LSC-HT (b,d). Calculated individual resistance contributions are also shown.

Even though the quality of the fit is better using different diffusion coefficients, the extracted values of the resistive contributions are very similar for the two models. In both LSC thin films the largest resistive contribution could be attributed to the electrode surface (~ 150 Ωcm² and ~ 280 Ωcm² for LSC-LT and LSC-HT, respectively) which is also in accordance with literature results for LSC investigated by impedance spectroscopy at higher temperatures.[34] Transforming the interfacial concentration drop in LSC-HT into an LSC|YSZ interface resistance shows that this is only a very small contribution to the total electrode resistance (~ 2.5 Ωcm²). Larger than this interface resistance, but still smaller than the dominating surface resistance, is the ionic diffusion resistance of LSC. Interestingly, significant changes of the diffusion coefficient with depth were found for LSC-HT. Here, closer to the interface almost a

factor of 3 faster diffusion than close to the surface was observed. For LSC-LT only slight inhomogeneities of the diffusion coefficient were obtained, and here diffusion was faster closer to the surface. The reasons for these inhomogeneities as well as for the differences between the LSC-LT and LSC-HT films are yet unclear. A comparison of the k* and D* values for these films with the epitaxially grown but strained films of the same composition (Sec. 4.2.8) is only possible to a limited extent. There, lower temperatures of 375°C were used and diffusion coefficients above 1×10^{-13} could not be determined. When extrapolating it seems that a better match to the more active tensile strained films is achieved, however the higher surface roughness or grain boundaries in these films on YSZ can be a reason for apparently higher catalytic activity.

6.5 Comparison of the extracted parameters from EIS and IEDP

In the following tables the resistive parameters extracted with the different measurement and fitting methods are compared for LSC-LT (Tab. 1) and LSC-HT (Tab. 2).

Table 6: Resistive contributions of the LSC-LT thin film electrodes extracted from EIS and IEDP measurements. Model a-c correspond to models shown in Fig. 48, C, Q indicate whether capacitances or constant phase elements were used. ^{18}O 1D* and ^{18}O var. D* corresponds to the fits of tracer depth profiles using a single or variable diffusion coefficients in LSC. $R_{LSCtotal}$ is the sum of all resistances attributed to LSC.

LSC-LT	R_{if} /Ωcm^2	R_{diff} /Ωcm^2	R_s /Ωcm^2	$R_{LSCtotal}$ /Ωcm^2	$R_s/(R_{if} + R_{diff})$
Model a (C)	25.4	-	96.7	122	3.8
Model a (Q)	31.0	-	114.6	146	3.7
Model b	4.1	110.4	20.5	135	0.18
Model c	-	20.5	116	137	5.7
^{18}O 1D*	-	23	142	165	6.2
^{18}O var. D*	-	18	147	165	8.2

Table 7: Resistive contributions of the LSC-LT thin film electrodes extracted from EIS and IEDP measurements with analogous abbreviation as in Tab. 1.

LSC-HT	R_{if} /Ωcm^2	R_{diff} /Ωcm^2	R_s /Ωcm^2	$R_{LSCtotal}$ /Ωcm^2	$R_s/(R_{if} + R_{diff})$
Model a (C)	41.7	-	172	214	4.1
Model a (Q)	50.1	-	201	251	4.0
Model b	7.7	185.4	39.9	233	0.21
Model c	-	37.3	198	235	5.3
^{18}O 1D*	-	38	283	321	7.4
^{18}O var. D*	2.5	36	277	316	7.2

When comparing the total electrode resistance $R_{LSCtotal}$ a systematic difference can be noted between the values from impedance measurements and isotope exchange, showing higher resistance values in the tracer studies. The difference of about 30% can have several causes. Besides possible changes of the sample between SIMS and EIS measurements, the correction with the Haven ratio of 0.69 - especially for k - can be a reason for discrepancies between the resistances obtained by the different methods. Another possible source for a systematic deviation is the temperature. In microelectrode measurements a temperature gradient in the sample is caused by the contact tip. Even if the temperature is corrected by the YSZ spreading resistance a temperature distribution over the electrode area is present that can affect the effective electrode temperature. For typical temperature dependencies of LSC electrode resistances (E_a 1.3-1.6 eV [34, 122]) a 30% change of the total resistance is already caused by a temperature difference of below 10°C. Accordingly, the still rather similar resistance values obtained by the two techniques are regarded as indication that indeed both methods probe the same electrochemical processes and are appropriate for analyzing the oxygen reduction kinetics of mixed conducting electrodes.

Fit results of the impedance data show that the total resistances of the EIS models with the full transmission line (Fig. 49b) and with only one RQ element (Fig. 49c) are matching well, but the distribution of the resistances to the individual processes is very different. Comparing this to the data extracted from ^{18}O experiments we find the simple model c fitting only one semicircle for the surface resistance is matching much better. This becomes obvious from the ratio of the surface resistance to the other electrode resistances shown in the last row of Tabs. 1,2. Here model c (Fig. 48c) yields values of 5-6 matching best to the values of 6-8 found in tracer experiments. The model including the full transmission line, which gives the best fit to impedance spectra, finds completely different ratios of about 0.2 here. One might get the impression that the model with the transmission line is simply over-parameterized and it should be possible to shift the predominant resistance from R_{diff} to R_s and still get a good fit. This assumption was investigated by fixing the surface resistance to higher values up to the resistance found by model c. However, in these cases the quality of the fit was much lower, and performing a linear least square fit with such starting parameters again yielded the fit with dominating R_{diff}.

From this comparison it is concluded that the more semicircle-like intermediate frequency part of LSC-HT can now be attributed to the interfacial resistance R_{if} and finds its counterpart in the concentration step of the tracer profile. Moreover this means that the apparently exact model b fails to correctly analyze the impedance data. It should be kept in mind, however, that the "exact" model b still assumes spatially homogeneous R_{TL} values (constant ionic conductivity) and the curves of the tracer diffusion experiments strongly suggest that this is not fulfilled here. Further also the chemical capacitance could accordingly vary with depth. This might cause an inaccurate use of the fit parameters in model b to minimize the error during the fitting routine and thus could explain the wrong materials parameters. Accordingly it can lead to a misinterpretation of the spectra when only relying on impedance data. Combining two independent and complementary measurement methods in order to investigate the oxygen reduction kinetics of mixed conducting electrodes is clearly advantageous.

6.6 Conclusions

Impedance spectroscopy and isotope exchange depth profiling were used to investigate the oxygen exchange and transport properties of LSC thin film electrodes on YSZ single crystals. Two types of LSC thin films LSC-LT and LSC-HT, prepared at different temperatures were considered. The same films were consecutively analyzed by the two methods yielding complementary information. Impedance spectroscopy revealed that LSC-LT has the lower polarization resistance. Both LSC films showed a Warburg-like impedance but several slight differences could be observed. The choice of the correct equivalent circuit for fitting of the spectra proved to be intricate. Three different models were used yielding fits with different quality and also with very different extracted surface and diffusion resistances. The model which was best suited to reproduce the impedance spectra suggested oxygen diffusion to be rate limiting, while other models suggested the surface exchange to cause the major part of the electrode resistance. In oxygen tracer experiments, it could be shown that indeed the oxygen exchange at the surface is rate limiting. Further a comparison of the resistances of the electrode surface, of diffusion in the electrode and of oxygen transport through the

LSC|YSZ interface extracted by the different methods was performed. Even though a systematic deviation of the calculated total electrode resistance of about 30% was observed between the two methods, the relative differences between LSC-LT and LSC-HT were well reproduced. Further, by this comparison the best suited model for impedance analysis could be identified. Also the small impedance contribution of the LSC|YSZ interface resistance found for LSC-HT and not for LSC-LT in tracer experiments is well matching to differences in the impedance response between LSC-LT and LSC-HT in the intermediate frequency range. Interestingly, inhomogeneities of the diffusion coefficient in LSC with depth were found. These inhomogeneities together with possible inhomogeneities of the chemical capacitance can be the reason for the large differences of resistance distributions in the different impedance models.

7 Summary

Dense LSC thin films of different composition were successfully prepared by PLD on (100) single crystalline YSZ electrolyte. Two different microstructures of LSC with different grain sizes were obtained by variation of the substrate temperature during the deposition process. For electrochemical characterization, microelectrodes were fabricated from LSC thin films by photolithography. The polarization resistance of the ORR was measured by impedance spectroscopy. By this technique it was possible to differentiate between contributions of the total electrode resistance from the LSC surface and the interface of LSC|YSZ. Besides comparative studies of the differently prepared electrodes, the degradation of the catalytic activity for the ORR at elevated temperatures was investigated. It could be shown that a process very close to the surface is responsible for the large part of the degradation. This was further verified by etching of the surface and this recovering the high catalytic activity for the ORR.

These etching experiments were further improved in a novel in-situ measurement setup using ICP-OES. Here, the surface of the thin films was continuously etched and the eluate was injected on-line into an ICP-OES instrument for quantitative chemical elementary analysis. In that way it was possible to gather quantitative information on the cation redistributions taking place at the LSC surface at elevated temperatures. In accordance with qualitative results acquired by ToF-SIMS, a segregation of Sr to the surface was observed. This Sr enrichment could be quantified to be in the range of 0.5 µg/cm² which is equivalent to about 4 atomic monolayers of SrO. The changes at the surface of the LSC films were further intensively investigated with ToF-SIMS and by collaboration partners at MIT Boston with XPS and AES.[98]

These results on cation redistributions inspired further systematic ToF-SIMS investigations of the cation mobility. LSC powders for PLD targets containing tracer isotopes (^{86}Sr/^{88}Sr) and elements (Co/Fe, La/Sm) were prepared and multilayered thin films were then fabricated by PLD. These bi- and multilayered thin films with different tracer levels were used as so called "diffusion couples". They were annealed for a

certain time to establish diffusion profiles, which were subsequently analyzed by ToF-SIMS depth profiling. By this method diffusion coefficients of the three cations in LSC were determined at remarkably low temperatures of 625-800°C. It was found that grain boundary diffusion was faster than diffusion in LSC grains. A quantification of the difference was possible by TEM analysis of the grain sizes and grain boundary density and by finite elements analysis of the depth profiles using 3D models of the thin films. About 3 orders of magnitude faster diffusion was found along grain boundaries with activation energies for all cations of ~4.1 eV compared to grain diffusion with activation energies of ~3.5 eV. Interestingly the activation energies of all cations were similar and also the absolute values of the diffusion coefficient were within one order of magnitude. This is a strong indication for a coupled diffusion mechanism for A-site and B-site cations in the LSC perovskite-type lattice.

Furthermore, it became possible to compare the kinetic diffusion parameters with the amount of Sr segregation at typical intermediate-temperature-SOFC operation conditions. It could be concluded that Sr diffusion in LSC is fast enough to cause even larger amounts of Sr at the surface than measured. Vice versa, it could be shown that suppressing the Sr segregation for technologically interesting durations by freezing the cation lattice would require temperatures below 400°C, which is too low for reasonable SOFC operation.

Isotope exchange depth profiling with ToF-SIMS was also used to investigate the surface exchange and diffusion of oxygen. By a fast gas exchange at elevated temperatures between ambient air and 200 mbar ^{18}O isotope enriched oxygen, isotope concentration depth profiles could be established in LSC thin films. Epitaxial and strained (100) LSC thin films grown on perovskite-type oxides (STO, LAO) were studied. The aim was to investigate the effect of tensile and compressive planar strain on the kinetic parameters of oxygen exchange. Both, a faster surface exchange (ca. $\times 4$) and a faster diffusion (ca. $\times 10$) could be shown for tensile strained compared to compressively strained (100) LSC thin films. The main challenge for this study was to establish and measure tracer profiles in only ~20 nm films, from which both the surface exchange and the diffusion coefficient were determined simultaneously. The temperature dependence of strained LSC thin films was measured in the range 280-

475°C. Significantly lower activation energies were observed in these experiments compared to measurements on bulk LSC at higher temperatures reported in literature. The activation energies were low enough to be almost completely explainable by the mobility of oxygen vacancies which means that the enthalpy of vacancy formation in the strained LSC films at these low temperatures was very small.

An activating effect of chemical etching of the surface of strained LSC films on k* and D* was shown, in accordance with the decrease of the electrode polarization resistance in above-mentioned impedance measurements. By using LSC on MgO as strain-neutral sample, an enhancing effect of tensile strain and a suppressing effect of compressive strain on the oxygen exchange parameters could be concluded. Additionally, the effect of tensile strain enhancing ORR kinetics compared to compressive strain was proven to be present for both compositions LSC82 and LSC64.

These investigations of oxygen isotopes by ToF-SIMS and also further measurements which were performed to investigate active and resistive zones of electrodes[190, 192, 203] required special care at the analytical measurements. In order to extract correct materials parameters, the correct isotope ratios of oxygen must be measured with high accuracy. Further, for investigations of active and resistive zones of electrodes, a high lateral resolution is desired. In the standard measurement modes suggested by the manufacturer ION-TOF for ToF-SIMS machines, these two requirements could not be achieved sufficiently. Therefore the guidance of the primary ion beam was adapted leading to a novel measurement mode which was developed together with G. Holzlechner. With this novel CBA-mode, it is possible to achieve lateral resolutions below 100 nm. Further, the primary beam intensity can be adjusted in order to influence secondary ion intensity, so that all majority and minority isotopes of interest are within the linear counting regime of the detector. By this feature it is possible to significantly improve the accuracy of oxygen isotope measurements compared to standard measurement modes. The significance and versatility of the novel CBA mode was shown by means of several examples of application. The incorporation of oxygen at Pt electrodes close to the three phase boundary was resolved in very high accuracy. Fast oxygen diffusion pathways at grain boundaries and triple junctions could be shown on steel samples. The corrosion products of copper in humid atmospheres were

measured, requiring the simultaneously high lateral and mass resolution achievable with CBA-burst mode. Further, the necessary accuracy of oxygen isotope analysis is discussed for determining surface exchange and diffusion parameters of LSC thin films on YSZ.

The same measurement mode was also employed in ^{18}O exchange and depth profiling measurements on 200 nm LSC thin films on YSZ. Complementary to these measurements the same LSC films were also investigated by impedance spectroscopy. Both analyses were performed at the same temperature, 400°C, to make a direct comparison of the results possible. A Warburg-like electrode impedance was measured and interestingly, different models for fitting yielded different rate limiting steps, either the surface exchange or bulk diffusion. To investigate which interpretation is correct ^{18}O depth profiles were analyzed. First, surface exchange and diffusion parameters were extracted which were then converted into electrode resistances. This analysis showed that surface exchange is responsible for the largest resistive contribution of the investigated LSC thin films. The total resistances which were determined with the two methods were comparable, but systematically about 30% higher polarization resistances were found with the ^{18}O tracer method. The distribution of the resistances to the electrode surface, bulk, and interface was well reproducible with the extracted parameters of one fitting model of the impedance spectra. In that way, also inhomogeneities in the LSC bulk were found that might be the reason for the misinterpretation of impedance spectra by some models. Further, even very slight differences in the high frequency part of the electrode impedance could be well correlated with a different interface resistance that appeared in tracer experiments as more or less pronounced drop of tracer fraction at the LSC|YSZ interface. Thus the analysis of the same samples by two complementary methods proved very advantageous.

7.1 Scientific publications

13: *Kubicek, M.*; Huber, S.; Opitz, A.; Penn, A.; Rupp, G. M.; Bernardi, J., Stöger-Pollach, M.; Hutter, H.; Fleig, J.	Cation Diffusion in $La_{1-x}Sr_xCoO_{3-\delta}$ Thin Films at Temperatures below 800°C	Submitted to Physical Chemistry Chemical Physics
12: Opitz, A. K.; *Kubicek M.*; Huber S.; Huber T.; Holzlechner G.; Hutter, H.; Fleig J.	Thin Film Cathodes in SOFC Research: How to identify Oxygen Reduction Pathways?	Submitted to the Journal of Materials Research
11: *Kubicek, M.*; Holzlechner G.; Opitz, A. K.; Larisegger, S.; Hutter, H.; Fleig, J.	A Novel ToF-SIMS Operation Mode for sub 100 nm Lateral Resolution: Application and Performance.	Submitted to Applied Surface Science
10: Holzlechner, G.; *Kubicek, M.*; Hutter, H.; Fleig, J.	Improved Accuracy and Lateral Resolution of Oxygen Isotope Measurements on Oxides: A Novel ToF-SIMS Operation Mode.	J. Anal. Atom. Spec. **2013**; in press.
9: *Kubicek, M.*; Cai, Z.; Wen, M.; Yildiz, B.; Hutter, H.; Fleig, J.	Tensile Lattice Strain Accelerates Oxygen Surface Exchange and Diffusion in $La_{1-x}Sr_xCoO_{3-\delta}$ Thin Films.	ACS Nano **2013**; in press.
8: Fleig, J.; *Kubicek, M.*; Huber, S.; Ahrens, M.; Langer-Hansel, K.; Gerstl, M.; Hutter, H.	Ion Transfer and Ion Transport in Thin Oxide Films Investigated by Complementary Tracer Diffusion and Impedance Spectroscopy Measurements.	ECS Transactions **2012**; pp 203-212.
7: Hagleitner, D. R.; Menhart, M.; Jacobson, P.; Blomberg, S.; Schulte, K.; Lundgren, E.; *Kubicek, M.*; Fleig, J.; Kubel, F.; Puls, C.; Limbeck, A.; Hutter, H.; Boatner, L. A.; Schmid, M.; Diebold, U.	Bulk and Surface Characterization of In_2O_3 (001) Single Crystals.	Phys Rev B **2012**, 85.

6: Cai, Z. H.; *Kubicek, M.*; Fleig, J.; Yildiz, B.	Chemical Heterogeneities on $La_{0.6}Sr_{0.4}CoO_{3-\delta}$ Thin Films-Correlations to Cathode Surface Activity and Stability.	Chem Mater **2012**, 24, 1116-1127.
5: Opitz, A. K.; Lutz, A.; *Kubicek, M.*; Kubel, F.; Hutter, H.; Fleig, J.	Investigation of the Oxygen Exchange Mechanism on Pt|Yttria Stabilized Zirconia at Intermediate Temperatures: Surface Path versus Bulk Path.	Electrochim Acta **2011**, 56, 9727-9740.
4: *Kubicek, M.*; Limbeck, A.; Fromling, T.; Hutter, H.; Fleig, J.	Relationship between Cation Segregation and the Electrochemical Oxygen Reduction Kinetics of $La_{0.6}Sr_{0.4}CoO_{3-\delta}$ Thin Film Electrodes.	Journal of the Electrochemical Society **2011**, 158, B727-B734.
3: Fleig, J.; Opitz, A.; Schintlmeister, A.; *Kubicek, M.*; Hutter, H.	Monitoring Active and Resistive Zones of SOFC Cathodes by Voltage Driven Tracer Incorporation.	ECS Transactions **2011**, 35, 2217-2226.
2: *Kubicek, M.*; Limbeck, A.; Fromling, T.; Hutter, H.; Fleig, J.	Surface Cation Segregation and its Effect on the Oxygen Reduction Reaction on Mixed Conducting Electrodes Investigated by ToF-SIMS and ICP-OES.	ECS Transactions **2011**, 35, 1975-1983.
1: Januschewsky, J.; *Kubicek, M.*; Stoeger-Pollach, M.; Bernardi, J.; Fleig, J.	Structural and Chemical Investigations of (La, Sr)CoO_{3-\delta} Thin Film Electrodes Exhibiting Very Fast Oxygen Reduction Kinetics.	ECS Transactions **2009**, 25, 2397-2402.

8 References

1.   Minh, N. Q., Ceramic Fuel Cells. J Am Ceram Soc **1993**, 76, 563-588.

2.   Steele, B. C. H.; Heinzel, A., Materials for fuel-cell technologies. Nature **2001**, 414, 345-352.

3.   Fuel Cell Handbook 7th Edition. EG and G Technical Services of West Virginia, Inc., Morgantown, WV.: **2004**.

4.   Yamamoto, O., Solid oxide fuel cells: fundamental aspects and prospects. Electrochim Acta **2000**, 45, 2423-2435.

5.   Ormerod, R. M., Solid oxide fuel cells. Chemical Society Reviews **2003**, 32, 17-28.

6.   Jacobson, A. J., Materials for Solid Oxide Fuel Cells†. Chem Mater **2009**, 22, 660-674.

7.   Yokokawa, H.; Tu, H. Y.; Iwanschitz, B.; Mai, A., Fundamental mechanisms limiting solid oxide fuel cell durability. Journal of Power Sources **2008**, 182, 400-412.

8.   Fleig, J., Solid oxide fuel cell cathodes: Polarization mechanisms and modeling of the electrochemical performance. Annu Rev Mater Res **2003**, 33, 361-382.

9.   Adler, S. B., Factors governing oxygen reduction in solid oxide fuel cell cathodes. Chem Rev **2004**, 104, 4791-4843.

10.   Ullmann, H.; Trofimenko, N.; Tietz, F.; Stöver, D.; Ahmad-Khanlou, A., Correlation between thermal expansion and oxide ion transport in mixed conducting perovskite-type oxides for SOFC cathodes. Solid State Ionics **2000**, 138, 79-90.

11.   Möbius, H.-H., On the history of solid electrolyte fuel cells. J Solid State Electr **1997**, 1, 2-16.

12.   Mastin, J.; Einarsrud, M. A.; Grande, T., Structural and thermal properties of $La_{1-x}Sr_xCoO_{3-\delta}$. Chem Mater **2006**, 18, 6047-6053.

13.   Petrov, A. N.; Kononchuk, O. F.; Andreev, A. V.; Cherepanov, V. A.; Kofstad, P., Crystal-Structure, Electrical and Magnetic-Properties of $La_{1-x}Sr_xCoO_{3-\delta}$. Solid State Ionics **1995**, 80, 189-199.

14.   Sitte, W.; Bucher, E.; Preis, W., Nonstoichiometry and transport properties of strontium-substituted lanthanum cobaltites. Solid State Ionics **2002**, 154–155, 517-522.

15.   Yamamoto, O.; Takeda, Y.; Kanno, R.; Noda, M., Perovskite-Type Oxides as Oxygen Electrodes for High-Temperature Oxide Fuel-Cells. Solid State Ionics **1987**, 22, 241-246.

16.   Sase, M.; Ueno, D.; Yashiro, K.; Kaimai, A.; Kawada, T.; Mizusaki, J., Interfacial reaction and electrochemical properties of dense $(La,Sr)CoO_{3-\delta}$ cathode on YSZ(100). J Phys Chem Solids **2005**, 66, 343-348.

17.   Ovenstone, J.; White, J. S.; Misture, S. T., Phase transitions and phase decomposition of $La_{1-x}Sr_xCoO_{3-delta}$ in low oxygen partial pressures. Journal of Power Sources **2008**, 181, 56-61.

18.   Sharma, V. I.; Yildiz, B., Degradation Mechanism in $La_{0.8}Sr_{0.2}CoO_3$ as Contact Layer on the Solid Oxide Electrolysis Cell Anode. Journal of the Electrochemical Society **2010**, 157, B441-B448.

19.   Peters, C.; Weber, A.; Ivers-Tiffee, E., Nanoscaled $La_{0.5}Sr_{0.5}CoO_{3-delta}$ thin film cathodes for SOFC application at 500 °C < T < 700 °C. Journal of The Electrochemical Society **2008**, 155, B730-B737.

20.   Hayd, J.; Dieterle, L.; Guntow, U.; Gerthsen, D.; Ivers-Tiffee, E., Nanoscaled $La_{0.6}Sr_{0.4}CoO_{3-delta}$ as intermediate temperature solid oxide fuel cell cathode: Microstructure and electrochemical performance. J Power Sources **2011**, 196, 7263-7270.

21.   Crumlin, E. J.; Mutoro, E.; Ahn, S. J.; La O, G. J.; Leonard, D. N.; Borisevich, A.; Biegalski, M. D.; Christen, H. M.; Shao-Horn, Y., Oxygen reduction kinetics enhancement on a heterostructured oxide surface for solid oxide fuel cells. J Phys Chem Lett **2010**, 1, 3149-3155.

22.   Baumann, F. S.; Fleig, J.; Konuma, M.; Starke, U.; Habermeier, H. U.; Maier, J., Strong performance improvement of $La_{0.6}Sr_{0.4}Co_{0.8}Fe_{0.2}O_{3-\delta}$ SOFC cathodes by electrochemical activation. Journal of The Electrochemical Society **2005**, 152, A2074-A2079.

23.   Jiang, S. P.; Love, J. G., Origin of the initial polarization behavior of Sr-doped $LaMnO_3$ for O_2 reduction in solid oxide fuel cells. Solid State Ionics **2001**, 138, 183-190.

24.   Burriel, M.; Garcia, G.; Santiso, J.; Kilner, J. A.; Richard, J. C. C.; Skinner, S. J., Anisotropic oxygen diffusion properties in epitaxial thin films of $La_2NiO_{4+delta}$. Journal of Materials Chemistry **2008**, 18, 416-422.

25.   Oh, D.; Gostovic, D.; Wachsman, E. D., Mechanism of $La_{0.6}Sr_{0.4}Co_{0.2}Fe_{0.8}O_3$ cathode degradation. Journal of Materials Research **2012**, 27, 1992-1999.

26.   Bucher, E.; Sitte, W.; Klauser, F.; Bertel, E., Impact of humid atmospheres on oxygen exchange properties, surface-near elemental composition, and surface morphology of $La_{0.6}Sr_{0.4}CoO_{3-delta}$. Solid State Ionics **2012**, 208, 43-51.

27.   Hjalmarsson, P.; Sogaard, M.; Mogensen, M., Electrochemical performance and degradation of $(La_{0.6}Sr_{0.4})_{0.99}CoO_{3-delta}$ as porous SOFC-cathode. Solid State Ionics **2008**, 179, 1422-1426.

28.   Kubicek, M.; Limbeck, A.; Fromling, T.; Hutter, H.; Fleig, J., Relationship between Cation Segregation and the Electrochemical Oxygen Reduction Kinetics of $La_{0.6}Sr_{0.4}CoO_{3-delta}$ Thin Film Electrodes. Journal of The Electrochemical Society **2011**, 158, B727-B734.

29.   Bieberle-Hutter, A.; Sogaard, M.; Tuller, H. L., Electrical and electrochemical characterization of microstructured thin film $La_{1-x}Sr_xCoO_3$ electrodes. Solid State Ionics **2006**, 177, 1969-1975.

30.   Baumann, F. S.; Maier, J.; Fleig, J., The polarization resistance of mixed conducting SOFC cathodes: A comparative study using thin film model electrodes. Solid State Ionics **2008**, 179, 1198-1204.

31.   Fleig, J.; Baumann, F. S.; Brichzin, V.; Kim, H. R.; Jamnik, J.; Cristiani, G.; Habermeier, H. U.; Maier, J., Thin film microelectrodes in SOFC electrode research. Fuel Cells **2006**, 6, 284-292.

32.   Kawada, T.; Horita, T.; Sakai, N.; Yokokawa, H.; Dokiya, M.; Mizusaki, J., Novel technique for imaging electrochemical reaction sites on a solid oxide electrolyte. Solid State Ionics **2000**, 131, 199-210.

33.   Mori, D.; Oka, H.; Suzuki, Y.; Sonoyama, N.; Yamada, A.; Kanno, R.; Sumiya, Y.; Imanishi, N.; Takeda, Y., Synthesis, structure, and electrochemical properties of epitaxial perovskite $La_{0.8}Sr_{0.2}CoO_3$ film on YSZ substrate. Solid State Ionics **2006**, 177, 535-540.

34.   Baumann, F. S.; Fleig, J.; Cristiani, G.; Stuhlhofer, B.; Habermeier, H. U.; Maier, J., Quantitative comparison of mixed conducting SOFC cathode materials by means of thin film model electrodes. Journal of The Electrochemical Society **2007**, 154, B931-B941.

35.		Ringuede, A.; Fouletier, J., Oxygen reaction on strontium-doped lanthanum cobaltite dense electrodes at intermediate temperatures. Solid State Ionics **2001**, 139, 167-177.

36.		Dieterle, L.; Bach, D.; Schneider, R.; Stormer, H.; Gerthsen, D.; Guntow, U.; Ivers-Tiffee, E.; Weber, A.; Peters, C.; Yokokawa, H., Structural and chemical properties of nanocrystalline $La_{0.5}Sr_{0.5}CoO_{3-delta}$ layers on yttria-stabilized zirconia analyzed by transmission electron microscopy. Journal of Materials Science **2008**, 43, 3135-3143.

37.		Kweon, H. J.; Park, D. G.; Kuk, S. T.; Park, H. B.; Kim, K., Synthesis of $La_{1-x}Sr_xCoO_3$ ($x \leq 0.2$) at low temperature from PVA-polymeric gel precursors. Bulletin of the Korean Chemical Society **1997**, 18, 1249-1256.

38.		Horita, T.; Yamaji, K.; Sakai, N.; Yokokawa, H.; Weber, A.; Ivers-Tiffée, E., Oxygen reduction mechanism at porous $La_{1-x}Sr_xCoO_{3-d}$ cathodes/$La_{0.8}Sr_{0.2}Ga_{0.8}Mg_{0.2}O_{2.8}$ electrolyte interface for solid oxide fuel cells. Electrochimica Acta **2001**, 46, 1837-1845.

39.		Lu, Y. X.; Kreller, C.; Adler, S. B., Measurement and Modeling of the Impedance Characteristics of Porous $La_{1-x}Sr_xCoO_{3-delta}$ Electrodes. Journal of the Electrochemical Society **2009**, 156, B513-B525.

40.		Torres-Garibay, C.; Kovar, D.; Manthiram, A., $Ln_{0.6}Sr_{0.4}Co_{1-y}Fe_yO_{3-delta}$ (Ln = La and Nd; $y = 0$ and 0.5) cathodes with thin yttria-stabilized zirconia electrolytes for intermediate temperature solid oxide fuel cells. Journal of Power Sources **2009**, 187, 480-486.

41.		Wang, J.; Manivannan, A.; Wu, N., Sol-gel derived $La_{0.6}Sr_{0.4}CoO_3$ nanoparticles, nanotubes, nanowires and thin films. Thin Solid Films **2008**, 517, 582-587.

42.		Januschewsky, J.; Ahrens, M.; Opitz, A.; Kubel, F.; Fleig, J., Optimized $La_{0.6}Sr_{0.4}CoO_{3-delta}$ Thin-Film Electrodes with Extremely Fast Oxygen-Reduction Kinetics. Adv Funct Mater **2009**, 19, 3151-3156.

43.		Endo, A.; Fukunaga, H.; Wen, C.; Yamada, K., Cathodic reaction mechanism of dense $La_{0.6}Sr_{0.4}CoO_3$ and $La_{0.81}Sr_{0.09}MnO_3$ electrodes for solid oxide fuel cells. Solid State Ionics **2000**, 135, 353-358.

44.		Yang, Y. M. L.; Jacobson, A. J.; Chen, C. L.; Luo, G. P.; Ross, K. D.; Chu, C. W., Oxygen exchange kinetics on a highly oriented $La_{0.5}Sr_{0.5}CoO_{3-delta}$ thin film prepared by pulsed-laser deposition. Applied Physics Letters **2001**, 79, 776-778.

45.   Sase, M.; Suzuki, J.; Yashiro, K.; Otake, T.; Kaimai, A.; Kawada, T.; Mizusaki, J.; Yugami, H., Electrode reaction and microstructure of $La_{0.6}Sr_{0.4}CoO_{3-delta}$ thin films. Solid State Ionics **2006**, 177, 1961-1964.

46.   Pecchini, M. P., US patent **1967**, No. 3 330 679.47.   Baumann, F. S.; Fleig, J.; Habermeier, H. U.; Maier, J., $Ba_{0.5}Sr_{0.5}Co_{0.8}Fe_{0.2}O_{3-delta}$ thin film microelectrodes investigated by impedance spectroscopy. Solid State Ionics **2006**, 177, 3187-3191.

48.   Baumann, F. S.; Fleig, J.; Habermeier, H. U.; Maier, J., Impedance spectroscopic study on well-defined $(La,Sr)(Co,Fe)O_{3-delta}$ model electrodes. Solid State Ionics **2006**, 177, 1071-1081.

49.   Jamnik, J.; Maier, J., Generalised equivalent circuits for mass and charge transport: chemical capacitance and its implications. Phys Chem Chem Phys **2001**, 3, 1668-1678.

50.   Gnaser, H., Low-energy ion irradiation of solid surfaces - Introduction. Low-Energy Ion Irradiation of Solid Surfaces **1999**, 146.

51.   Zalm, P. C., Ultra-Shallow Doping Profiling with Sims. Reports on Progress in Physics **1995**, 58, 1321-1374.

52.   Fearn, S.; Rossiny, J.; Kilner, J., SIMS artifacts in the near surface depth profiling of oxygen conducting ceramics. Solid State Ionics **2008**, 179, 811-815.

53.   Wu, Q. H.; Liu, M. L.; Jaegermann, W., X-ray photoelectron spectroscopy of $La_{0.5}Sr_{0.5}MnO_3$. Materials Letters **2005**, 59, 1980-1983.

54.   Bertacco, R.; Contour, J. P.; Barthelemy, A.; Olivier, J., Evidence for strontium segregation in $La_{0.7}Sr_{0.3}MnO_3$ thin films grown by pulsed laser deposition: consequences for tunnelling junctions. Surface Science **2002**, 511, 366-372.

55.   Jiang, S. P., Activation, microstructure, and polarization of solid oxide fuel cell cathodes. Journal of Solid State Electrochemistry **2006**, 11, 93-102.

56.   Chang, K. C.; Ingram, B.; Kavaipatti, B.; Yildiz, B.; Hennessy, D.; Salvador, P.; Leyarovska, N.; You, H., In situ Synchrotron X-ray Studies of Dense Thin-Film Strontium-Doped Lanthanum Manganite Solid Oxide Fuel Cell Cathodes. Solid-State Ionics-2008 **2009**, 1126, 27-32171.

57.   Szot, K.; Speier, W., Surfaces of reduced and oxidized $SrTiO_3$ from atomic force microscopy. Physical Review B **1999**, 60, 5909-5926.

58.   Szot, K.; Speier, W.; Breuer, U.; Meyer, R.; Szade, J.; Waser, R., Formation of micro-crystals on the (100) surface of $SrTiO_3$ at elevated temperatures. Surface Science **2000**, 460, 112-128.

59.   Jung, W.; Tuller, H. L., Investigation of Cathode Behavior and Surface Chemistry of Model Thin Film $SrTi_{1-x}Fe_xO_{3-d}$ Electrode. ECS Transactions **2009**, 25, 2775-2782.

60.   Januschewsky, J.; Kubicek, M.; Stoeger-Pollach, M.; Bernardi, J.; Fleig, J., Structural and chemical investigations of $(La,Sr)CoO_{3-d}$ thin film electrodes exhibiting very fast oxygen reduction kinetics. ECS Transactions **2009**, 25, 2397-2402.

61.   Kostgloudis, G. C.; Tsiniarakis, G.; Ftikos, C., Chemical reactivity of perovskite oxide SOFC cathodes and yttria stabilized zirconia. Solid State Ionics **2000**, 135, 529-535.

62.   Rohnke, M.; Falk, M.; Huber, A.-K.; Janek, J., Combining high temperature electrochemistry and time of flight secondary ion mass spectrometry: Quasi in situ study of lanthanum strontium chromate manganate electrodes. J Power Sources **2013**, 221, 97-107.

63.   Akashi, T.; Nanko, M.; Maruyama, T.; Shiraishi, Y.; Tanabe, J., Solid-state reaction kinetics of $LaCrO_3$ from the oxides and determination of La^{3+} diffusion coefficient. Journal of The Electrochemical Society **1998**, 145, 2090-2094.

64.   Palcut, M.; Wiik, K.; Grande, T., Cation self-diffusion in $LaCoO_3$ and La_2CoO_4 studied by diffusion couple experiments. J Phys Chem B **2007**, 111, 2299-2308.

65.   Smith, J. B.; Norby, T., Cation self-diffusion in $LaFeO_3$ measured by the solid state reaction method. Solid State Ionics **2006**, 177, 639-646.

66.   Palcut, M.; Knibbe, R.; Wiik, K.; Grande, T., Cation inter-diffusion between $LaMnO_3$ and $LaCoO_3$ materials. Solid State Ionics **2011**, 202, 6-13.

67.   Smith, J. B.; Norby, T.; Fossdal, A., Electron probe micro analysis of A-site inter-diffusion between $LaFeO_3$ and $NdFeO_3$. J Am Ceram Soc **2006**, 89, 582-586.

68.   Miyoshi, S.; Martin, M., B-Site cation diffusivity of Mn and Cr in perovskite-type $LaMnO_3$ with cation-deficit nonstoichiometry. Phys Chem Chem Phys **2009**, 11, 3063-3070.

69.   Horita, T.; Ishikawa, M.; Yamaji, K.; Sakai, N.; Yokokawa, H.; Dokiya, M., Calcium tracer diffusion in $(La,Ca)CrO_3$ by SIMS. Solid State Ionics **1999**, 124, 301-307.

70.   Palcut, M.; Christensen, J. S.; Wiik, K.; Grande, T., Impurity diffusion of Pr-141 in $LaMnO_3$, $LaCoO_3$ and $LaFeO_3$ materials. Phys Chem Chem Phys **2008**, 10, 6544-6552.

71.   Schulz, O.; Martin, M.; Argirusis, C.; Borchardt, G., Cation tracer diffusion of La-138, Sr-84 and Mg-25 in polycrystalline $La_{0.9}Sr_{0.1}Ga_{0.9}Mg_{0.1}O_{2.9}$. Phys Chem Chem Phys **2003**, 5, 2308-2313.

72.   Waernhus, I.; Sakai, N.; Yokokawa, H.; Grande, T.; Einarsrud, M. A.; Wiik, K., Mass transport in $La_{1-x}Sr_xFeO_3 (x = 0$ and 0.1) measured by SIMS. Solid State Ionics **2004**, 175, 69-71.

73.   Waernhus, I.; Sakai, N.; Yokokawa, H.; Grande, T.; Einarsrud, M. A.; Wiik, K., Cation diffusion in $La_{1-x}Sr_xFeO_{3-delta}$, $x = 0$ and 0.1 measured by SIMS. Solid State Ionics **2007**, 178, 907-914.

74.   Koerfer, S.; De Souza, R. A.; Yoo, H. I.; Martin, M., Diffusion of Sr and Zr in BaTiO3 single crystals. Solid State Sciences **2008**, 10, 725-734.

75.   Gomann, K.; Bochardt, G.; Schulz, M.; Gomann, A.; Maus-Friedrichs, W.; Lesage, B.; Kaitasov, O.; Hoffman-Eifert, S.; Schneller, T., Sr diffusion in undoped and La-doped $SrTiO_3$ single crystals under oxidizing conditions. Phys Chem Chem Phys **2005**, 7, 2053-2060.

76.   Kishimoto, H.; Sakai, N.; Horita, T.; Yamaji, K.; Brito, M. E.; Yokokawa, H., Cation transport behavior in SOFC cathode materials of $La_{0.8}Sr_{0.2}CoO_3$ and $La_{0.8}Sr_{0.2}FeO_3$ with perovskite structure. Solid State Ionics **2007**, 178, 1317-1325.

77.   Harvey, S. P.; De Souza, R. A.; Martin, M., Diffusion of la and Mn in $Ba_{0.5}Sr_{0.5}Co_{0.8}Fe_{0.2}O_{3-\delta}$ polycrystalline ceramics. Energy and Environmental Science **2012**, 5, 5803-5813.

78.   Norton, D. P., Pulsed Laser Deposition of Thin Films. Eason, R., Ed. John Wiley & Sons, Inc.: **2007**.

79.   Rupp, G. Relation between surface composition of $(La,Sr)CoO_{3-\delta}$ thin film electrodes and oxygen reduction kinetics. Vienna University of Technology, **2012**.

80.   Ohno, Y.; Nagata, S.; Sato, H., Properties of Oxides for High-Temperature Solid Electrolyte Fuel-Cell. Solid State Ionics **1983**, 9-10, 1001-1007.

81.   ICDD (2010). PDF-4/Organics 2011 (Database), International; Centre for Diffraction Data, N. S., PA, USA.

82.	Plonczak, P.; Bieberle-Hutter, A.; Sogaard, M.; Ryll, T.; Martynczuk, J.; Hendriksen, P. V.; Gauckler, L. J., Tailoring of $La_xSr_{1-x}Co_yFe_{1-y}O_{3-delta}$ Nanostructure by Pulsed Laser Deposition. Adv Funct Mater **2011**, 21, 2764-2775.

83.	Crank, J., The mathematics of diffusion. 2nd Edn. Oxford University Press, Oxford **1979**.

84.	Whipple, R. T. P., CXXXVIII. Concentration contours in grain boundary diffusion. Philosophical Magazine Series 7 **1954**, 45, 1225-1236.

85.	Le Claire, A. D., The analysis of grain boundary diffusion measurements. British Journal of Applied Physics **1963**, 14, 351-356.

86.	Subramaniam, A.; Koch, C. T.; Cannon, R. M.; Rühle, M., Intergranular glassy films: An overview. Materials Science and Engineering A **2006**, 422, 3-18.

87.	Xing, J.; Gu, H.; Heo, Y. U.; Takeguchi, M., Initial transient structure and chemistry of intergranular glassy films in ferric-oxide doped strontium titanate ceramics. J Mater Sci **2011**, 46, 4361-4367.

88.	Yoo, H. I.; Lee, C. E.; De Souza, R. A.; Martin, M., Equal mobility of constituent cations in $BaTiO_3$. Applied Physics Letters **2008**, 92.

89.	Xu, J. S.; Yamazaki, D.; Katsura, T.; Wu, X. P.; Remmert, P.; Yurimoto, H.; Chakraborty, S., Silicon and magnesium diffusion in a single crystal of $MgSiO_3$ perovskite. J Geophys Res-Sol Ea **2011**, 116.

90.	Sakai, N.; Yamaji, K.; Horita, T.; Negishi, H.; Yokokawa, H., Chromium diffusion in lanthanum chromites. Solid State Ionics **2000**, 135, 469-474.

91.	Meyer, R.; Waser, R.; Helmbold, J.; Borchardt, G., Observation of vacancy defect migration in the cation sublattice of complex oxides by O-18 tracer experiments. Phys Rev Lett **2003**, 90.

92.	De Souza, R. A.; Islam, M. S.; Ivers-Tiffee, E., Formation add migration of cation defects in the perovskite oxide $LaMnO_3$. Journal of Materials Chemistry **1999**, 9, 1621-1627.

93.	Jones, A.; Islam, M. S., Atomic-scale insight into $LaFeO_3$ perovskite: Defect nanoclusters and ion migration. J Phys Chem C **2008**, 112, 4455-4462.

94.	De Souza, R. A.; Maier, J., A computational study of cation defects in $LaGaO_3$. Phys Chem Chem Phys **2003**, 5, 740-748.

95.	Kilo, M.; Taylor, M. A.; Argirusis, C.; Borchardt, G.; Jackson, R. A.; Schulz, O.; Martin, M.; Weller, M., Modeling of cation diffusion in oxygen ion conductors using molecular dynamics. Solid State Ionics **2004**, 175, 823-827.

96.   Walsh, A.; Catlow, C. R. A.; Smith, A. G. H.; Sokol, A. A.; Woodley, S. M., Strontium migration assisted by oxygen vacancies in $SrTiO_3$ from classical and quantum mechanical simulations. Phys Rev B **2011**, 83.

97.   Cai, Z.; Kuru, Y.; Han, J. W.; Chen, Y.; Yildiz, B., Surface Electronic Structure Transitions at High Temperature on Perovskite Oxides: The Case of Strained $La_{0.8}Sr_{0.2}CoO_3$ Thin Films. Journal of the American Chemical Society **2011**, 133, 17696-17704.

98.   Cai, Z. H.; Kubicek, M.; Fleig, J.; Yildiz, B., Chemical Heterogeneities on $La_{0.6}Sr_{0.4}CoO_{3-delta}$ Thin Films-Correlations to Cathode Surface Activity and Stability. Chem Mater **2012**, 24, 1116-1127.

99.   Monceau, D.; Filal, M.; Tebtoub, M.; Petot, C.; Petot-Ervas, G., Kinetic demixing of ceramics in an electrical field. Solid State Ionics **1994**, 73, 221-225.

100.   Szot, K.; Speier, W.; Herion, J.; Freiburg, C., Restructuring of the surface region in $SrTiO_3$. Appl Phys A **1996**, 64, 55-59.

101.   Jung, W.; Tuller, H. L., Investigation of surface Sr segregation in model thin film solid oxide fuel cell perovskite electrodes. Energ Environ Sci **2012**, 5, 5370-5378.

102.   Shannon, R., Revised effective ionic radii and systematic studies of interatomic distances in halides and chalcogenides. Acta Crystallographica Section A **1976**, 32, 751-767.

103.   Maier, J., Physical Chemistry of Ionic Materials. Ions and Electrons in Solids. John Wiley & Sons, Ltd, Chichester: **2004**.

104.   Kubicek, M.; Cai, Z.; Ma, W.; Yildiz, B.; Hutter, H.; Fleig, J., Tensile Lattice Strain Accelerates Oxygen Surface Exchange and Diffusion in $La_{1-x}Sr_xCoO_{3-\delta}$ Thin Films. Acs Nano **2013**.

105.   Rata, A. D.; Herklotz, A.; Nenkov, K.; Schultz, L.; Dorr, K., Strain-induced insulator state and giant gauge factor of $La_{0.7}Sr_{0.3}CoO_3$ films. Phys Rev Lett **2008**, 100.

106.   Hou, F.; Cai, T. Y.; Ju, S.; Shen, M. R., Half-Metallic Ferromagnetism via the Interface Electronic Reconstruction in $LaAlO_3/SrMnO_3$ Nanosheet Superlattices. Acs Nano **2012**, 6, 8552-8562.

107.   Cantoni, C.; Gao, Y. F.; Wee, S. H.; Specht, E. D.; Gazquez, J.; Meng, J. Y.; Pennycook, S. J.; Goyal, A., Strain-Driven Oxygen Deficiency in Self-Assembled, Nanostructured, Composite Oxide Films. Acs Nano **2011**, 5, 4783-4789.

108.   Estrade, S.; Rebled, J. M.; Arbiol, J.; Peiro, F.; Infante, I. C.; Herranz, G.; Sanchez, F.; Fontcuberta, J.; Cordoba, R.; Mendis, B. G.; Bleloch, A. L., Effects of thickness on the cation segregation in epitaxial (001) and (110) $La_{2/3}Ca_{1/3}MnO_3$ thin films. Applied Physics Letters **2009**, 95, 072507-3.

109.   Estradé, S.; Arbiol, J.; Peiró, F.; Infante, I. C.; Sánchez, F.; Fontcuberta, J.; De La Peña, F.; Walls, M.; Colliex, C., Cationic and charge segregation in $La_{2/3}Ca_{1/3}MnO_3$ thin films grown on (001) and (110) SrTiO3. Applied Physics Letters **2008**, 93.

110.   Estradé, S.; Arbiol, J.; Peiró, F.; Abad, L.; Laukhin, V.; Balcells, L.; Martínez, B., Cationic diffusion in $La_{2/3}Ca_{1/3}MnO_3$ thin films grown on $LaAlO_3$ (001) substrates. Applied Physics Letters **2007**, 91.

111.   Lussier, A.; Dvorak, J.; Stadler, S.; Holroyd, J.; Liberati, M.; Arenholz, E.; Ogale, S. B.; Wu, T.; Venkatesan, T.; Idzerda, Y. U., Stress relaxation of $La_{1/2}Sr_{1/2}MnO_3$ and $La_{2/3}Ca_{1/3}MnO_3$ at solid oxide fuel cell interfaces. Thin Solid Films **2008**, 516, 880-884.

112.   Jalili, H.; Han, J. W.; Kuru, Y.; Cai, Z. H.; Yildiz, B., New Insights into the Strain Coupling to Surface Chemistry, Electronic Structure, and Reactivity of $La_{0.7}Sr_{0.3}MnO_3$. J Phys Chem Lett **2011**, 2, 801-807.

113.   Schichtel, N.; Korte, C.; Hesse, D.; Janek, J., Elastic strain at interfaces and its influence on ionic conductivity in nanoscaled solid electrolyte thin films-theoretical considerations and experimental studies. Phys Chem Chem Phys **2009**, 11, 3043-3048.

114.   Kushima, A.; Yildiz, B., Oxygen ion diffusivity in strained yttria stabilized zirconia: where is the fastest strain? Journal of Materials Chemistry **2010**, 20, 4809-4819.

115.   Han, J. W.; Yildiz, B., Enhanced one dimensional mobility of oxygen on strained $LaCoO_3$ (001) surface. Journal of Materials Chemistry **2011**, 21, 18983-18990.

116.   Kushima, A.; Yip, S.; Yildiz, B., Competing strain effects in reactivity of $LaCoO_3$ with oxygen. Phys Rev B **2010**, 82.

117.   Ji, H. I.; Hwang, J.; Yoon, K. J.; Son, J. W.; Kim, B. K.; Lee, H. W.; Lee, J. H., Enhanced oxygen diffusion in epitaxial lanthanum-strontium-cobaltite thin film cathodes for micro solid oxide fuel cells. Energ Environ Sci **2013**, 6, 116-120.

118.   Yashima, M.; Nomura, K.; Kageyama, H.; Miyazaki, Y.; Chitose, N.; Adachi, K., Conduction path and disorder in the fast oxide-ion conductor $La_{0.8}Sr_{0.2}Ga_{0.8}Mg_{0.15}Co_{0.05}O_{2.8}$. Chem Phys Lett **2003**, 380, 391-396.

119.   Gunter, M. M.; Boysen, H.; Corte, C.; Lerch, M.; Suard, E., In-situ investigation of oxygen diffusion in Sr, Mg-doped $LaGaO_3$ superionic conductors with a simultaneously applied electric field. Z Kristallogr **2005**, 220, 218-224.

120.   Islam, M. S., Ionic transport in ABO_3 perovskite oxides: a computer modelling tour. Journal of Materials Chemistry **2000**, 10, 1027-1038.

121.   Kilner, J. A.; Skinner, S. J.; Brongersma, H. H., The isotope exchange depth profiling (IEDP) technique using SIMS and LEIS. J Solid State Electr **2011**, 15, 861-876.

122.   De Souza, R. A.; Kilner, J. A., Oxygen transport in $La_{1-x}Sr_xMn_{1-y}Co_yO_{3\pm\delta}$ perovskites Part I. Oxygen tracer diffusion. Solid State Ionics **1998**, 106, 175-187.

123.   van Doorn, R. E.; Fullarton, I. C.; de Souza, R. A.; Kilner, J. A.; Bouwmeester, H. J. M.; Burggraaf, A. J., Surface oxygen exchange of $La_{0.3}Sr_{0.7}CoO_{3-\delta}$. Solid State Ionics **1997**, 96, 1-7.

124.   van der Haar, L. M.; den Otter, M. W.; Morskate, M.; Bouwmeester, H. J. M.; Verweij , H., Chemical Diffusion and Oxygen Surface Transfer of $La_{1-x}Sr_xCoO_{3-\delta}$ Studied with Electrical Conductivity Relaxation. Journal of The Electrochemical Society **2002**, 149, J41-J46.

125.   Wang, J. Y.; Starke, U.; Mittemeijer, E. J., Evaluation of the depth resolutions of Auger electron spectroscopic, X-ray photoelectron spectroscopic and time-of-flight secondary-ion mass spectrometric sputter depth profiling techniques. Thin Solid Films **2009**, 517, 3402-3407.

126.   Escobar Galindo, R.; Gago, R.; Albella, J. M.; Lousa, A., Comparative depth-profiling analysis of nanometer-metal multilayers by ion-probing techniques. TrAC Trends in Analytical Chemistry **2009**, 28, 494-505.

127.   Pergolesi, D.; Fabbri, E.; Cook, S. N.; Roddatis, V.; Traversa, E.; Kilner, J. A., Tensile Lattice Distortion Does Not Affect Oxygen Transport in Yttria-Stabilized Zirconia–CeO_2 Heterointerfaces. Acs Nano **2012**.

128.   den Otter, M. W.; van der Haar, L. M.; Bouwmeester, H. J. M., Numerical evaluation of eigenvalues of the sheet diffusion problem in the surface/diffusion mixed regime. Solid State Ionics **2000**, 134, 259-264.

129.   Schneider, C. W.; Esposito, M.; Marozau, I.; Conder, K.; Doebeli, M.; Hu, Y.; Mallepell, M.; Wokaun, A.; Lippert, T., The origin of oxygen in oxide thin films: Role of the substrate. Applied Physics Letters **2010**, 97.

130.	De Souza, R. A.; Metlenko, V.; Park, D.; Weirich, T. E., Behavior of oxygen vacancies in single-crystal $SrTiO_3$: Equilibrium distribution and diffusion kinetics. Phys Rev B **2012**, 85.

131.	Ishigaki, T.; Yamauchi, S.; Kishio, K.; Mizusaki, J.; Fueki, K., Diffusion of oxide ion vacancies in perovskite-type oxides. Journal of Solid State Chemistry **1988**, 73, 179-187.

132.	Teraoka, Y.; Nobunaga, T.; Okamoto, K.; Miura, N.; Yamazoe, N., Influence of constituent metal cations in substituted $LaCoO_3$ on mixed conductivity and oxygen permeability. Solid State Ionics **1991**, 48, 207-212.

133.	Tsvetkov, D. S.; Zuev, A. Y.; Vylkov, A. I.; Petrov, A. N., Oxide ion transport in undoped and Cr-doped $LaCoO_{3-\delta}$. Solid State Ionics **2007**, 178, 1458-1462.

134.	Ishigaki, T.; Yamauchi, S.; Mizusaki, J.; Fueki, K.; Tamura, H., Tracer diffusion coefficient of oxide ions in $LaCoO_3$ single crystal. Journal of Solid State Chemistry **1984**, 54, 100-107.

135.	Denk, I.; Munch, W.; Maier, J., Partial conductivities in $SrTiO_3$: Bulk polarization experiments, oxygen concentration cell measurements, and defect-chemical modeling. J Am Ceram Soc **1995**, 78, 3265-3272.

136.	Mizusaki, J.; Yasuda, I.; Shimoyama, J.-i.; Yamauchi, S.; Fueki, K., Electrical conductivity, defect equilibrium and oxygen vacancy diffusion coefficient of $La_{1-x}Ca_xAlO_{3-\delta}$ single crystals. Journal of The Electrochemical Society **1993**, 140, 467-471.

137.	Lybye, D.; Poulsen, F. W.; Mogensen, M., Conductivity of A- and B-site doped $LaAlO_3$, $LaGaO_3$, $LaScO_3$ and $LaInO_3$ perovskites. Solid State Ionics **2000**, 128, 91-103.

138.	Nomura, K.; Tanase, S., Electrical conduction behavior in $La_{0.9}Sr_{0.1}M^{III}O_{3-\delta}$ (M^{III} = Al, Ga, Sc, In, and Lu) perovskites. Solid State Ionics **1997**, 98, 229-236.

139.	Mizusaki, J.; Mima, Y.; Yamauchi, S.; Fueki, K.; Tagawa, H., Nonstoichiometry of the perovskite-type oxides $La_{1-x}Sr_xCoO_{3-\delta}$. Journal of Solid State Chemistry **1989**, 80, 102-111.

140.	Kuhn, M.; Fukuda, Y.; Hashimoto, S.; Sato, K.; Yashiro, K.; Mizusaki, J., Oxygen Nonstoichiometry of Perovskite-type $La_{0.6}Sr_{0.4}Co_{1-y}Fe_yO_{3-delta}$ (y = 0, 0.2, 0.4, 0.5, 0.6, 0.8, 1) SOFC Cathode Materials. Ecs Transactions **2011**, 35, 1881-1890.

141.   Kuhn, M.; Hashimoto, S.; Sato, K.; Yashiro, K.; Mizusaki, J., Oxygen nonstoichiometry, thermo-chemical stability and lattice expansion of $La_{0.6}Sr_{0.4}FeO_{3-delta}$. Solid State Ionics **2011**, 195, 7-15.

142.   Kawada, T.; Suzuki, J.; Sase, M.; Kaimai, A.; Yashiro, K.; Nigara, Y.; Mizusaki, J.; Kawamura, K.; Yugami, H., Determination of oxygen vacancy concentration in a thin film of $La_{0.6}Sr_{0.4}CoO_{3-\delta}$ by an electrochemical method. Journal of The Electrochemical Society **2002**, 149, E252-E259.

143.   De Souza, R. A.; Kilner, J. A., Oxygen transport in $La_{1-x}Sr_xMn_{1-y}Co_yO_{3\pm\delta}$ perovskites: Part II. Oxygen surface exchange. Solid State Ionics **1999**, 126, 153-161.

144.   Mastrikov, Y. A.; Merkle, R.; Heifets, E.; Kotomin, E. A.; Maier, J., Pathways for oxygen incorporation in mixed conducting perovskites: A DFT-based Mechanistic analysis for $(La,Sr)MnO_{3-\delta}$. J Phys Chem C **2010**, 114, 3017-3027.

145.   Kuru, Y.; Marrocchelli, D.; Bishop, S. R.; Chen, D.; Yildiz, B.; Tuller, H. L., Anomalous Chemical Expansion Behavior of $Pr_{0.2}Ce_{0.8}O_{2-delta}$ Thin Films Grown by Pulsed Laser Deposition. Journal of The Electrochemical Society **2012**, 159, F799-F803.

146.   Lee, Y. L.; Kleis, J.; Rossmeisl, J.; Shao-Horn, Y.; Morgan, D., Prediction of solid oxide fuel cell cathode activity with first-principles descriptors. Energ Environ Sci **2011**, 4, 3966-3970.

147.   Nørskov, J. K.; Rossmeisl, J.; Logadottir, A.; Lindqvist, L.; Kitchin, J. R.; Bligaard, T.; Jónsson, H., Origin of the overpotential for oxygen reduction at a fuel-cell cathode. J Phys Chem B **2004**, 108, 17886-17892.

148.   Jung, W.; Tuller, H. L., A New Model Describing Solid Oxide Fuel Cell Cathode Kinetics: Model Thin Film $SrTi_{1-x}Fe_xO_{3-d}$ Mixed Conducting Oxides-a Case Study. Adv Energy Mater **2011**, 1, 1184-1191.

149.   Mizusaki, J., Nonstoichiometry, Diffusion, and Electrical-Properties of Perovskite-Type Oxide Electrode Materials. Solid State Ionics **1992**, 52, 79-91.

150.   Señarís-Rodríguez, M. A.; Goodenough, J. B., $LaCoO_3$ Revisited. Journal of Solid State Chemistry **1995**, 116, 224-231.

151.   Chen, X.; Yu, J.; Adler, S. B., Thermal and chemical expansion of Sr-doped lanthanum cobalt oxide ($La_{1-x}Sr_xCoO_{3-\delta}$). Chem Mater **2005**, 17, 4537-4546.

152.   Sakai, N.; Yamaji, K.; Horita, T.; Kishimoto, H.; Brito, M. E.; Yokokawa, H.; Uchimoto, Y., Application of SIMS analyses on oxygen transport in SOFC materials. Applied Surface Science **2006**, 252, 7045-7047.

153. Señarís-Rodríguez, M. A.; Goodenough, J. B., Magnetic and Transport Properties of the System $La_{1-x}Sr_xCoO_{3-\delta}$ ($0 \leq x \leq 0.50$). Journal of Solid State Chemistry **1995**, 118, 323-336.

154. Efimov, V.; Efimova, E.; Karpinsky, A.; Kochubey, D. I.; Kriventsov, V.; Kuzmin, A.; Molodtsov, S.; Sikolenko, V.; Tiutiunnikov, S.; Troyanchuk, I. O.; Shmakov, A. N.; Vyalikh, A., XAFS and neutron diffraction study of the $La_{1-x}Sr_xCoO_3$. Phys Status Solidi C **2007**, 4, 805-808.

155. Baskar, D.; Adler, S. B., High temperature magnetic properties of Sr-Doped lanthanum cobalt oxide ($La_{1-x}Sr_xCoO_{3-\delta}$). Chem Mater **2008**, 20, 2624-2628.

156. Horita, T.; Yamaji, K.; Sakai, N.; Yokokawa, H.; Weber, A.; Ivers-Tiffée, E., Electrode Reaction of $La_{1-x}Sr_xCoO_{3-\delta}$ Cathodes on $La_{0.8}Sr_{0.2}Ga_{0.8}Mg_{0.2}O_{3-y}$ Electrolyte in Solid Oxide Fuel Cells. Journal of The Electrochemical Society **2001**, 148, A456-A462.

157. Borovskikh, L.; Mazo, G.; Kemnitz, E., Reactivity of oxygen of complex cobaltates $La_{1-x}Sr_xCoO_{3-\delta}$ and $LaSrCoO_4$. Solid State Sciences **2003**, 5, 409-417.

158. Adler, S. B., Mechanism and kinetics of oxygen reduction on porous $La_{1-x}Sr_xCoO_{3-\delta}$ electrodes. Solid State Ionics **1998**, 111, 125-134.

159. Benninghoven, A., Surface analysis by Secondary Ion Mass Spectrometry (SIMS). Surf Sci **1994**, 299–300, 246-260.

160. Pacholski, M. L.; Winograd, N., Imaging with mass spectrometry. Chem Rev **1999**, 99, 2977.

161. McDonnell, L. A.; Heeren, R. M. A., Imaging mass spectrometry. Mass Spectrometry Reviews **2007**, 26, 606-643.

162. Senoner, M.; Unger, W. E. S., SIMS imaging of the nanoworld: applications in science and technology. J Anal Atom Spectrom **2012**, 27, 1050-1068.

163. Benninghoven, A., Chemical-Analysis of Inorganic and Organic-Surfaces and Thin-Films by Static Time-of-Flight Secondary-Ion Mass-Spectrometry (Tof-SIMS). Angewandte Chemie-International Edition in English **1994**, 33, 1023-1043.

164. Deline, V. R.; Katz, W.; Evans Jr, C. A.; Williams, P., Mechanism of the SIMS matrix effect. Applied Physics Letters **1978**, 33, 832-835.

165. Valaskovic, G. A.; Morrison, G. H., Quantitative imaging ion microscopy: A short review. Scanning Microscopy **1992**, 6, 305-318.

166. Deloule, E.; Albarede, F.; Sheppard, S. M. F., Hydrogen Isotope Heterogeneities in the Mantle from Ion Probe Analysis of Amphiboles from Ultramafic Rocks. Earth Planet Sc Lett **1991**, 105, 543-553.

167.   Mckeegan, K. D., Oxygen Isotopes in Refractory Stratospheric Dust Particles - Proof of Extraterrestrial Origin. Science **1987**, 237, 1468-1471.

168.   Eiler, J. M.; Graham, C.; Valley, J. W., SIMS analysis of oxygen isotopes: Matrix effects in complex minerals and glasses. Chem Geol **1997**, 138, 221-244.

169.   Stephan, T.; Zehnpfenning, J.; Benninghoven, A., Correction of Dead-Time Effects in Time-of-Flight Mass-Spectrometry. J Vac Sci Technol A **1994**, 12, 405-410.

170.   Keenan, M. R.; Smentkowski, V. S.; Ohlhausen, J. A.; Kotula, P. G., Mitigating dead-time effects during multivariate analysis of ToF-SIMS spectral images. Surf Interface Anal **2008**, 40, 97-106.

171.   Langer-Hansel, K.; Schintlmeister, A.; Fleig, J.; Hutter, H., Oxygen transport in electroceramics investigated by electrochemical $^{18}O/^{16}O$ isotope exchange and ToF-SIMS. Surf Interface Anal **2013**, 45, 486-489.

172.   Fielitz, P.; Borchardt, G., On the accurate measurement of oxygen self-diffusivities and surface exchange coefficients in oxides via SIMS depth profiling. Solid State Ionics **2001**, 144, 71-80.

173.   Opitz, A. K.; Schintlmeister, A.; Hutter, H.; Fleig, J., Visualization of oxygen reduction sites at Pt electrodes on YSZ by means of O-18 tracer incorporation: the width of the electrochemically active zone. Phys Chem Chem Phys **2010**, 12, 12734-12745.

174.   Horita, T.; Yamaji, K.; Sakai, N.; Xiong, Y. P.; Kato, T.; Yokokawa, H.; Kawada, T., Determination of proton and oxygen movements in solid oxides by the tracer gases exchange technique and secondary ion mass spectrometry. Applied Surface Science **2003**, 203, 634-638.

175.   De Souza, R. A.; Kilner, J. A.; Walker, J. F., A SIMS study of oxygen tracer diffusion and surface exchange in $La_{0.8}Sr_{0.2}MnO_{3+delta}$. Mater Lett **2000**, 43, 43-52.

176.   Holzlechner G., K. M., Hutter H., Fleig J., A Novel ToF-SIMS Operation Mode for Improved Accuracy and Lateral Resolution of Oxygen Isotope Measurements on Oxides. Journal of Analytical Atomic Spectrometry **2013,** in press.

177.   Lee, J. L. S.; Gilmore, I. S.; Fletcher, I. W.; Seah, M. P., Topography and field effects in the quantitative analysis of conductive surfaces using ToF-SIMS. Applied Surface Science **2008**, 255, 1560-1563.

178.   Kita, N. T.; Ushikubo, T.; Fu, B.; Valley, J. W., High precision SIMS oxygen isotope analysis and the effect of sample topography. Chem Geol **2009**, 264, 43-57.

179. Abbe, E., Beiträge zur Theorie des Mikroskops und der mikroskopischen Wahrnehmung. Archiv f. mikrosk. Anatomie **1873**, 9, 413-418.

180. 22493:2008, I., Microbeam analysis -- Scanning Electron Microscopy -- Vocabulary.

181. Senoner, M.; Wirth, T.; Unger, W. E. S., Imaging surface analysis: Lateral resolution and its relation to contrast and noise. J Anal Atom Spectrom **2010**, 25, 1440-1452.

182. Benningh.A, Surface Investigation of Solids by Statical Method of Secondary Ion Mass Spectroscopy (Sims). Surf Sci **1973**, 35, 427-457.

183. Belu, A. M.; Graham, D. J.; Castner, D. G., Time-of-flight secondary ion mass spectrometry: techniques and applications for the characterization of biomaterial surfaces. Biomaterials **2003**, 24, 3635-3653.

184. Kollmer, F.; Paul, W.; Krehl, M.; Niehuis, E., Ultra high spatial resolution SIMS with cluster ions - approaching the physical limits. Surf Interface Anal **2012**.

185. Horita, T.; Yamaji, K.; Sakai, N.; Yokokawa, H.; Kawada, T.; Kato, T., Oxygen reduction sites and diffusion paths at $La_{0.9}Sr_{0.1}MnO_{3-x}$/yttria-stabilized zirconia interface for different cathodic overvoltages by secondary-ion mass spectrometry. Solid State Ionics **2000**, 127, 55-65.

186. Kawada, T.; Horita, T.; Sakai, N.; Yokokawa, H.; Dokiya, M.; Mizusaki, J., A novel technique for imaging electrochemical reaction sites on a solid oxide electrolyte. Solid State Ionics **2000**, 131, 199-210.

187. Kishimoto, H.; Sakai, N.; Yamaji, K.; Horita, T.; Brito, M. E.; Yokokawa, H.; Amezawa, K.; Uchimoto, Y., Visualization of oxygen transport behavior at metal electrode/oxide electrolyte interface using secondary ion mass spectrometry. Solid State Ionics **2008**, 179, 347-354.

188. Horita, T.; Yamaji, K.; Sakai, N.; Yokokawa, H.; Kato, T., Oxygen Transport at the $LaMnO_3$ Film/Yttria-Stabilized Zirconia Interface under Different Cathodic Overpotentials by Secondary Ion Mass Spectrometry. Journal of The Electrochemical Society **2001**, 148, J25-J30.

189. Horita, T.; Yamaji, K.; Sakai, N.; Xiong, Y.; Kato, T.; Yokokawa, H.; Kawada, T., Imaging of oxygen transport at SOFC cathode/electrolyte interfaces by a novel technique. J Power Sources **2002**, 106, 224-230.

190. Opitz, A. K.; Lutz, A.; Kubicek, M.; Kubel, F.; Hutter, H.; Fleig, J., Investigation of the oxygen exchange mechanism on Pt|yttria stabilized zirconia at

intermediate temperatures: Surface path versus bulk path. Electrochim Acta **2011**, 56, 9727-9740.

191.   Opitz, A. K.; Hörlein, M. P.; Huber, T.; Fleig, J., Current-Voltage Characteristics of Platinum Model Electrodes on Yttria-Stabilized Zirconia. Journal of The Electrochemical Society **2012**, 159, B502-B513.

192.   Fleig, J.; Opitz, A.; Schintlmeister, A.; Kubicek, M.; Hutter, H., Monitoring Active and Resistive Zones of SOFC Cathodes by Voltage Driven Tracer Incorporation. Ecs Transactions **2011**, 35, 2217-2226.

193.   Krumbein, S. J., Metallic Electromigration Phenomena. Ieee T Compon Hybr **1988**, 11, 5-15.

194.   De Souza, R. A.; Chater, R. J., Oxygen exchange and diffusion measurements: The importance of extracting the correct initial and boundary conditions. Solid State Ionics **2005**, 176, 1915-1920.

195.   De Souza, R. A.; Zehnpfenning, J.; Martin, M.; Maier, J., Determining oxygen isotope profiles in oxides with Time-of-Flight SIMS. Solid State Ionics **2005**, 176, 1465-1471.

196.   Fahey, A. J.; Messenger, S., Isotopic ratio measurements by time-of-flight secondary ion mass spectrometry. Int J Mass Spectrom **2001**, 208, 227-242.

197.   Lee, J. L. S.; Gilmore, I. S.; Seah, M. P., Linearity of the instrumental intensity scale in TOF-SIMS - A VAMAS interlaboratory study. Surf Interface Anal **2012**, 44, 1-14.

198.   Manning, P. S.; Sirman, J. D.; DeSouza, R. A.; Kilner, J. A., The kinetics of oxygen transport in 9.5 mol % single crystal yttria stabilised zirconia. Solid State Ionics **1997**, 100, 1-10.

199.   Opitz, A. K.; Fleig, J., Investigation of O_2 reduction on Pt/YSZ by means of thin film microelectrodes: The geometry dependence of the electrode impedance. Solid State Ionics **2010**, 181, 684-693.

200.   Kim, J. J.; Kuhn, M.; Bishop, S. R.; Tuller, H. L., Cathodic and defect properties of $Ba_xSr_{1-x}Co_{1-y}Fe_yO_{3-\delta}$ mixed conducting oxides. Solid State Ionics **2013**, 230, 2-6.

201.   Yeh, T. C.; Routbort, J. L.; Mason, T. O., Oxygen transport and surface exchange properties of $Sr_{0.5}Sm_{0.5}CoO_{3-\delta}$. Solid State Ionics **2013**, 232, 138-143.

202.   Fleig, J.; Maier, J., The polarization of mixed conducting SOFC cathodes: Effects of surface reaction coefficient, ionic conductivity and geometry. J Eur Ceram Soc **2004**, 24, 1343-1347.

203.   Opitz, A. K.; Kubicek, M.; Huber, S.; Huber, T.; G., H.; Hutter, H.; Fleig, J., Thin film cathodes in SOFC research: how to identify oxygen reduction pathways? submitted to Journal of Materials Research **2013**.

9 List of Abbreviations and Symbols

AC   alternating current

AES   Auger electron spectroscopy

AFM   atomic force microscopy

BA   burst alignment (a ToF-SIMS mode)

BSCF   Barium Strontium Cobalt Ferrite

CBA   collimated burst alignment (a ToF-SIMS mode)

CN   coordination number

DC   direct current

DHM   digital holographic microscopy

EDX   energy dispersive X-ray spectroscopy

EIS   electrochemical impedance spectroscopy

HCBU   high current bunched (a ToF-SIMS mode)

ICDD   International Center for Diffraction Data

ICP-OES: inductively coupled plasma-optical emission spectroscopy

IEDP   isotope exchange depth profiling

ISO   International Organization for Standardization

LAO   Lanthanum Aluminate

LSC   Lanthanum Strontium Cobaltite

LSC64   LSC composition $La_{0.6}Sr_{0.4}CoO_{3-\delta}$

LSC82   LSC composition $La_{0.8}Sr_{0.2}CoO_{3-\delta}$

LSC-HT   LSC deposited at high temperature

LSC-LT   LSC deposited at low temperature

$L^{86}SC$ LSC composition containing Sr isotope tracer

LSC-T10   LSC composition containing Sr isotope tracer, Fe and Sm

LSCF   Lanthanum Strontium Cobalt Ferrite

LSM   Lanthanum Strontium Manganite

MIEC   mixed ionic electronic conduction

NIST   National Institute of Standards and Technology (USA)

ORR	oxygen reduction reaction
PDF	powder diffraction file
PLD:	pulsed laser deposition
Q	constant phase element
R	resistance
RMS	root mean square roughness
RSM	reciprocal space mapping
SEM	scanning electron microscopy
SIMS	secondary ion mass spetrometry
SOFC:	solid oxide fuel cell
STO	Strontium Titanate
TEM	transmission electron microscopy
ToF-SIMS	time-of-flight secondary ion mass spectrometry
VSMOW	Vienna Standard Mean Ocean Water
XPS	X-ray photoelectron spectroscopy
XRD	X-ray diffraction
XRR	X-ray reflection
YSZ	Yttria stabilized Zirconia

c	concentration, tracer fraction
c'	normalized ^{18}O tracer fraction
$c_{Fe, Sm, Sr}$	normalized tracer levels
$corr_{Co, La}$	element specific correction factors for different secondary ion yields
$Cu\ K\alpha_1$	emission line of copper, 0.15418 nm wavelength
δ	oxygen non-stoichiometry
d	film thickness
D	diffusion coefficient
D*	tracer diffusion coefficient
D_{chem}	chemical diffusion coefficient
D_g	grain (bulk) diffusion coefficient
D_{gb}	grain boundary diffusion coefficient
D_V	vacancy diffusion coefficient
e_0	elementary charge
E_a	activation energy
erf	error function
f_c	correlation factor related to crystal structure
ΔG	Gibbs Free Energy
ΔG_0	standard Gibbs Free Energy
$h^{\cdot}$	electron hole
H	Haven ratio
ΔH_0	standard reaction enthalpy
k_B	Boltzmann's constant
k	surface exchange coefficient
k*	tracer surface exchange coefficient
k_{chem}	chemical surface exchange coefficient
λ	wavelength
l	film thickness (tracer)
l_{diff}	diffusion length
L	quotient of film thickness and critical length
m	mass
M_{Sr}	amount of Strontium

$O_O^\times$	oxide ion on a standard lattice site
$p(O_2)$	oxygen partial pressure
R_i	electrode interface polarization resistance
R_s	electrode surface polarization resistance
θ	a crystallographic angle
t	time
T	temperature
u_v	mobility of vacancies
$V_O^{\bullet\bullet}$	Oxygen vacancy
$V_{Sr}^{\parallel}$	Strontium vacancy
ω	a crystallographic angle
z	charge number

10 List of Figures

11 List of Tables

12 Acknowledgements